Stony Brook University

Investigations in the crystal growth and neutron scattering of superconductors and a relaxor ferroelectric

A Dissertation presented

by

John A. Schneeloch

to

The Graduate School

in Partial Fulfillment of the

Requirements

for the Degree of

Doctor of Philosophy

in

Physics

Stony Brook University

August 2016

Stony Brook University

The Graduate School

John A. Schneeloch

We, the dissertation committee for the above candidate for the
Doctor of Philosophy degree, hereby recommend
acceptance of this dissertation

Genda Gu—Dissertation Advisor
Adjunct Professor, Physics and Astronomy Department

John M. Tranquada—Dissertation Advisor
Senior Physicist, Condensed Matter Physics and Materials Science Department,
Brookhaven National Laboratory

Philip B. Allen—Chairperson of Defense
Professor, Physics and Astronomy Department

Dominik A. Schneble
Associate Professor, Physics and Astronomy Department

Matthew Dawber
Associate Professor, Physics and Astronomy Department

Weiguo Yin
Physicist, Condensed Matter Physics and Materials Science Department,
Brookhaven National Laboratory

This dissertation is accepted by the Graduate School

Nancy Goroff
Interim Dean of the Graduate School

Abstract of the Dissertation

Investigations in the crystal growth and neutron scattering of superconductors and a relaxor ferroelectric

by

John A. Schneeloch

Doctor of Philosophy

in

Physics

Stony Brook University

2016

In this dissertation, I present research on four materials with properties that are not well understood, and illustrate the many roles inhomogeneity and disorder may play in material properties. First, we investigated materials synthesis and annealing conditions of the proposed topological superconductor $Cu_xBi_2Se_3$, finding that quenching above a minimum temperature was essential for superconductivity. Due to the inhomogeneity of $Cu_xBi_2Se_3$, we suggest that a metastable secondary phase may be responsible for the superconductivity. Second, we performed neutron scattering measurements on samples in the $Fe_{1+y}Te_{1-x}Se_x$ family of iron-based superconductors, focusing on the anomalous phonon mode recently discovered near Bragg peaks forbidden by symmetry and at high-symmetry wavevectors where the mode's neutron scattering intensity is expected to be zero. We characterize this mode and propose that disorder may explain its anomalous visibility. Third, a superconducting crystal of the bilayer cuprate $La_{1.9}Ca_{1.1}Cu_2O_{6+\delta}$ was synthesized and measured by neutron scattering. Though the magnetic excitations near $(0.5, 0.5)$ in reciprocal space resemble those of weakly doped members of the $La_{2-x}Ae_xCuO_4$ (Ae=Ca, Sr, Ba) cuprate superconductor family, the temperature-dependence of the intensity of the magnetic excita-

tions is much different from those of weakly hole-doped cuprates. Superstructural peaks appear to indicate ordering induced by interstitial oxygen, and a comparison with the similarly oxygen-doped cuprate $La_2CuO_{4+\delta}$ suggests the possibility of phase separation. Fourth, the relaxor ferroelectric $Pb(Mg_{1/3}Nb_{2/3})_{0.68}Ti_{0.32}O_3$ was measured with neutron scattering while subjected to an electric field. From differences in neutron scattering intensity with and without field, we find a possible coupling between short-range polar correlations and transversely-polarized phonons near certain Brillouin zone centers.

Dedication Page

To my family.

Contents

List of Figures

List of Tables

Acknowledgements

I could not have made it this far without the help of a great number of people. Of course, my advisors Genda Gu and John Tranquada deserve a great deal of credit for what I've been able to achieve. Genda has taught me first-hand about the growth of crystals, which involves much more skill than it might appear from the outside. He has been very patient, offered lots of practical advice, and led me to pursue opportunities that I otherwise would not have considered. John Tranquada, the leader of our group, has offered plenty of helpful comments and suggestions, and has always pushed for high standards in my research.

I thank Guangyong Xu for mentoring me on neutron scattering. Much of the results in this thesis are from experiments he proposed. He has offered plenty of advice on giving presentations, the best way to phrase things in papers, how to analyze data, what to look for in a large data set, and so forth.

I thank Ruidan Zhong, my officemate, for being a good role model.

I thank Zhijun Xu and Jinsheng Wen, my colleagues and also former members of our group at BNL, for their help, their advice, and for being pleasant to work with. I thank David Fobes for collaborating with us and for his "neutronpy" code which has made much of the data analysis in this research easier.

I thank my many collaborators for their advice and support, especially Peter Gehring, from NIST, and Igor Zaliznyak and Markus Hücker, who I've worked with in the neutron scattering group.

Whenever we do neutron scattering experiments at NIST or ORNL, we have essential help from instrument scientists such as Barry Winn, Melissa Graves-Brook, Matt Stone, Masaaki Matsuda, and Daniel Pajerowski at ORNL, and Jose Rodriguez-Rivera, Daniel Parshall, and Yang Zhao at NIST.

I thank Kim Mohanty and Ed Stein for providing technical assistance to our group and for keeping things running smoothly.

As for my fellow graduate students, I have had the pleasure to study with them, play board games with them, attend parties with them, go on trips with them, live with them, and generally share an experience these past seven years that could have been tedious but was instead fun.

Finally, I simply wouldn't be where I am today if it weren't for my family, including my parents who raised and supported me, and my three brothers who, each in their own ways, show the value of a life well-lived.

The work in Sections 3, 4, and 5 was supported as part of the Center for Emergent Superconductivity, an Energy Frontier Research Center funded by the U.S. Department of Energy, Office of Science, Office of Basic Energy Science. The work in Section 3 benefitted from facilities at the Center for Functional Nanomaterials, which is funded by the same Office. Most of the work in this dissertation was performed at Brookhaven National Laboratory, which is funded through Contract No. DE-SC00112704. The research at Oak Ridge National Laboratory's Spallation Neutron Source was sponsored by the Scientific User Facilities Division, Office of Basic Energy Sciences, U.S. Department of Energy. The research at the National Institute of Standards and Technology's NIST Center For Neutron Research utilized facilities supported in part by the National Science Foundation under Agreement No. DMR-1508249.

1 Introduction

As a student in the Neutron Scattering Group at Brookhaven National Laboratory, I have worked with a variety of materials with interesting properties that are not well understood. These materials are related to such loosely-related topics as topological superconductors, iron-based superconductors, cuprate superconductors, and relaxor ferroelectrics, but a common characteristic of many of these materials is a possible role of inhomogeneity or disorder in their properties. Often, materials are thought of as perfectly crystalline and homogeneous, but it can be instructive to take a bird's eye view of the many ways disorder and inhomogeneity can affect properties. With this in mind, for each of the four materials covered in this dissertation, the proposed topological superconductor $Cu_xBi_2Se_3$, the iron-based superconductor family $Fe_{1+y}Te_{1-x}Se_x$, the cuprate superconductor $La_{1.9}Ca_{1.1}Cu_2O_{6+\delta}$, and the relaxor ferroelectric $Pb(Mg_{1/3}Nb_{2/3})_{0.68}Ti_{0.32}O_3$, I will detail an issue that has evaded understanding, our attempts to clarify this issue, and what role inhomogeneity and disorder may play.

Our group conducts both crystal growth and neutron scattering experiments. For crystal growth, usually the goal is simply to grow large single crystals so that we may study them by neutron scattering or other means, but the process of optimizing crystal growth conditions can itself yield insights. For example, $Cu_xBi_2Se_3$ has been proposed to be a topological superconductor [1–3]. Although topological properties have been studied for decades in the form of the integer quantum Hall effect, there has been an explosion within the past decade of interest in materials with topologically nontrivial electronic structures due to the proposal and confirmed existence of topological insulators [4]. (See Section 2.3 for an overview of topological materials.) Superconductors with topologically nontrivial electronic structures were also proposed, the first being $Cu_xBi_2Se_3$ ($0.1 \leq x \leq 0.6$), though as yet no topological superconductors have been confirmed to exist[1]. A primary issue with $Cu_xBi_2Se_3$ is that, when one combines the elemental ingredients, attempts crystal growth (resulting in a silvery, flaky ingot of material), cuts pieces from the ingot, and measures their diamagnetic responses (a signal for superconductivity), the degree of superconductivity as measured by magnetic susceptibility for each piece is usually very low and may vary substantially

[1] A recent list of candidate topologically-nontrivial superconductors can be seen in Ref. [5]

from piece to piece. This unpredictability impedes understanding of the properties of this material. Section 3 presents our attempt to clarify this situation. We found that: 1. Quenching from a sufficiently high temperature is essential for superconductivity. 2. The melt growth method (simply melting the ingredients together) sometimes results in pieces with large shielding fractions but the in-ampoule floating zone method (a crystal growth method typically resulting in high quality single crystals) rarely does. In floating zone growth, the very top of the grown rod tends to become very Cu-concentrated. We interpret our findings as suggesting that a metastable impurity phase may be responsible for the superconductivity.

$Fe_{1+y}Te_{1-x}Se_x$ is a family of iron-based superconductors. The iron-based superconductors were discovered in 2008, starting with $LaFeAsO_{1-x}F_x$ [6] with $T_C = 26$ K (the related $Gd_{1-x}Th_xFeAsO$[7] and $SmFeAsO_{1-x}F_x$ [8] compounds hold record T_C values of 55 and 56 K, respectively, for bulk iron-based superconductors). While the $Fe_{1+y}Te_{1-x}Se_x$ family has a relatively modest maximum T_C of 15 K [9], this family is especially convenient to work with due to the lack of arsenic present in most other iron-based superconductors and due to the fact that large single crystals can be grown relatively easily. Though there are many questions about the mechanism of superconductivity and its relation to magnetic interactions in the iron-based superconductors (most of our group's neutron scattering experiments have investigated the magnetic excitations and their potential relationship to the superconductivity in this compound), in Section 4 we instead study unusual, recently discovered [10] anomalous phonon mode behavior. We identify the mode as the c-axis polarized transverse acoustic mode branch, despite this mode ideally having zero intensity in the $HK0$ plane. We propose that the mode's anomalous visibility in the $HK0$ plane, and its clear presence near forbidden Bragg peak wavevectors even where other acoustic phonon modes are too weak to be detected, may be explained by disorder misaligning the polarization vectors of phonon modes.

The source of superconductivity in the high-transition temperature cuprate superconductors remains poorly understood, but magnetic interactions are commonly thought to play a role, and over the years neutron scattering experiments on a number of families of hole-doped cuprates have shown a similar trend in the types of magnetic excitations seen as a function of doping [11]. The bilayer $La_{2-x}Ca_{1+x}Cu_2O_{6+\delta}$ family has been relatively infrequently studied due to the difficulty of annealing at pressures on the order of $\sim$670 MPa, which is needed to introduce enough oxygen to the sample to induce

bulk superconducitivty. However, our group has recently grown and annealed large single crystals of $La_{1.9}Ca_{1.1}Cu_2O_{6+\delta}$, and we have measured one of them by neutron scattering to characterize its magnetic excitations. This research is presented in Section 5. Surprisingly, though annealed samples appear to have bulk superconductivity, the magnetic excitations in the sample are unlike those seen in other superconducting hole-doped cuprates, being commensurate rather than incommensurate. The dispersion of the magnetic excitations resembles that in weakly hole-doped, non-superconducting cuprates, except that the intensity of the magnetic excitations within a certain energy range drops with increasing temperature, a behavior much different than that seen in the underdoped cuprates In the similarly oxygen-doped $La_2CuO_{4+\delta}$ cuprates, the doped interstitial oxygen atoms are mobile at 300 K and phase segregate into various ordered phases at low temperatures [12]. A similar phase separation might occur in oxygen-annealed $La_{1.9}Ca_{1.1}Cu_2O_{6+\delta}$, but we do not yet have an explanation for how multiply phases could explain our results. A naive model where the commensurate excitations come from non-superconducting regions and the diamagnetic response comes from superconducting regions would not explain the apparent lack of incommensurate excitations or the unusual temperature-dependence of the commensurate excitations.

Relaxor ferroelectrics are a family of ferroelectrics with a number of unusual properties, such as a dielectric function $\epsilon(\omega)$ that is broad in temperature and whose frequency dependence shows continuing variation down to very low frequencies (e.g., $\sim$1 kHz) [13]. This behavior is in contrast to that of "normal" ferroelectrics, for which $\epsilon(\omega)$ tends to have sharp peaks at structural phase transitions. Relaxors are associated with strong charge disorder due to the random occupation of ions of varying valence on the same site. Much of the research in relaxors is spurred by a desire to understand the extremely high d_{33} piezoelectric coefficients along certain directions measured in some relaxor single crystals, such as in $(1-x)$PMN-xPT [14], where PMN is $PbMg_{1/3}Nb_{2/3}O_3$, PT is $PbTiO_3$, and x denotes the fraction of PMN substituted with PT in a solid solution. The phase diagrams of relaxors such as $(1-x)$PMN-xPT show a high-temperature paraelectric phase, a region with relaxor behavior for small x at low temperature, and a conventional ferroelectric phase for larger x at low temperature [15], with the d_{33} coefficient reaching a maximum for x between the regions for conventional and relaxor ferroelectric behavior [14, 16]. Short-range polar order has been measured in the form of diffuse scattering by X-ray and neutron scattering measurements

[17], and may be indicative of polar nanoregions which were first invoked to explain optical index of refraction data [18]. A past experiment by members of our group showed a coupling between the short-range polar order and acoustic phonons along certain direction in a single crystal of the relaxor $0.955PbZn_{1/3}Nb_{2/3}O_3$-$0.045PbTiO_3$, which was shown in experiments where samples were cooled in the presence of an electric field [19]. In that experiment, the effect of the field may have been due to a shifting of ferroelectric domains polarized along different $\langle 111 \rangle$ orientations. We have conducted an experiment with the field applied along [001] in the related relaxor 0.68PMN-0.32PT, so that no single domain should be favored and so that a more direct effect of the electric field on the short-range order or phonons could be seen without the effect of a shifting population of domains. These results are presented in Section 6. We observed coupling between short-range polar order and acoustic and optic phonons along different sets of polarizations and with different characteristics than the coupling observed in Ref. [19].

In these four disparate materials, we see four possible examples of disorder or inhomogeneity:

- In $Cu_xBi_2Se_3$, a metastable secondary phase may be responsible for the superconductivity.
- In $Fe_{1+y}Te_{1-x}Se_x$, disorder may explain why a certain phonon mode has non-zero neutron scattering intensity at wavevectors where zero intensity would be expected. Chemical disorder is present in the form of interstitial Fe and the substitutional disorder of Se and Te.
- In $La_{1.9}Ca_{1.1}Cu_2O_{6+\delta}$, the interstitial oxygen atoms might phase segregate at low temperatures, as seen in the similar oxygen-doped cuprate $La_2CuO_{4+\delta}$.
- In 0.68PMN-0.32PT, a coupling between short-range order (possibly associated with polar nanoregions) and various phonons may explain changes in the phonon properties between electric field-cooled and zero-field-cooled conditions.

Hopefully, the great range of possible roles of disorder and inhomogeneity will highlight the importance of having an open mind in the analysis of data.

2 Background Information

2.1 Materials Synthesis and Crystal Growth

2.1.1 General information

Large single crystals can be valuable for many applications, for example, in single-crystal turbine blades, in the very large boules of silicon used for integrated circuits, and in research [20]. While many experimental probes of materials require single crystals to get the most useful information, neutron scattering (used for most of the research in this thesis) in particular requires large single crystals due to the weak interaction of neutrons with matter, with neutron scattering penetration depths often on the order of centimeters. Furthermore, materials synthesis experiments play an important role in condensed matter physics beyond simply providing known materials for other experiments. For example, in the La-based cuprate superconductors discovered in 1986, early experiments found evidence of superconductivity and antiferromagnetism in nominally pure La_2CuO_4, but later measurements with single crystals of better quality clarified that superconductivity is only present in samples with excess oxygen [21]. Another example is the proposed topological superconductor $Cu_xBi_2Se_3$, whose superconductivity is likely to be highly inhomogeneous. In Section 3, I present research on $Cu_xBi_2Se_3$ that attempts to relate the results of materials synthesis experiments with the possibility of a secondary phase being responsible for the superconductivity. In this Section, I will provide background information about crystal growth, especially information relevant to the synthesis of the materials that are the subject of this thesis. Special attention will be given to the optical floating zone growth method, used to grow the $La_{1.9}Ca_{1.1}Cu_2O_{6+\delta}$ crystal used for the neutron scattering experiments discussed in Section 5.

There are a number of techniques available for growing bulk single crystals. These can be divided according to the phase of the initial ingredients [22]: solid-to-solid, liquid-to-solid, and gas-to-solid. In this section I will focus mainly on liquid-to-solid growth methods due to that method being used most often for the growth of our materials, but solid-to-solid and gas-to-solid methods have been important as well. For example, large single crystals of metals such as iron have been made by the strain-anneal method [23], a solid-to-solid growth method. Also, a popular example of a gas-to-solid growth method for bulk crystal growth is the vapor transport method, which has

been used to grow compounds such as FeSe [24].

One of the simplest of the liquid-to-solid growth methods is the **melt-growth** method, where initial solid ingredients are heated together until they react and form a liquid, which is then slowly cooled until solid. Since a monotonic temperature gradient is not applied, crystal nucleation may occur at many locations at once, resulting in crystal domains being limited in size, though possibly still large enough for study.

Another method, the **Bridgman method**, is when solidification takes place in a temperature gradient that cools uniformly with time.[2] Often, a furnace is used that has many zones that can be set to different temperatures to create a custom temperature profile, but the natural temperature gradient of an ordinary box furnace is often sufficient. Initially, many small crystals nucleate at the cooler end of the ingot. As the temperature uniformly decreases, these crystals grow toward the warmer end, with larger crystals dominating until (ideally) single-crystal growth is achieved.

These methods share many common considerations. First, ampoules, often made of "fused quartz" silica glass such as the ampoules shown in Fig. 1, are frequently used to seal the sample in an atmosphere with a desired composition. This atmosphere is often an inert gas, such as argon, or a vacuum, though gases that are oxidizing (such as O_2) or reducing (such as CO or argon-H_2 mixtures) may also be used. **Annealing** (heating below the melting point) procedures often use similar methods. For example, annealing in O_2 results in an increase of the hole doping concentration of $Bi_2Sr_2CaCu_2O_{8+\delta}$ due to the increased interstitial oxygen [27, 28], and annealing in vacuum, possibly with elemental Ti pieces included to absorb residual O_2, can decrease the hole concentration of $Bi_2Sr_2CaCu_2O_{8+\delta}$.

Second, it is usually essential to make sure the ingredients are well-mixed before crystal growth starts. Since mass diffusion in a liquid is not sufficient to equalize the composition across many centimeters in typical laboratory time scales, the container should be rocked enough for turbulent mixing of the liquid to occur.

Third, the ampoule can be oriented horizontally or vertically. One factor that may influence this decision is the possibility of expansion during cooling if a structural phase transition is present, which may lead to the ampoule cracking if it is oriented vertically due to the lack of space into which the

[2]Technically, the Bridgman method has the ingredients slowly moved through a temperature gradient rather than staying in place [25, 26].

Figure 1: Photo of pieces of Pb, Sn, In, and Te sealed in double layers of fused quartz glass ampoules for the synthesis of $Pb_{1-x-y}Sn_xIn_yTe$ and related materials, to explore potential topological insulator and superconductor properties.

material would expand.

Another class of methods are those involving **zone-melting**, where only a small region of the ingot is melted at a time [29]. This region, called the "liquid zone", moves slowly along the starting materials, ideally leaving behind a single crystal. Various heating methods have been used, including radio-frequency induction heating and optical heating with either focused light or lasers. The optical heating methods have the advantage of working with insulating materials. Zone-melting methods can also be divided based on whether the liquid zone is held in place by surface tension, as in the **floating zone growth** method, or whether an ampoule is used to contain the materials (often called the "traveling heater method" [30] or a "modified floating zone" method). Two big advantages of floating zone methods is that the liquid zone is not in contact with a crucible, which reduces the possibility of nucleation from unwanted regions, and that there is no need to find a chemically-compatible crucible to contain the materials. The optical floating zone method (hereafter simply called the "floating zone (FZ) method") has been one of the most useful for growing large single crystals, and yet one of the most complicated to employ. Due to its importance in growing many of our materials, such as the $La_{1.9}Ca_{1.1}Cu_2O_6$ crystal measured with neutron scattering in Section 5, we discuss it in detail below in a separate section.

Another way to classify growth methods is by whether or not a solvent (or "flux") is used. For methods such as melt growth or Bridgman growth, if a flux is used, the method can be called **flux growth**. If a flux contains only the elements of the grown compound, then the method is called a **self-flux method**; for example, $ZrTe_5$ crystals can be grown from a flux of excess Te with a Zr:Te ratio of 0.0025:0.9975 [31]. Alternatively, a flux not containing elements of the crystal can be used. Fluxes such as the alkali halides and molten tin are popular choices for many materials of interest to condensed matter physics. Water is, of course, also a solvent that can be used in crystal growth, which has been used since antiquity at ambient conditions for the production of salt and sugar crystals [22]. For **hydrothermal synthesis**, water is used as a solvent at high pressure and temperature, taking advantage of the increased solubility range in water under these conditions.

Aside from the crystal growth methods mentioned above, there are many more methods which are important in research and industry. The **Verneuil method**, or flame fusion method, involves dropping small bits of material through a flame, which then melts the material; these droplets then deposit onto a seed crystal, which is slowly lowered, and crystal growth occurs

[22]. The **Czochralski method** is the main method for producing single-crystalline silicon for electronics. This method involves lowering a seed crystal into the molten material and slowly raising the crystal as it solidifies [32]. **Top-seeded solution growth** is similar to the Czochralski method, but involves pulling a crystal out of a solution rather than out of a liquid having the crystal's composition [33].

2.1.2 The optical floating zone method

The first step in this method is to prepare a feed rod of raw materials. **Sintering** is often used to make the feed rod for oxide materials. Sintering may involve both the solid-state reaction of the initial ingredients and the transfer of mass among particles to form a less porous whole from the initial packed powder. For sintering, first, powders of initial ingredients (La_2O_3, $CaCO_3$, and CuO in the case of $La_{1.9}Ca_{1.1}Cu_2O_{6+\delta}$) are mixed together, put into a crucible, and heated to the point where they react together. This process is repeated a few more times to ensure that the initial ingredients are homogeneous. Frequently, carbonates such as $CaCO_3$ are used rather than the simpler oxides such as CaO. In this case, the carbon in the carbonate is liberated as CO_2 gas, and the sintering reaction is otherwise similar to the same reaction with the oxide. This method has the advantage that the less water-reactive carbonate is used instead of the oxide, which is probably why this method is more popular. However, for some compounds such as $HgBa_2CuO_{4+\delta}$, carbonate ingredients may be avoided to eliminate the possibility of carbon contamination [34]. After the powder has been mixed and ground several times, it is pressed at room temperature at typically 800-4000 bars [29] into a rod, with 4000 bars used for our $La_{1.9}Ca_{1.1}Cu_2O_{6+\delta}$ synthesis. The pressed powder rod is then sintered at as high a temperature as possible to reduce porosity (since sintering brings the initial particles closer), while avoiding the formation of liquid. Often, a "pre-melting" step is used, where the feed rod is quickly run through the zone-melting process to make the feed rod more compact.

Once the feed rod is sintered, it is put in the floating zone image furnace. Fig. 2 shows a screenshot of streaming video of the FZ growth of $La_{1.9}Ca_{1.1}Cu_2O_{6+\delta}$, from which a single crystal was obtained and used for the neutron scattering experiments in Section 5. The "feed rod", containing the initial materials, is on top. In the middle, light focused by a pair of elliptical mirrors to the left and right (not shown) heats the rod in the middle

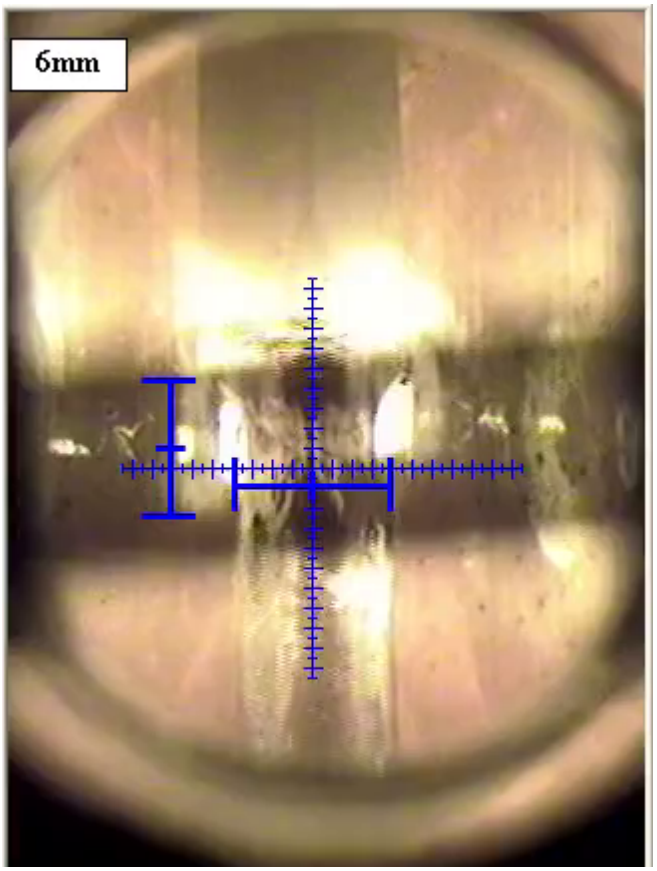

Figure 2: Screenshot from streaming video of the floating zone growth of the $La_{1.9}Ca_{1.1}Cu_2O_{6+\delta}$ compound used for the neutron scattering experiments in Section 5.

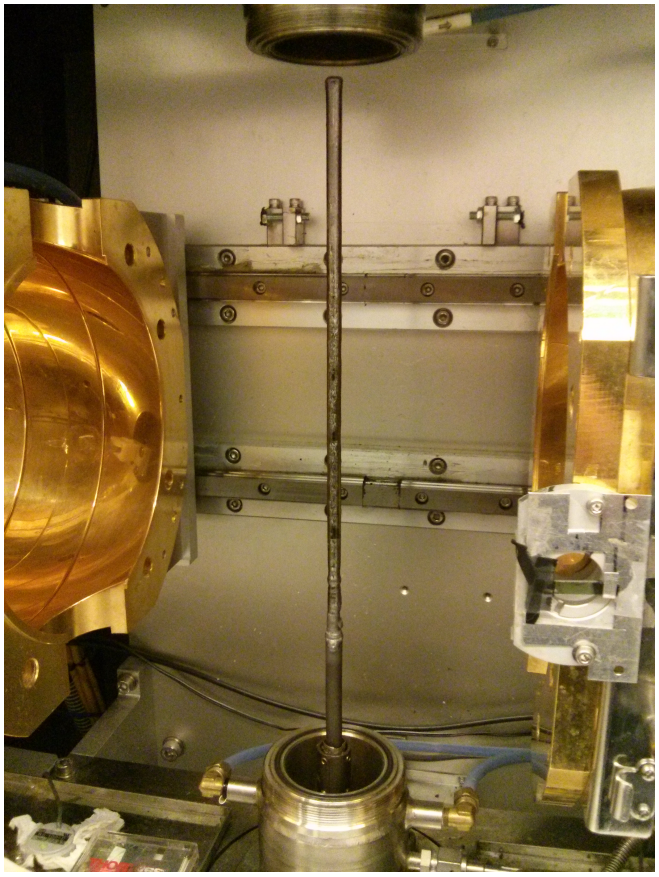

Figure 3: Photo of a floating-zone grown rod for $La_{1.9}Ca_{1.1}Cu_2O_{6+\delta}$. A single crystal from this rod was later used for the neutron scattering experiments shown in Section 5.

past its melting point. The "seed rod", on the bottom, may be a seed crystal, or it may simply be a pedestal of similar material that supports the liquid zone. The seed rod will accumulate the crystallized material as growth progresses. Most often, both rods are translated downward. The relative speeds can be varied, but are often similar to each other. A very slow speed for the seed rod (often < 1 mm/hr) is often needed to grow large single crystals to avoid the possibility of constitutional supercooling, as explained below. Ideally, the grown rod may look like the one shown in Fig. 3, but frequently, FZ growth fails due to spills of the liquid zone or other sudden changes in conditions which interrupt single-crystal growth.

There are a number of forces within the liquid zone that should be considered to understand floating zone growth. The origins of these forces are primarily surface tension, gravity from the weight of the liquid, and the normal force of the seed rod's support. Though the top and bottom rods are often counter-rotated, the centripetal acceleration of a point on the surface is much less than the acceleration due to gravity, and thus the centrifugal force can be neglected as far as stability of the liquid zone is concerned. However, the counter-rotation and forces arising from variations in surface tension and density are also important since they result in rapid mixing inside the liquid zone (up to a few cm/s; typical rod diameters are <1 cm) [29].

The shape of the liquid zone can be described by the Laplace capillary equation [35], where the curvature at a point on the surface is related to the pressure difference, which in turn is related to factors such as the distribution of weight within the liquid zone. If the liquid zone becomes too thin or too tall, the liquid will pinch together and break apart (i.e., it undergoes the Plateau-Rayleigh instability). If the liquid zone is too wide, the lack of curvature on the surface reduces the surface tension and the liquid may also spill due to its weight.

A complicating factor is that more liquid may be present than apparent from the size of the liquid zone due to the possibly porous nature of the feed rod. For example, in $La_{2-x}Sr_xCuO_4$ [36] and $La_{2-x}Ca_{1+x}Cu_2O_{6+\delta}$, the liquid zone may seep up into the feed rod. If the liquid zone composition is not at a eutectic composition, it may dissolve portions of the bottom of the feed rod, possibly leading to a precarious situation where portions of the feed rod abruptly break off and cause a liquid zone spill due to the shift in the distribution of weight. This situation may explain why we sometimes see sudden liquid spills during $La_{2-x}Ca_{1+x}Cu_2O_{6+\delta}$ growth even when the liquid zone shape is similar to its steady-state shape, and why these liquid spills

happen more often during the initial stages of growth, when the liquid zone has not yet reached its steady-state composition.

The shape of the liquid zone generally tends to change over time, either tending toward a stable, steady-state shape, or becoming more unstable over time until the liquid zone collapses, with oscillations in the shape possible either way [35]. (The composition may also need to stabilize, as discussed below.) Though first-principles simulations are difficult, there are a number of basic concepts that one can keep in mind. First, the interface between the seed rod and the liquid zone should be flat or curved upward, so that nucleation of crystals is most likely to occur in just one position on the interface, the top. (Unfortunately, the solid-liquid interface is hidden in the liquid zone, and cannot be seen without interrupting the growth.) Whether the interface is flat or curved up or down depends on the temperature distribution inside the liquid zone, which in turn depends on how the material's surface is heated and how heat flows inside the liquid zone.

Second, there is a steady-state "growth angle", the angle between a line tangent to the liquid zone where the liquid meets the seed rod's solid interface on the outside, and a line tangent to the grown seed rod at this same point [35]. If the growth angle is not its steady-state value, the shape of the liquid zone is not yet stable. The growth angle varies depending on the material and factors such as growth speed.

Third, constitutional supercooling should be avoided, which may occur for systems where the liquid zone composition is different from that of the grown crystal [29]. Most of the liquid zone can be considered to have a uniform composition due to vigorous convection, but near the solid surface of the seed rod the liquid moves very little. Since mass transport is dominated by diffusion in this region, it is called the "diffusion layer". As the seed rod crystallizes, the diffusion layer becomes depleted of species that join the crystal and enriched in species that are rejected from the crystal. This depletion/enrichment leads to a concentration gradient. For a peritectic-type transition (see below), this region will have a lower solidus temperature than the rest of the liquid zone. If the thermal gradient in this region is low enough, a part of the layer can become supercooled more than liquid closer to the solid-liquid interface; this situation is called "constitutional supercooling". The crystallization front thus becomes unstable, and numerous disruptions of single-crystal growth can occur. Constitutional supercooling can be avoided by choosing a lower growth speed, which reduces concentration gradients, or by increasing the temperature gradient (though this is harder to implement

and may lead to cracking due to increased thermal stress.) It should be noted that abrupt changes in parameters such as heating power or the speed or positions of the rods should be avoided after having started single-crystal growth, as they may also lead to rapid changes in the location of the solid-liquid interface.

For many materials, the composition of the liquid zone may be different from that of the feed rod or the desired composition. These materials are "incongruently melting", meaning that a liquid of the same composition does not solidify to a solid of that same composition at a single temperature, but rather to a different solid composition, with the composition of the liquid changing as the temperature cools from the liquidus (start of solidification) to the solidus (end of solidification) temperatures [29]. A common possibility is that the desired composition will only start solidifying if the liquid has a composition beyond a peritectic composition (see Fig. 12.11 of Ref. [29] for a phase diagram). In this case, one composition would solidify for a portion of the growth while the liquid zone composition changes, and only once the liquid zone composition reaches the peritectic point would the desired composition start to solidify and the composition of the liquid zone stabilize. To shorten the wait for the change in composition to occur or to make growth possible, a flux closer to the steady-state liquid zone composition may be melted on the seed rod to initialize the liquid zone composition. For example, for the FZ growth of $La_{1.9}Ca_{1.1}Cu_2O_{6+\delta}$ shown in Fig. 2, a flux of nominal composition $\sim La_{1.9}Ca_{1.1}Cu_4O_8$ was used.

2.1.3 Materials synthesis methods used in the research in this thesis

Many of these methods were used to grow the materials discussed in this thesis. In Section 3, the melt-growth method and a modified floating zone method were used. In Section 6, the crystal we purchased was grown from a top-seeded solution growth method. In Section 4, the $Fe_{1+y}Te_{1-x}Se_x$ and related materials were grown by a modified Bridgman method in which the natural temperature gradient of the furnace was used for unidirectional solidification. Finally, in Section 5, the $La_{1.9}Ca_{1.1}Cu_2O_{6+\delta}$ crystal was synthesized by sintering, followed by the optical floating zone method, and then annealing in an oxygen-containing atmosphere at $\sim$670 MPa.

Figure 4: Photo of the $La_{1.9}Ca_{1.1}Cu_2O_{6+\delta}$ crystal used for the neutron scattering experiments in Section 5. This crystal was obtained from the rod shown in Fig. 3. It is mounted on a goniometer, parts of which are wrapped in cadmium to absorb neutrons and reduce the background due to unintended scattering from the goniometer.

2.2 Neutron Scattering

Much information can be obtained from materials by scattering experiments. For neutrons, their ability to penetrate deeply into materials, their convenient momentum-energy relationship, and their sensitivity to magnetic moments in materials make them favorable for probing structural and magnetic correlations in materials. For example, elastic neutron scattering can be used to determine changes in the crystal structure or the kind of magnetic ordering present, and inelastic neutron scattering can provide information on lattice vibrations and magnetic excitations. My experience has focused on the neutron scattering of single crystals with triple-axis spectrometer and time-of-flight methods, and these areas are what I will focus on below, though neutron scattering has been used in a wide range of other research, such as in soft matter, metallurgy, biology, and so forth [37].

Neutrons have unique advantages (and some disadvantages) compared to other scattering probes such as X-rays. First, neutrons are sensitive to magnetic correlations in addition to structural correlations. Neutrons interact with matter in two ways: by the nuclear force between neutrons and atomic nuclei, and the magnetic interaction between neutrons and sources of the magnetization density within a material. Often, the intensity of neutron magnetic scattering can be comparable to that of nuclear neutron scattering.

Another advantage (and weakness) of neutrons is that they penetrate deeply into matter, with a penetration depth on the order of centimeters. In contrast, X-rays, for example, can only penetrate $\sim$10 µm into materials at 10.7 keV [15]. One example where probing more deeply is advantageous is in investigating the "skin effect" in relaxor ferroelectrics such as solid solutions of $PbMg_{1/3}Nb_{2/3}O_3$ and $PbZn_{1/3}Nb_{2/3}O_3$ with $PbTiO_3$. In these materials, the apparent crystal structure symmetry measured by X-rays differs depending on their penetration depth, which in turn depends on their incident energy[15], whereas neutrons penetrate deeply enough that surface effects are negligible. On the other hand, because the neutron scattering cross sections are much lower, larger single crystals are needed to get good data, which places a major constraint on the types of experiments that can be performed.

A third potential advantage of neutrons is that their scattering cross-sections vary much differently from those for X-rays or electrons, which tend to increase monotonically with atomic number [37]. Neutrons may thus be a better probe for materials with light elements or when contrast between

elements with similar atomic numbers is desired.

Finally, neutrons have a momentum-energy relation which is convenient for probing lattice vibrations and magnetic excitations. Solids often have interesting behavior on lengths scales of 10^{-10}m or greater and energies in the meV range. Neutrons can have the momentum necessary to probe these length scales even if their incident energy is only on the order of 10 meV; the relative energy resolution needed to measure common features in materials is thus easily achievable. X-ray scattering, on the other hand, would require energies of at least $\sim$10 keV to be able to probe momentum transfers of several reciprocal lattice units, which means their relative energy resolution would need to be $\sim 10^{-7}$ to match the absolute energy resolution of common neutron scattering techniques.

2.2.1 Neutron scattering techniques

For our research, the two most common neutron scattering methods are triple-axis spectrometry and time-of-flight spectrometry, which differ according to how energy transfer is measured. In **triple-axis spectrometry**, the incident energy is selected from a polychromatic beam of neutrons by a monochromator crystal in the beam path. The crystal is oriented so that only neutrons with energies close to certain values are reflected due to Bragg scattering. The sample is located in the path of the diffracted beam. After the neutrons are scattered from the material, some of them meet a second crystal called the analyzer crystal, which also uses Bragg scattering to select certain outgoing neutron energies. Thus, the detector should detect only scattered neutrons that have a chosen energy transfer. Commonly, intensity for one location in the space of momentum transfer $\mathbf{Q}$ and energy transfer $\hbar\omega$ is obtained at a time. In these cases, it is common to scan across a feature (e.g., a phonon dispersion curve) using fixed-$\hbar\omega$ or fixed-$\mathbf{Q}$ paths in $(\mathbf{Q}, \hbar\omega)$ space, or by taking measurements at a grid of points to survey a region of $(\mathbf{Q}, \hbar\omega)$ space. There are, however, triple-axis spectrometers equipped with multianalyzers that can obtain data from a range of momentum or energy transfers simultaneously.

The other common neutron scattering method is **time-of-flight spectrometry**, where the incident beam of neutrons is shaped into monochromatic pulses of times on the order of milliseconds. The time between the pulse hitting the sample and each neutron hitting a detector determines the energy transfer. Time-of-flight spectrometry frequently uses an array of de-

tectors so that many momentum and energy transfers can be measured with each pulse, resulting in data sets that are often many gigabytes large.

In these techniques, there are two sources for neutrons: from a nuclear reactor, or from the spallation of neutrons from collisions between accelerated protons and a target. For reactors, the neutrons are the result of the nuclear fission occurring in the reactor core, and some of these neutrons escape and proceed down neutron guides toward various instruments. Typically, these sources are continuous, but these beams can also be shaped into pulses using "choppers" (devices which only allow neutrons of certain velocities to pass through), thus allowing time-of-flight techniques. For spallation, a proton beam is incident on a target material, resulting in the spallation of neutrons away from the target. The proton beam is typically pulsed, but choppers are nonetheless used to reduce background noise from unintended neutron detection, select certain incident energies, and filter higher-order neutrons from the incident beam. Time-of-flight spectroscopy is frequently used at spallation sources.

Usually, the polarization of neutrons in the incoming beam is random, but by using polarized neutrons (selecting the polarization of the neutrons before and after scattering), magnetic and non-magnetic neutron scattering contributions can be distinguished. Two common ways of polarizing neutrons are by passing the beam through a filter of spin-polarized ^{3}He (the absorption cross-section of ^{3}He is very large, but only if the nuclear spin is antiparallel to the neutron spin), or by magnetic Bragg reflection from certain magnetized crystals.

2.2.2 Mathematical details

In scattering experiments, we are typically interested in the double-differential cross section $d^2\sigma/d\Omega_f dE_f$, which represents the rate at which particles are scattering into a solid angle $d\Omega_f$ with a final energy between E_f and E_f+dE_f. Each neutron has incident energy E_i and momentum $\mathbf{k}_i$, and after scattering has final energy E_f and momentum $\mathbf{k}_f$. The energy transfer is defined as $\hbar\omega = E_i - E_f$, and the momentum transfer is $\mathbf{Q} = \mathbf{k}_f - \mathbf{k}_i$. Scattering can be split into elastic ($\hbar\omega = 0$) and inelastic ($\hbar\omega \neq 0$) scattering. Most often, data are obtained for $\hbar\omega > 0$, termed neutron energy loss, rather than $\hbar\omega < 0$, termed neutron energy gain. Provided that the spin and spatial states of the nuclei are not too correlated, neutron scattering can also be divided into coherent and incoherent scattering [38]. In addition, neutron

scattering can be split between magnetic and nuclear neutron scattering, depending on whether the neutron interacts with matter via the nuclear or magnetic interaction.

Several approximations and simplifications can be made in obtaining neutron scattering formulae. First, since neutron scattering constitutes a weak perturbation of the material being probed, the double differential cross section can be obtained from Fermi's Golden rule. Thus, we have [37]

$$\frac{d^2\sigma}{d\Omega_f dE_f} = \frac{k_f}{k_i}\left(\frac{m_n}{2\pi\hbar^2}\right)^2 |\langle \mathbf{k}_f\lambda_f|V|\mathbf{k}_i\lambda_i\rangle|^2\delta(\hbar\omega + E_i - E_f) \tag{1}$$

Here, the initial and final states' quantum numbers are denoted λ_i and λ_f, respectively; m_n is the neutron mass; and V is the interaction operator of the neutron with the sample.

Second, the weakness of the perturbation allows us to use the Born approximation, where incident and outgoing neutrons are treated as plane waves. This allows us to decompose the V matrix elements as

$$\langle \mathbf{k}_f\lambda_f|V|\mathbf{k}_i\lambda_i\rangle = \sum_l V_l(\mathbf{Q})\langle\lambda_f|e^{i\mathbf{Q}\cdot\mathbf{r}_l}|\lambda_i\rangle \tag{2}$$

l labels each scattering center, and the sum goes over every scattering center in the neutron's path.

Third, for nuclear neutron scattering, since the nuclear potential can be represented by a delta function, $V(\mathbf{Q})$ can be represented especially simply, by a scattering length b which depends on the isotope and spin state of the nucleus but not on $\mathbf{Q}$. b is a complex quantity, with its imaginary component corresponding to neutron absorption by the nucleus.

For magnetic neutron scattering, the V matrix elements are more complicated, with a now non-trivial dependence on $\mathbf{Q}$ and the directions of the magnetic moments of the scatterers. To illustrate, the V matrix element for a system with magnetic moments due purely to spin is given by [37]

$$\langle\lambda_f|\sum_l e^{i\mathbf{Q}\cdot\mathbf{r_l}}U_l^{s_i s_f}|\lambda_i\rangle \tag{3}$$

with

$$U_l^{s_i s_f} = \langle s_f|b_l - p_l(\mathbf{Q})\mathbf{S}_{\perp l}\cdot\sigma + B_l\mathbf{I}_l\cdot\sigma|s_i\rangle. \tag{4}$$

b_l is just the nuclear scattering length, and we ignore the third term which involves the nuclear-spin dependence of nuclear scattering to focus on the second term, which involves the magnetic interaction between the neutron and

the material's electrons. (Nuclear magnetic moments are typically too weak to have a significant magnetic scattering contribution.) $\mathbf{S}_{\perp l}$ is the component of the spin $\mathbf{S}$ at the l site that is oriented perpendicular to $\mathbf{Q}$. The coefficient p_l is proportional to $gf(\mathbf{Q})$, where g is the Landé g-factor and $f(\mathbf{Q})$ is the Fourier transform of the normalized unpaired spin density, termed the magnetic form factor. The fact that $f(\mathbf{Q})$ tends to 0 for large $|\mathbf{Q}|$ means that magnetic neutron scattering is usually strongest for small $|\mathbf{Q}|$, in contrast to, for example, neutron scattering from phonons whose intensity tends to increase with $|\mathbf{Q}|$.

The nuclear scattering cross section can often be divided into coherent and incoherent parts. The incoherence is due to the random occupation within a lattice of nuclei with different scattering lengths. Even for a single element, there may be multiple isotopes and nuclear spin states, and they usually occupy an atomic site of a certain type randomly. The fractions of each isotope are usually determined by nature and are listed in tables such as that in Ref. [37], though materials with single isotopes may be obtained, for example, to reduce incoherent scattering (especially if isotopes with zero nuclear spin are chosen) or to avoid the presence of isotopes that have large absorption or incoherent scattering cross sections. For example, hydrogen is well known to have a strong incoherent scattering cross-section, so deuterium is frequently used in place of hydrogen in making samples for neutron scattering. For a set of bound nuclei with no correlations in the occupations of different species at different sites, the incoherent part of $\frac{d\sigma}{d\Omega}$ is isotropic and is proportional to $\overline{|b-\bar{b}|^2}$, whereas the coherent part is proportional to $|\bar{b}|^2$ [38]. For single crystal neutron scattering, the broadness in $\mathbf{Q}$ of the incoherent scattering means that it serves mainly as a source of background noise and is seen as an inconvenience [37].

For a crystal, coherent elastic scattering results in intensity only being present near reciprocal lattice vectors $\mathbf{G}$. Specifically, for elastic nuclear neutron scattering from a perfectly ordered crystal, the coherent cross section is given by

$$\left.\frac{d\sigma}{d\Omega}\right|_{\text{coh}}^{\text{el}} = N\frac{(2\pi)^3}{v_0}\sum_{\mathbf{G}}\delta(\mathbf{Q}-\mathbf{G})|F_N(\mathbf{G})|^2 \tag{5}$$

with

$$F_N(\mathbf{G}) = \sum_j \bar{b}_j e^{i\mathbf{G}\cdot\mathbf{d_j}} e^{-W_j} \tag{6}$$

Here, v_0 is the volume of the unit cell. N is the number of unit cells. j labels

atom sites within each unit cell having positions $\mathbf{d}_j$ and average nuclear scattering lengths $\bar{b}_j$. The Debye-Waller factor is e^{-W_j}, which accounts for the loss of coherence due to random atomic displacements from thermal excitations. $F_N(\mathbf{G})$ is termed the static nuclear structure factor, and it accounts for the variation in the Bragg diffraction peak intensities due to the unit cell having more than one atom. When a Bragg peak at $\mathbf{G}$ is forbidden by the symmetry of the crystal, $F_N(\mathbf{G}) = 0$. If short-range order is present, then a spread of elastic or near-elastic spectral weight beyond the Bragg peaks originating from the long-range crystalline order (the "diffuse scattering") may be seen. Incoherent elastic scattering is usually also present, manifesting as a sharp peak in energy at $\hbar\omega = 0$ meV for all $\mathbf{Q}$.

For magnetic elastic neutron scattering, a similar expression to (5) can be derived. In this case, except for ferromagnetic materials, the magnetic unit cell is generally larger than the structural unit cell and has additional reciprocal lattice vectors. Also, the static nuclear structure factor is replaced by the static magnetic structure factor, with the essential difference being that the b_j in (6) is replaced by $p_j(\mathbf{Q})\mathbf{S}_{\perp j}$.

For inelastic scattering, we have

$$\left.\frac{d^2\sigma}{d\Omega_f dE_f}\right|_{\text{coh}}^{\text{inel}} = N\frac{k_f}{k_i}\frac{1}{4\pi}S(\mathbf{Q},\omega). \tag{7}$$

($k_f = |\mathbf{k}_f|$ and $k_i = |\mathbf{k}_i|$.) $S(\mathbf{Q},\omega)$ is called the scattering function.

Generally, a harmonic crystal in 3-dimensional space will have $3n$ branches of vibrational modes, where n is the number of atoms in the unit cell. The frequencies can be labeled $\omega_{\mathbf{q}s}$, where $\mathbf{q}$ is the wavevector relative to the nearest Brillouin zone center, and s labels each of the $3n$ modes. Each mode will have a $3n$-dimensional polarization vector $\xi_{\mathbf{q},js}$.

When measuring phonons by neutron scattering, it is convenient to separate $S(\mathbf{Q},\omega)$ into

$$S(\mathbf{Q},\omega) = \chi''(\mathbf{Q},\omega)(n(\omega,T)+1). \tag{8}$$

$\chi''(\mathbf{Q},\omega)$ is the imaginary part of the dynamical susceptibility, and for harmonic phonons this factor is conveniently temperature-independent. $n(\omega,T) = 1/(e^{\hbar\omega/k_BT}-1)$ is the Bose factor and T is the temperature. For scattering resulting in the creation of a single harmonic phonon, we have

$$\chi''(\mathbf{Q},\omega) = \frac{1}{2}\frac{(2\pi)^3}{v_0}\sum_{\mathbf{G},\mathbf{q}}\delta(\mathbf{Q}-\mathbf{q}-\mathbf{G})\sum_s \frac{|\mathscr{F}(\mathbf{Q})|^2}{\omega_{\mathbf{q}s}}[\delta(\omega-\omega_{\mathbf{q}s})] \tag{9}$$

$\mathscr{F}(\mathbf{Q})$ is the dynamic nuclear structure factor, which is given by

$$\mathscr{F}(\mathbf{Q}) = \sum_j \frac{\bar{b}_j}{\sqrt{m_j}}(\mathbf{Q}\cdot\xi_{\mathbf{q},js})e^{i\mathbf{Q}\cdot\mathbf{d}_j}e^{-W_j}. \tag{10}$$

m_j is the mass of the jth atom in the unit cell. Unlike the static nuclear structure factor, the dynamic nuclear structure factor depends on the masses of the atoms and the amplitude of their oscillations in the form of the polarization vectors. These structure factors are related, though, in the limit of $\mathbf{q}\to\mathbf{0}$:

$$\lim_{\mathbf{q}\to\mathbf{0}}|\mathscr{F}(\mathbf{Q})|^2 = \frac{|\mathbf{G}|^2}{M}|F_N(\mathbf{G})|^2 \tag{11}$$

where $M = \sum_j m_j$. Generally, vibrational modes will not be true eigenstates due to damping, and the phonon mode will have a Lorentzian lineshape rather than a delta function for scans along energy if resolution-broadening is ignored.

For inelastic magnetic scattering, a variety of phenomena can occur. One common type of magnetic excitations that occurs in magnetically ordered structures is spin waves, which may involve ferromagnetic or antiferromagnetic correlations between neighboring spins. Ferromagnetic spin waves disperse quadratically from Bragg peak locations, whereas antiferromagnetic spin waves disperse linearly from magnetic Bragg peaks. The expression for the scattering intensity of antiferromagnetic spin waves is similar to that of phonons in terms of temperature- and energy transfer-dependence, whereas the intensity expression for ferromagnetic spin waves lacks the $1/\omega$ factor seen in Equation 9. Magnetic excitations can sometimes also be observed in the absence of magnetic ordering. For example, magnetic excitations can be seen in hole-doped cuprate superconductors in the form of an "hour-glass dispersion" near the wavevectors of the antiferromagnetic spin waves in the corresponding undoped compound [21], and in the $Fe_{1+y}Te_{1-x}Se_x$ family of iron-based superconductors, diffuse magnetic excitations can be seen whose details vary depending on the temperature and whether the sample can host superconductivity [39].

In experiments, the effect of the resolution of the instrument may be nontrivial. It may be accounted for by convolving the measured $S(\mathbf{Q},\omega)$ with a resolution function $R(\mathbf{Q}-\mathbf{Q}_0,\omega-\omega_0)$. Usually, the resolution function is thought of as a Gaussian function defined in 4-dimensional $(\mathbf{Q},\hbar\omega)$ space. The resolution function is generally anisotropic, and a feature that is sharp

as seen along $\hbar\omega$ for fixed $\mathbf{Q}$ may appear broad for a different, theoretically equivalent wavevector; such considerations may need to be taken into account when choosing where in $(\mathbf{Q}, \hbar\omega)$ space to take measurements. Broadening may also be due to the "mosaic", which is the spread in domain orientations in a real (i.e., imperfect) crystal.

2.2.3 Neutron scattering techniques used in this thesis

For the research in this thesis, a number of neutron scattering techniques were used. In Section 4, to study the phonons of the $Fe_{1+y}Te_{1-x}Se_x$ family of iron-based superconductors, we used time-of-flight spectroscopy at HYSPEC[3] and triple-axis spectroscopy at MACS and BT7[4]. In Section 5, to study the magnetic excitations in the cuprate superconductor $La_{1.9}Ca_{1.1}Cu_2O_{6+\delta}$, we used time-of-flight spectroscopy at SEQUOIA[5]. In Section 6, to study changes in short-range order and lattice vibrations in the relaxor ferroelectric 68%$PbMg_{1/3}Nb_{2/3}O_3$-32%$PbTiO_3$, we used time-of-flight spectroscopy at HYSPEC.

[3]HYSPEC is an instrument in the Spallation Neutron Source at Oak Ridge National Laboratory in Oak Ridge, TN.

[4]MACS and BT7 are instruments in the NIST Center for Neutron Research at the National Institute of Standards and Technology in Gaithersburg, MD

[5]SEQUOIA is an instrument in the Spallation Neutron Source at Oak Ridge National Laboratory in Oak Ridge, TN.

2.3 Overview of topological materials

As motivation for the research on $Cu_xBi_2Se_3$, the proposed topological superconductor discussed in Section 3, this section gives a broad overview of materials with topologically nontrivial electronic structures.

Topological insulators (TIs) are materials with a topologically nontrivial electronic structure and a complete band gap.[6] For a perfect crystal, in the absence of effective electron-electron interactions, the Hamiltonian H for a single electron can be decomposed into matrices $H(\mathbf{k})$, i.e.,

$$H = \sum_{\mathbf{k}} (c^\dagger_{1,\mathbf{k}} c^\dagger_{2,\mathbf{k}} ...) H(\mathbf{k}) \begin{pmatrix} c_{1,\mathbf{k}} \\ c_{2,\mathbf{k}} \\ ... \end{pmatrix}, \tag{12}$$

where $c_{j,\mathbf{k}}$ and $c^\dagger_{j,\mathbf{k}}$ are creation and annihilation operators for an electron with wavevector $\mathbf{k}$ in band j. If n bands are considered, the $H(\mathbf{k})$ are each an $n \times n$ matrix. Due to the translational symmetries of the crystal, these matrices obey the periodicity $H(\mathbf{k}) = H(\mathbf{k} + \mathbf{G})$ for any reciprocal lattice vector $\mathbf{G}$. The band structure thus represents a mapping from $\mathbf{k}$ defined on a D-dimensional torus to $H(\mathbf{k})$, where D is the number of dimensions of the reciprocal space [4]. Topological invariants can be defined for $H(\mathbf{k})$, forming equivalence classes of band structures that can be smoothly deformed to each other while still maintaining the same invariant [4]. These topological invariants are only well-defined if a gap is maintained throughout the Brillouin zone.

Topological superconductors (and topological superfluids) also have an energy gap[7], and they can be described in a mathematically similar way, but with an additional particle-hole symmetry. For example, for a BCS mean-field theory of a system of spinless electrons, the Hamiltonian can be written [4]

$$H - \mu N = \frac{1}{2} \sum_{\mathbf{k}} (c^\dagger_{\mathbf{k}} c_{-\mathbf{k}}) H_{BdG}(\mathbf{k}) \begin{pmatrix} c_{\mathbf{k}} \\ c^\dagger_{-\mathbf{k}} \end{pmatrix}, \tag{13}$$

[6] Semimetals with full band gaps can also be topologically nontrivial in the same way as TIs, though insulators are often more desirable for applications and research. Confusingly, "topological semimetals" may refer to Dirac or Weyl semimetals, which are distinct from "topological insulators", though they will be briefly discussed as well.

[7] For time-reversal-invariant superconductors, the topological invariant can be extended to superconductors with point nodes in their gap [3].

where $c_{\mathbf{k}}^{\dagger}$ and $c_{\mathbf{k}}$ are electron creation and annihilation operators written as a vector in Nambu's notation, μ is the chemical potential, N is the number of electrons in the system, and H_{BdG} is the Bogoliubov-de Gennes 2×2 block matrix [4]. $H_{BdG}(\mathbf{k})$ is given by

$$H_{BdG}(\mathbf{k}) = (H(\mathbf{k}) - \mu)\tau_z + \Delta_1(\mathbf{k})\tau_x + \Delta_2(\mathbf{k})\tau_y, \tag{14}$$

where τ_x, τ_y, and τ_z are Pauli matrices, $H(\mathbf{k})$ is the Bloch Hamiltonian, and $\Delta_1(\mathbf{k})$ and $\Delta_2(\mathbf{k})$ define the pairing interaction. $H_{BdG}(\mathbf{k})$ plays a similar role for classifying topological superconductors as $H(\mathbf{k})$ plays for topological insulators. ^{3}He-B is an example of a 3D TR-invariant topological superfluid [40], and a number of candidate topological superconductors have been proposed, such as $Sn_{1-x}In_xTe$ [41] and $Cu_xBi_2Se_3$ [2] (the subject of Section 3).

Topological invariants can be specified by a "periodic table" according to the material's dimensionality and the eigenvalues of time-reversal (TR) and particle-hole swapping operators when these symmetries are obeyed [4]. If Θ denotes the time-reversal operator, and $\Xi = \tau_x K$ denotes the particle-hole swapping operator with K being complex conjugation, then TR symmetry would require that

$$\Theta H(\mathbf{k})\Theta^{-1} = H(-\mathbf{k}) \tag{15}$$

and particle-hole symmetry would require that

$$\Xi H_{BdG}(\mathbf{k})\Xi^{-1} = -H_{BdG}(-\mathbf{k}). \tag{16}$$

The topological invariants, if allowed to be nontrivial, have either a $\mathbb{Z}$ form, meaning they may take on integer values, or a $\mathbb{Z}_2$ form, meaning they can only take on two values. To give a concrete example, a 2D TR symmetry-breaking system (i.e., the quantum Hall state) can be described by a $\mathbb{Z}$ invariant given by a line integral of the Berry phase $i\langle u_m(\mathbf{k})|\nabla_{\mathbf{k}}|u_m(\mathbf{k})\rangle$, where $|u_m(\mathbf{k})\rangle$ is an eigenstate of $H(\mathbf{k})$ and $\nabla_{\mathbf{k}}$ is the gradient in $\mathbf{k}$-space. This "Chern invariant" has been used to explain the quantized Hall conductivity σ_{xy} in the integer quantum Hall effect [42]. Other examples of topological invariants include the $\mathbb{Z}_2$ invariants for 3D TR-invariant insulators and the $\mathbb{Z}$ invariant for 3D TR-invariant superconductors.

The surface and edge states that are expected to exist between regions of different topological invariants can be described by a **bulk-boundary correspondance**, the relation between the bulk topology and how surface or edge bands are connected on the boundary. If we consider a region in

space moving from the bulk of a topologically nontrivial material to the bulk of a topologically trivial space (which includes the gas or vacuum outside the sample [4]), the topological invariant for this region must become undefined near the interface. This can happen if the conduction and valence bands meet, resulting in gapless boundary states [43]. The constraints on the boundary states vary according to symmetries which must be obeyed and the dimensionality of the boundary. For instance, in systems obeying TR symmetry, surface or edge states at time-reversal-invariant momenta (TRIM) are required by Kramers' theorem to be at least doubly degenerate. In the absence of spin-orbit coupling, all states would be degenerate, but with spin-orbit coupling Kramers pairs of states may split from each other for any non-TRIM wavevector, and the way these Kramers pairs are connected to each other in reciprocal space corresponds to the topology of the bulk.

An important concept for applications, beyond the simple existence of topological boundary states, is that of **topological protection**, where topology and symmetry considerations result in elastic backscattering from nonmagnetic impurities being forbidden. For example, a time-reversal-invariant 2D topological insulator, also known as the quantum spin Hall state, has helical edge states, in which states with opposite spins propagate in opposite directions [43]. Non-spin-flip elastic backscattering is forbidden since there are no backward-moving edge states with the same spin and opposite momenta as the forward-moving states. (Inelastic scattering, however, is still possible [4].) Thus, the surface states that arise from the topologically nontrivial nature of the bulk are protected by the system's time-reversal symmetry. Similar considerations also apply to the surface states of 3D topological TR-invariant insulators, with some complications. First, there are now four $\mathbb{Z}_2$ topological invariants for 3D TR-invariant TIs, rather than the single $\mathbb{Z}_2$ invariant for 2D TR-invariant TIs. Only if a certain one of these invariants is nontrivial does one have a "strong TI", where surface states are protected by TR symmetry; other sets of nontrivial topological invariant values lead merely to a "weak TI" with non-robust surface states that are not protected by TR symmetry[4]. Second, in addition to the absence of backscattering, the presence of disorder on the surface states of these 3D materials results in weak antilocalization [4]. For strong TIs, evidence for the absence of backscattering despite the presence of disorder has been reported, for example, in a study on the TI $Bi_{0.92}Sb_{0.08}$ with spin-resolved angle-resolved photoemission spectroscopy and quasiparticle interference [44].

In addition to TR-symmetry and particle-hole symmetry, additional topo-

logical invariants have been found for other symmetries. For example, **topological crystalline insulators** (TCIs) are insulators which have topological surface states on high-symmetry crystal surfaces that are protected by both TR and certain point group symmetries [45]. TCIs need not have spin-orbit coupling (necessary for the TR-invariant TIs discussed above). Instead of the TR-invariant momenta in the reciprocal space of the surface, we consider momenta that are invariant with respect to both TR and certain point group symmetries, such as reflection or rotational symmetries. The way the boundary bands are connected between these symmetry-invariant momenta corresponds to the bulk TCI topological invariant (which is also of type $\mathbb{Z}_2$). However, these momenta are only invariant with respect to the point group symmetries if the surface obeys these symmetries, which means robust TCI surface states may only be found on certain high-symmetry surfaces. One example of a TCI is SnTe, which was theoretically proposed as such [46], with experimental confirmation soon after [47]. It may also be possible for a material to be simultaneously a TI and a TCI, as recently claimed for BiTe [48]. Aside from TIs, TCIs, and topological superconductors, topologically nontrivial materials have also been classified according to other symmetries, such as combined particle-hole and mirror symmetry [49], magnetic symmetries [50, 51], and non-symmorphic space group symmetries [52, 53].

There is a close relation between Dirac fermions and topological materials, so here I will briefly describe Dirac and Weyl semimetals. Dirac fermions are solutions to the Dirac equation. When the mass is zero, the Dirac equation can be split into two Weyl equations, whose solutions represent Weyl fermions [54]. The band structure of graphene is known to have conical dispersions which can be thought of as 2D massless Dirac fermions, and we have already discussed the similar 2D conical dispersion on the surface of TIs, but it is also possible to have 3D massless dispersions in the bulk of materials[8]. We can consider a Hamiltonian which can be split into $H(\mathbf{k})$ for each $\mathbf{k}$, and if we consider two spin and two orbital degrees of freedom near where two bands may touch, the $H(\mathbf{k})$ will be 4×4 matrices. The $H(\mathbf{k})$ can generally be decomposed in terms of an identity matrix and four 4×4 Dirac matrices [54]. In three dimensions, with no imposed symmetries, we generally cannot expect accidental degeneracies to be present. However, if additional

[8] 3D *massive* Dirac dispersions may also be present in materials such as bismuth, where their presence has been used to explain unusual properties such as bismuth's large diamagnetism [55].

crystallographic symmetries are imposed, then Dirac points with 3D massless dispersion relations are allowed in materials known as **Dirac semimetals** [56]. 3D Dirac semimetals are also predicted to exist on a phase boundary between phases with different topological invariants, but in this case tuning of parameters is required. **Weyl semimetals**, having 3D Weyl fermions, may also exist, provided that TR- and inversion-invariance are not both present [57]. Weyl semimetals are unusual in that Fermi arcs are predicted on the material's boundary [57]. Experimental verification of the existence of Dirac and Weyl semimetals has recently been reported; for example, TaAs was reported to be a Weyl semimetal [58, 59] and Na_3Bi was reported to be a Dirac semimetal [60].

Unusual quasiparticles known as **Majorana fermions** can arise on boundaries in a number of situations, usually when superconductivity is present. Majorana fermions have unique properties such as being their own antiparticles. Single $E = 0$ states of superconductors provide an example of Majorana modes. Due to the particle-hole symmetry of superconductors, for each state at energy $E \neq 0$, there must be another state at energy $-E$ generated by the particle-hole swapping operator Ξ, but at $E = 0$ a single state may exist on its own [4]. Such a nondegenerate $E = 0$ state, if it exists, must be a Majorana mode [61]. Generally, any Dirac fermion creation or annihilation operator can be written as a superposition of two Majorana creation operators, so any system of electrons can formally be written in terms of Majorana fermions, but if a pair of Majorana modes becomes spatially separated, then a description in terms of Majorana fermions becomes a natural way to account for the physical degrees of freedom in the system [61]. Single $E = 0$ modes are topologically protected as long as an energy gap (called a "minigap") exists between the $E = 0$ state and other excitations [61]. The reason for this protection is that, if the Hamiltonian is deformed adiabatically, this single $E = 0$ state cannot be perturbed into a state with $E \neq 0$ energy because a discontinuous change would be required in the form of the creation of a second state at $-E$. For a pair of $E = 0$ Majorana states, there is a splitting of these states' energies as the Majorana modes are brought close to each other, so separation of $E = 0$ Majorana states (which always come in pairs in real systems) is necessary to take advantage of their topological protection.

Numerous systems involving superconductors have been proposed to host Majorana fermions [62]. Examples of 1-dimensional systems that may host Majorana fermions include the edge of a 2D TR-invariant TI, a 3-dimensional

TI nanowire threaded by magnetic flux, a semiconductor quantum wire with spin-orbit coupling, and a helical spin chain formed by magnetic impurity atoms on a superconductor [61]. Superconductivity is introduced in these examples via the proximity effect. The $E = 0$ Majorana states are localized at each end.[9] An important example in 2 dimensions was introduced by Fu and Kane [63]. They proposed a model in which the surface of a 3D TR-invariant strong TI is covered by an s-wave superconductor, causing pairing in the TI due to the superconducting proximity effect. In their model, the eigenstates for a region centered on a vortex were found to be Majorana modes. Another example is in 3D TR-invariant topological superconductors, which have been said to have gapless counterpropagating Majorana states on their surface (albeit states which are delocalized and are thus less useful for quantum computation [64]) and a pair of Majorana zero modes bound to each superconducting vortex [65].

Majorana fermions bound to superconducting vortices in 2-dimensional systems exhibit non-Abelian exchange statistics, though it should be emphasized that free Majorana fermions obey ordinary fermionic statistics [66]. Though well-separated Majorana fermions do not cause a significant splitting of their $E = 0$ states, being robust to local perturbations, the relative phases of these modes in vortices gives rise to non-Abelian exchange statistics. Exchange can occur if two vortices encircle each other, and the non-Abelian statistics of the system as a whole allows these states to be manipulated globally while being immune to local perturbations. The robustness of manipulating Majorana fermions in vortices (or states with anyonic statistics in general [67]) have been proposed for use in "topological quantum computation" [63, 68]. Quantum computation is when quantum states are manipulated rather than the classical two-state systems in traditional computing. The excitement around quantum computation is due to the discovery of certain algorithms that can scale more efficiently than known classical counterparts, such as Shor's algorithm for factoring prime numbers [69]. Topological quantum computation is the manipulation of quantum states that are robust with respect to local perturbations due to the system having non-Abelian exchange statistics [61]. However, it is known that manipulations in topological quantum computation are not enough to implement a universal quantum

[9] In the 2D TR-invariant TI, the "ends" are the locations of junctions between the TI, a superconductor, and a ferromagnet needed to break TR-symmetry so Kramers' theorem does not forbid an unpaired $E = 0$ state.

computer, and non-topologically protected manipulations may be necessary [61].

The discussion so far has focused on abstract concepts, but consideration of the materials that might host these properties is also important. A large list of discovered TIs and TCIs as of May 2013 can be found in Ref. [55]. For TIs and TCIs, the prediction of materials has been fairly successful. For example, members of $Bi_{1-x}Sb_x$ and Bi_2Te_3 were predicted to be TIs [70] before experimental confirmation followed in the form of angle-resolved photoemission spectroscopy (ARPES) measurement of the conical dispersion of the surface states[10] [72, 73]. Some guidelines have been developed for predicting TIs [74]. Essentially, we can start by picturing a system that is a semimetal or a small-band-gap semiconductor. One guideline is to have strong covalency between the orbitals near the Fermi energy, which can arise between two elements with similar electronegativities. In a tight-binding band theory picture, before the mixing is considered, the conduction and valence bands would be flat and have contributions solely from each of the two elements involved. The covalency would then introduce a hybridization between states of each band, especially those near the top of the valence band and the bottom of the conduction band. Next, spin-orbit coupling may open a band gap. A balance is needed between having covalency that is too strong for spin-orbit coupling to open a gap, and an initial band gap that is too large for sufficient mixing of states to occur. Since spin-orbit coupling tends to be largest for materials with heavy atoms, the discovered TI and TCI materials tend to have heavy elements in them; the list of known TIs and TCIs in Ref. [55] all include at least one element from the 4th or 5th rows of the periodic table.

In addition to guidelines for the existence of TIs, there are also materials considerations that affect whether the TIs will be useful for studying their surface states [75]. For example, the tetradymite $(Bi_{1-x}Sb_x)_2(Te_{1-y}Se_y)_3$ family of materials, which are nominally intrinsic semiconductors, nevertheless tend to have defects such as Se/Te vacancies or antisite defects where Bi/Sb occupy Se/Te sites [74]; these defects can introduce charge carriers that make the bulk conducting and mask potential surface transport properties. Also, while the surface states of a 3D TI should have a conical dispersion, the vertex of this dispersion may be located within the energy range of the va-

[10]Spin-resolved ARPES has also been useful to verify the predicted spin-momentum locking of surface states, e.g., in $Bi_{1-x}Sb_x$ [71].

lence or conduction bands, which would also make it difficult to measure the transport properties intrinsic to the surface's 2D massless Dirac dispersion.

No materials have yet been verified to have topological superconductivity[11], but there are candidate compounds and some helpful criteria to identify future possibilities. For example, in 3D TR-invariant topological superconductors, if the superconducting energy gap is much smaller than the Fermi energy, which is usually the case, then the topological invariant can be determined from the Fermi surface topology and the pairing gap symmetry [77]. This criterion becomes simpler if inversion symmetry is present, splitting pairing symmetries into odd-parity and even-parity. It can be shown that even-parity superconductors are topologically trivial [2, 78]. Odd-parity superconductivity, on the other hand, is guaranteed if the Fermi surface encloses an odd number of time-reversal invariant momenta, and possible even when this is not the case, provided that the signs of the superconducting order parameter on different Fermi pockets are the same. Unfortunately, few examples of odd-parity superconductors are known, especially if one requires TR-invariance [77]. The requirement of odd-parity (and thus unconventional) superconductivity for inversion-symmetric TR-invariant topological superconductors has been, thus far, the primary way of attempting to identify a topological superconductor. For example, unconventional superconductors are expected to host Andreev bound states which can be detected in the form of zero-bias conductance peaks in scanning tunneling spectroscopy or point-contact measurements data (for example, in $Cu_xBi_2Se_3$ [3, 79–82] or $Sn_{1-x}In_xTe$ [41]).

Candidate TR-invariant topological superconductors include $Cu_xBi_2Se_3$ [1–3], $Sn_{1-x}In_xTe$ [41], $Cu_x(PbSe)_5(Bi_2Se_3)_6$ [83], and numerous others. Most of the proposed topological superconductors have been materials arising from other topologically nontrivial materials, such as doped TIs. Possible reasons for investigating doped TIs may include the common importance of spin-orbit coupling in TIs and in theories of topological superconductivity [2], or the fact that a doped TI may still have a 2D topologically nontrivial superconducting state even if the bulk is a topologically trivial superconductor, as in Fu and Kane's model[12] [63].

$Cu_xBi_2Se_3$, despite being one of the major candidates for topological su-

[11] although the B phase of liquid ^{3}He has been described as a topological superfluid [76]

[12] provided that the necessary doping has not destroyed the topological character of the bulk band structure [64]

perconductivity, unfortunately has the problem that it is very inhomogeneous, with diamagnetic shielding fractions varying substantially from sample to sample. In Section 3, I present our research into the effects of various materials synthesis conditions on the superconductivity in this compound.

3 Dependence of superconductivity in $Cu_xBi_2Se_3$ on quenching conditions

In this Section, I present our research on the shielding fractions obtained in the proposed topological superconductor $Cu_xBi_2Se_3$ under various materials synthesis conditions, noting especially the importance of quenching. This section is largely reprinted from Ref. [84]; copyright is held by the American Physical Society. Coauthors include myself, Ruidan Zhong, Zhijun Xu, Genda Gu, and John Tranquada of Brookhaven National Laboratory.

3.1 Abstract

Topological superconductivity, implying gapless protected surface states, has recently been proposed to exist in the compound $Cu_xBi_2Se_3$. Unfortunately, low diamagnetic shielding fractions and considerable inhomogeneity have been reported in this compound. In an attempt to understand and improve on the finite superconducting volume fractions, we have investigated the effects of various growth and post-annealing conditions. With a melt-growth (MG) method, diamagnetic shielding fractions of up to 56% in $Cu_{0.3}Bi_2Se_3$ have been obtained, the highest value reported for this method. We investigate the efficacy of various quenching and annealing conditions, finding that quenching from temperatures above 560°C is essential for superconductivity, whereas quenching from lower temperatures or not quenching at all is detrimental. A modified floating zone (FZ) method yielded large single crystals but little superconductivity. Even after annealing and quenching, FZ-grown samples had much less chance of being superconducting than MG-grown samples. From the low shielding fractions in FZ-grown samples and the quenching dependence, we suggest that a metastable secondary phase having a small volume fraction in most of the samples may be responsible for the superconductivity.

3.2 Introduction

Materials with topologically nontrivial electronic structures have gained a great deal of attention recently, both for their unique physics and for their potential applications. Whereas conventional insulators or superconductors can be adiabatically transformed into topologically trivial states [4, 77],

symmetry-protected topological insulators (TI) and superconductors (TSC) [40, 43, 65, 76, 85] cannot be so transformed without breaking certain symmetries, resulting in surface states robust to many kinds of perturbations. For example, the surfaces of time-reversal invariant TSCs would host Majorana fermions, which are potentially useful for the low decoherence needed for quantum computation and are also desirable for investigating their unique properties, such as being their own antiparticles [62, 63, 68].

The recently discovered [1] compound $Cu_xBi_2Se_3$, in which Cu is intercalated between layers of the TI Bi_2Se_3, was soon proposed to be a TSC [2]. Many experiments have probed topological properties in this material, with mixed findings. The strongest evidence thus far for TSC has come from point-contact spectroscopy data [3, 79, 80] showing zero-bias conductance peaks (ZBCPs) that may be indicative of unconventional superconductivity. Calculations showed that, for a two-orbital model of the band structure, every possible unconventional pairing symmetry should be topologically nontrivial [2, 3], suggesting that $Cu_xBi_2Se_3$ could be a TSC. On the other hand, scanning tunneling spectroscopy measurements [81] showed no such peaks except when superconductor-insulator-superconductor junctions were accidentally formed, suggesting that $Cu_xBi_2Se_3$ is instead an s-wave superconductor and highlighting the difficulties in making point-contact measurements on $Cu_xBi_2Se_3$. In addition, spectroscopy with normal-metal/superconductor junctions [82] showed ZBCPs for a transparent barrier but not for a finite barrier, raising more doubts about unconventional superconductivity in $Cu_xBi_2Se_3$. On the other hand, one theoretical study [86] suggested that the link between unconventional superconductivity and a ZBCP is not as simple as earlier suggested, and that an odd-parity superconductor with a cylindrical Fermi surface could account for a peak absence. Findings from ARPES experiments have also been mixed, with the finding of a conical dispersion relation for $Cu_{0.12}Bi_2Se_3$[64, 87–91] and other characteristics of the band structure seen as favoring TSC, but a later study showing that the Fermi surface encloses an even number of time-reversal invariant momentum points casting doubt on TSC[91]. In addition, specific heat data [92], nuclear magnetic resonance data [93], and what have been claimed as anomalously high superconducting transition temperatures ($T_C \sim 3.5$ K) for the measured carrier concentrations ($\sim 10^{-20}$ cm^{-3}) [1, 77, 92] have been interpreted as favoring TSC, though the specific heat behavior may have a more conventional explanation [94].

Unfortunately, the large inhomogeneity and low diamagnetic shielding

fractions of crystals have contributed to the difficulty in studying this compound, and it would be highly desirable to improve crystal quality and obtain clearer results. Since the discoverers of $Cu_xBi_2Se_3$ reported only a 20% shielding fraction at their lowest achievable temperature [1] and did not show zero resistance, there have been doubts as to the bulk nature of the superconductivity [92]. They used a melt-growth method, where one seals Cu, Bi, and Se in a quartz ampoule, heats to the melting point, slowly cools the mixture as crystallization occurs, then quenches. Other groups [79, 95, 96] used similar methods, obtaining similar shielding fractions, and two of these groups [79, 96] were able to measure zero resistance in their samples. More recently, a superconducting fraction of 35% was reported for the melt-growth method [97]. A different method involving quenching from the liquid state while using precursor ingredients to avoid Cu_2Se production [98] has also been reported to improve shielding fraction. Alternatively, an electrochemical method has been used [77, 99] to intercalate Cu in pre-grown Bi_2Se_3 crystals, with reported zero resistance, shielding fractions of up to $\sim$70%, and specific heat data indicating bulk superconductivity.

In this paper, we report the effects of various growth conditions on diamagnetic shielding fraction in $Cu_xBi_2Se_3$, highlighting changes in conditions that result in qualitative increases in the likelihood of superconductivity. We have found shielding fractions as high as 56%, showing that it is possible to obtain substantial shielding fractions using the melt-growth method; however, while the occurrence of superconductivity is generally reproducible, the magnitude of the shielding fraction is not. We investigated the effects of various quenching and annealing conditions, highlighting the importance of quenching, which has been investigated in detail for the electrochemical [99] and quench-from-liquid [98] methods and prescribed but not studied in detail for the melt-growth method [1]. While not quenching results in little superconductivity, its effects appear to be reversible by subsequent annealing and quenching. Annealing at temperatures of 560°C or higher before quenching was found to be essential for superconductivity, whereas somewhat lower temperatures were actually detrimental to superconductivity. Large single crystals of $Cu_xBi_2Se_3$ grown by the floating zone method are generally non-superconducting. These observations suggest that the phase responsible for the superconductivity is metastable.

The rest of the paper is organized as follows. In the next section, we describe the methods we used for sample growth and treatment, as well as the characterization methods. In Sec. III, we present our results. Their signifi-

cance is discussed in Sec. IV, where we point out similarities with $K_xFe_{2-y}Se_2$, another system for which quenching is essential for achieving superconductivity. A brief conclusion is given in Sec. V.

3.3 Materials and methods

We used two growth methods, the melt-growth (MG) method and a modified floating-zone growth (FZ) method. For the MG method [1], stoichiometric amounts of Cu, Bi, and Se were sealed in an ampoule that was sealed within another ampoule (double-sealed) under 0.2 bar Ar, then the ampoule was placed horizontally in a small box furnace, heated well above the melting point to 840°C, jostled to mix the ingredients, cooled to 640°C at 18°C/h, and then quenched in liquid nitrogen. The inner ampoules were 2mm thick, had 10 mm inner diameter, and were ∼15 cm long; the outer ampoules had similar dimensions and were 1mm thick. Typically, $Cu_xBi_2Se_3$ was made this way in 50g batches. For the FZ method, stoichiometric amounts of Cu, Bi, and Se were vertically premelted in an ampoule (sealed similarly to the MG method), then zone-melted from bottom to top in-ampoule using an image furnace at a rate of 0.6 mm/h, resulting in single crystals of up to several cm in length. For samples grown by both the MG and FZ methods, the impact of post-annealing (hereafter, "annealing") was explored, where pieces were sealed in a single ampoule (typically, 1mm thick, 10mm inner diameter, and ∼15 cm long) under 0.2 bar Ar, heated at 580°C for 4 h, then quenched in liquid nitrogen. For all growth methods, the Cu, Bi, and Se were of purities 99.999%, 99.999%, and 99.995%, respectively, and used without pretreatment.

There have been a number of reports on the best choice of Cu concentration x for superconductivity, with superconductivity found within $0.1 \leq x \leq 0.3$ for the MG method [1], $0.1 \leq x \leq 0.6$ for the electrochemical method [99], and $0.03 \leq x \leq 0.5$ for a quench-from-liquid method [98]. Our preliminary data suggested $0.25 \leq x \leq 0.35$ as an optimal range, so we have focused our efforts on $x = 0.3$ when comparing different growth and post-annealing conditions.

For magnetic measurements, we used a SQUID magnetometer[13], with the field H applied within the cleavage plane ($H \perp c$) to minimize the demagneti-

[13]Specifically, we used a Magnetic Properties Measurement System instrument purchased from Quantum Design, Inc.

zation effect. To mitigate the effect of magnetic relaxation [95], we waited 30 seconds after applying the field before measuring the magnetic response. To calculate shielding fraction, we took data under zero-field cooling at $T = 1.7$ K for at least two different fields within $0 < H \leq 2$ Oe, and used the slope of the line fit through these points, the sample's mass, and the density to calculate the shielding fraction. The density was determined from a cylindrical piece of an FZ ingot of nominal $Cu_{0.35}Bi_2Se_3$ composition. For the resistance measurements, the four-probe method was used with current applied in the *ab*-plane. The temperature was controlled by the magnetometer cryostat. We performed annealing on pieces thicker than 1 mm and then cleaved samples from the inside of these pieces for measurement. A direct comparison of the superconducting properties of cleaved samples before and after annealing was not possible since annealing thin (< 1 mm) samples invariably resulted in loss of superconductivity. We suspect this loss was due to preferential evaporation of Se, which was proposed to be responsible for the n-type doping of Bi_2Se_3 [73, 100]. To characterize the composition of our materials, we used a JEOL 7600F scanning electron microscope (SEM) equipped with energy-dispersive X-ray (EDX) analysis capabilities located at the Center for Functional Nanomaterials at Brookhaven National Laboratory. The compositions measured as a function of position are reported in Fig. 5; in contrast, the values of Cu concentration cited in the text are generally the nominal concentrations, corresponding to the elemental mixtures from which samples were grown.

3.4 Results

In Fig. 5(a) the resistance parallel to the *ab*-plane is plotted as a function of temperature for a sample with $x = 0.35$. Each plotted resistance point corresponds to the average of ten consecutive measurements; error bars show standard deviation. The resistance drops to nearly zero from roughly 3.4 to 3.0 K, indicating superconductivity, with a small further decrease down to 1.7 K. Magnetoresistance measurements (not shown) indicated that B_{c2} is between 1 and 7 T, consistent with previous reports [1, 81, 92].

In Fig. 5(b), we plot susceptibility as a function of temperature for a 2.2 mg sample with $x = 0.25$ having $T_c \approx 3.5$ K and a shielding fraction of $\sim$30% at 1.7 K. The applied field was $H = 2$ Oe with $H \perp c$. The magnetization has a broad transition and seems likely to continue dropping well below $\sim$1.7 K, our lowest achievable temperature. We have seen similarly broad curves

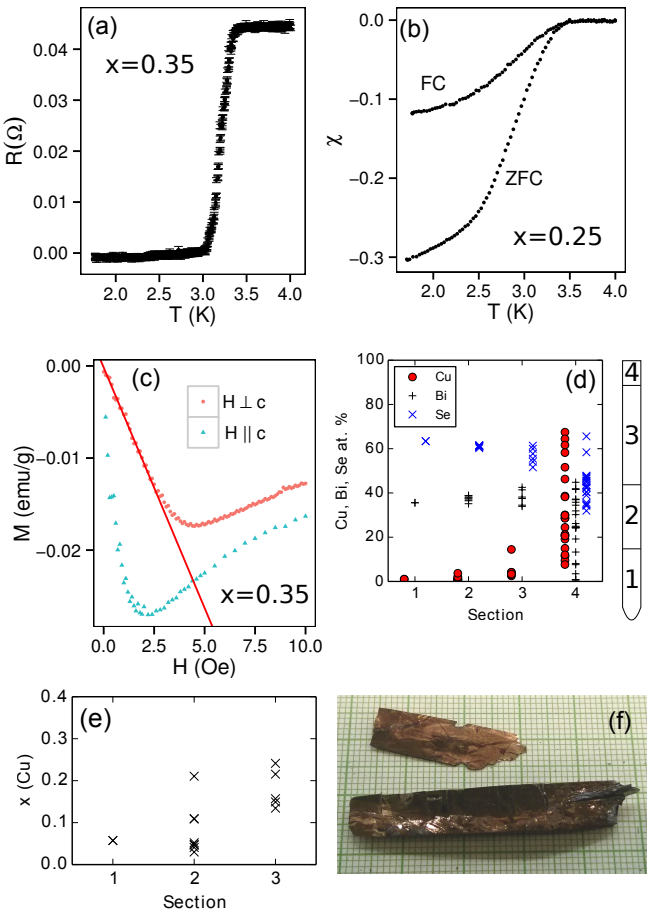

Figure 5: (a) Resistance vs. temperature for a single crystal of $x = 0.35$. (b) Magnetic susceptibility χ vs. temperature for a single crystal with $x = 0.25$, 2.2 mg, and ∼30% shielding fraction at 1.7 K. The applied field was 2 Oe with $H \perp c$, with both ZFC and field cooling (FC) shown. (c) Magnetization curve for a single crystal with $x = 0.35$ near 1.7 K, for both $H \perp c$ and $H \parallel c$, under zero field cooling (ZFC); the shielding fraction was found to be 48% at 1.7 K. The best-fit line used for shielding fraction calculation has been plotted. In (b) and (c), two measurements were taken at each field and temperature respectively, then averaged and plotted. (d,e) Composition as determined by EDX measurements for samples taken from different sections of an $x = 0.25$ FZ ingot. The sections are ordered by increasing height. (d) Atomic percents of Cu, Bi, and Se. (e) x for the ratio Cu_x:Bi_2 for the first three sections. (f) Photo of crystals cleaved from section 3 of the same ingot. The smallest division of the grid is 1 mm.

for all of our other magnetization vs. temperature data, as well as for data reported elsewhere [1, 92, 95, 97, 101]. Generally, measured T_C values varied within $2.5 \leq T \leq 3.6$, consistent with the T_C range reported for the electrochemical method[99], but unlike in ref. [99] there is no apparent correlation between T_C and nominal x value in our data. This lack of correlation may be due to the increased inhomogeneity expected for the MG method.

Magnetization data as a function of field are plotted in Fig. 5(c) for a 5.1 mg sample with $x = 0.35$ and ∼48% shielding fraction at 1.7 K. Both $H \perp c$ and $H \parallel c$ are plotted. The highest shielding fraction that we measured was 56% for another $x = 0.35$ sample with similar growth and annealing conditions. The demagnetization effect was neglected since it is expected to be small for field applied to a flat crystal within its plane. The dimensions for the 48% and 56% shielding fraction samples were roughly $1.7 \times 2.1 \times 0.25$ mm^3 and $1.4 \times 0.8 \times 0.2$ mm^3, respectively. These samples were brittle and their size was small due to attempting to isolate portions with the highest shielding fractions; typical dimensions for other samples were the same thickness or less, and longer. These shielding fractions are higher than any previously reported shielding fractions for the MG method [1, 79, 95–98] and comparable to those of the electrochemical method [92]. Our magnetization curves for $H \perp c$ and $H \parallel c$ are similar to magnetization curves previously reported[92, 95], with H_{c1} significantly larger for $H \perp c$ than for $H \parallel c$. We note that the minima of the magnetization curves for $H \perp c$ varied from roughly 4 Oe to 10 Oe for different crystals, even for the same nominal composition, growth, and annealing conditions, and there was no apparent correlation with shielding fraction.

To get insight into how the Cu was incorporated into Bi_2Se_3, we performed EDX measurements on samples from one of our $x = 0.25$ FZ ingots having good crystal quality, as shown in Figures 5(d) and 5(e). We note that there was a decrease of the measured Cu to Bi ratio with increasing electron accelerating voltage (and little change for the Se to Bi ratio), possibly indicating a strong depth dependence in Cu composition, so a high voltage of 25 keV was used to probe the bulk composition to a greater extent. The ingot was divided into four sections, ordered by height (see Fig. 5(d), right); sections 1 to 4 had lengths of 3, 2.5, 5.5, and 1 cm, respectively. In Fig. 5(d), atomic percentages for Cu, Bi, and Se are plotted for pieces selected from each section. Fig. 5(e) shows a portion of the same data, but in terms of the x in the ratio Cu_x:Bi_2. Unfortunately, EDX-measured x values varied widely for the same nominal x. Even MG $Cu_{0.05}Bi_2Se_3$ samples had similar EDX

x values (not plotted) as for nominal $x = 0.25$ or 0.3 samples. This variation is evident in Fig. 5(e). The reason for the inconsistent EDX results is uncertain, though it is possible that Cu tends to segregate in certain planes, making those planes easiest to cleave and thus most likely to be probed, or that Cu segregates to the surface soon after cleaving. Nevertheless, in Fig. 5(d) we see clear evidence of Cu-rich, non-Bi_2Se_3 related compositions in section 4, with a large increase in Cu fraction and a deviation from a Bi:Se ratio of 2:3. These data suggest that, for most of the ingot, $Cu_xBi_2Se_3$ of lower-than-nominal Cu concentration crystallized as the liquid zone passed through the starting materials, making the liquid zone increasingly Cu-rich until the Cu precipitated out at the top of the ingot.

In Fig. 5(f), we show a photo of a crystal cleaved from the inside of the FZ ingot whose EDX data is plotted in Fig. 5(d) and 5(e); we see that crystals many cm long can be cleaved from the inside of FZ ingots, unlike for the MG method where such large crystals are only found at the top surface (corresponding to the free surface of the melt). A copper coloring which usually appears on $Cu_xBi_2Se_3$ samples after some time has passed [1] is present. Usually, this coloring appeared slowly, on the order of weeks or months, but we have seen similar coloring already present on crystals taken from an ingot that was quenched from a liquid melt. Despite appearance changes, we have observed that crystals initially found to be superconducting remain superconducting for many months afterward, but there is variation between samples and some loss has been observed. For example, the sample initially measured to have 48% shielding fraction was measured to have 36% shielding fraction 19 months later, whereas two other samples, each with 7% to 8% shielding fractions, still had shielding fractions within this range 7 months later.

Shielding fractions for $Cu_{0.3}Bi_2Se_3$ crystals subjected to various growth and annealing conditions are plotted in Fig. 6(a). After growth (which included quenching), crystals were cleaved from the inside of the ingots and measured ("as-grown"), with remaining parts of the ingots being annealed and exposed to different cooling conditions: quenching in liquid nitrogen and cooling within a minute ("quench"); smash-quenching, where the ampoule is smashed open in liquid nitrogen and cooled within seconds ("smash-quench"); or furnace-cooling, in which the furnace is shut off and the ampoule is cooled within several hours ("furnace-cool"). Some of the samples that were furnace-cooled were later annealed and quenched ("furnace-cool then quench"). In addition, as-grown and annealed FZ samples ("floating-

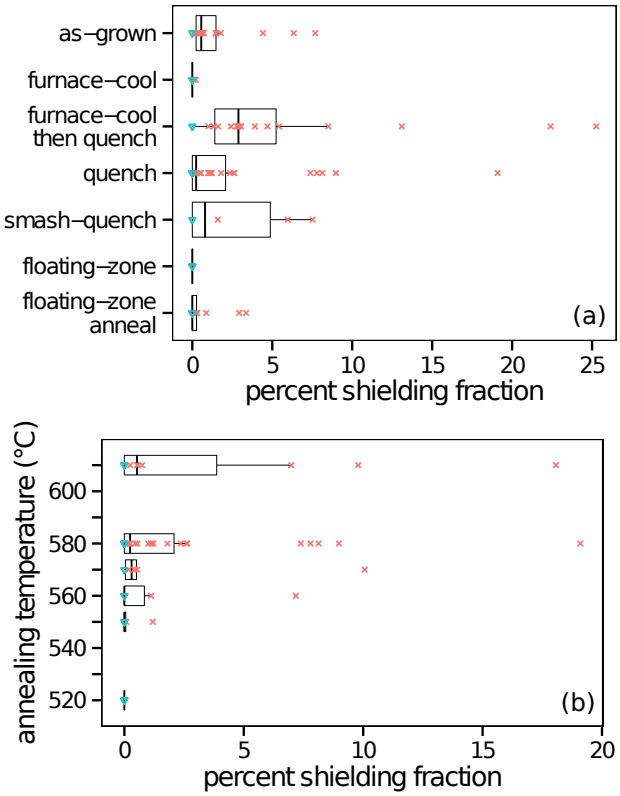

Figure 6: (a) Shielding fractions obtained for samples of $Cu_{0.3}Bi_2Se_3$ obtained for various growth and annealing conditions. See text for description of conditions. The numbers of samples plotted in each row from top to bottom are 19, 12, 18, 31, 6, 6, and 18. (b) Shielding fractions for MG $Cu_{0.3}Bi_2Se_3$ samples obtained after annealing and quenching at the displayed temperatures. The numbers of samples plotted in each row from top to bottom are 11, 31, 6, 6, 6, and 6. In (a) and (b), for each distribution of shielding fractions (including non-superconducting samples), the boxplot indicates the median, quartiles, and the most extreme values not greater than 1.5 times the interquartile range from the median; the triangles represent samples with negligible diamagnetic response.

zone" and "floating-zone anneal") were measured. Due to the large variation in shielding fractions even for the same conditions, we focus on cases where there is a qualitative difference between the shielding fraction distributions for different conditions.

A few findings are readily apparent in Fig. 6(a). First, annealing followed by furnace-cooling was clearly detrimental to superconductivity, with most of the samples measured having no diamagnetic response, whereas annealing followed by quenching had results comparable to the as-grown samples (which were also quenched), showing the importance of quenching for superconductivity in $Cu_xBi_2Se_3$. Pieces that were annealed and furnace-cooled and then annealed and quenched showed relatively large shielding fractions, suggesting that the detrimental effects of annealing and furnace-cooling appear to be reversible by subsequent annealing and quenching. We see no clear difference between the quenching and smash-quenching data, suggesting that cooling to room temperature within a minute is sufficiently fast to allow superconductivity.

The FZ method was much less effective than the MG method for making superconducting samples. None of the six as-grown FZ samples included in Fig. 6(a) were superconducting, and we have also found that magnetic responses at $H = 10$ Oe for crystals from other FZ ingots with $x = 0.25$ or 0.35 (not plotted) were also very low. By annealing and quenching, it is possible to induce superconductivity; however, the shielding fraction tends to be low compared to the MG samples. It should be noted that the samples measured tended to be good single crystals cleaved from the middle of the FZ ingot.

In Fig. 6(b) we show the dependence of shielding fraction on annealing temperature for MG $Cu_{0.3}Bi_2Se_3$ samples that were quenched after annealing. (All pieces were originally quenched from 580°C or higher after growth.) We see that large shielding fractions were achievable after quenching from an annealing temperature above 560°C, with lower temperatures appearing to result in little superconductivity relative to either the as-grown or quenched-above-560°C sample sets. The temperature-dependence agrees with data reported for the electrochemical method [99], with superconductivity found after annealing between 530°C and 620°C, whereas no superconductivity was found between 500°C to 520°C.

3.5 Discussion

There are a number of aspects of the crystal growth and superconductivity in $Cu_xBi_2Se_3$ which need explanation. Why does the superconductivity vary so wildly from sample to sample, with most samples having low shielding fraction but a few having >50% shielding fraction? Why is quenching necessary? Why do FZ-grown crystals have low shielding fractions?

We can address some of these questions by comparing the MG and FZ methods. The MG method should result in more inhomogeneity before quenching on a macroscopic scale than the FZ method. The large Cu concentration near the top of the FZ ingot in Fig. 5(d) and the relatively low Cu concentrations obtained elsewhere suggest that for slow cooling the solubility of Cu in $Cu_xBi_2Se_3$ is low. Combined with the decreasing melting point of $Cu_xBi_2Se_3$ with increasing Cu concentration [99, 102], it seems that cooling slowly from the liquid phase should result in inhomogeneity, with lower-Cu $Cu_xBi_2Se_3$ crystals solidifying before higher-Cu compositions, as suggested by others[98]. In the FZ method, the Cu-rich regions would be deposited toward the end of the ingot under ideal crystal growth conditions, but in the MG method these regions would be deposited in the interior of the ingot, increasing the inhomogeneity. If impurity phases were responsible for the superconductivity in $Cu_xBi_2Se_3$, this would provide a natural explanation for the relative lack of superconductivity in FZ-grown crystals, though another possibility is that the Cu concentration in the FZ-grown crystals is too low.

For more insight into the source of the inhomogeneity and the superconductivity in $Cu_xBi_2Se_3$, we consider two cases: primary-phase, where the superconductivity arises from regions having the same phase as Bi_2Se_3; or secondary-phase, where the superconductivity arises from an impurity phase. In both of these cases, quenching above 560°C is presumed to preserve the configuration at high temperatures, while annealing and quenching within 550°C to 520°C (and probably lower) is presumed to equilibrate the system to the lower-temperature configuration.

For the primary-phase case, the superconductivity should arise from sufficiently highly-intercalated Bi_2Se_3 regions, since our lower-than-nominal Cu-intercalated Bi_2Se_3 FZ crystals were non-superconducting. (It should be noted, though, that a $Cu_xBi_2Se_3$ thin film with $x = 0.12$ was found non-superconducting[103] even with a carrier concentration higher than reported for bulk superconducting samples [1].) To account for the necessity of quenching, we presume that highly-intercalated Bi_2Se_3 may be stable at high tem-

peratures but may decompose to less-intercalated Bi_2Se_3 and Cu-rich impurity phases upon slow cooling, a decomposition which should be reversible with further annealing and quenching. While this scenario is consistent with some observations, we feel it does not provide a natural explanation for the inhomogeneity; assuming that the copper is intercalated homogeneously above 560°C, one should only expect inhomogeneity after quenching in this scenario if only a small portion of the sample cooled quickly enough.

For the secondary-phase case, the role of quenching would be to preserve a phase separation rather than a single phase. Specifically, at high temperatures we assume a phase separation between a less Cu-intercalated Bi_2Se_3 phase and a Cu-rich impurity phase, with the impurity phase being only metastable at lower temperatures. The Cu-rich phase would be the most obviously responsible for the superconductivity considering the low shielding fractions and the majority Bi_2Se_3 phase present in most samples.

This situation is similar to that of $K_xFe_{2-y}Se_2$, another layered superconducting system that must be quenched from high temperature in order to obtain superconductivity [104]. While the dominant phase, with ordered Fe vacancies, exhibits antiferromagnetic order with large magnetic moments [105], it is now clear that the superconductivity in $K_xFe_{2-y}Se_2$ is driven by a second, epitaxial phase that may be vacancy free [106–109]. The second phase can only be obtained by quenching; slow cooling yields only the vacancy-ordered antiferromagnet [110]. T_C values remain nearly constant around 30 K with varying composition [111], suggesting that the secondary phase maintains a similar composition despite changes in nominal composition. Though T_C varies to a greater extent in $Cu_xBi_2Se_3$, it also appears to be bounded, with the lowest reported T_C being 2.2 K and shielding fractions being maximized for intermediate T_C in electrochemically-doped samples [99]. Given the limited shielding fraction in $Cu_xBi_2Se_3$ and the similarities to $K_xFe_{2-y}Se_2$ discussed above, as well as the lack of superconductivity in the FZ-grown crystals, which are expected to have higher crystal quality than MG-grown crystals, the possibility that the superconductivity might be due to a yet-to-be-identified second phase deserves consideration.

3.6 Summary

In summary, we have investigated various growth and annealing conditions on $Cu_xBi_2Se_3$ and identified their effects on shielding fractions. Shielding fractions as high as 56% have been measured, showing that a substantial

shielding fraction is possible for the MG method, though typical values are much lower. Quenching after annealing at a sufficiently high temperature was shown to be crucial to obtaining superconductivity, as equilibrated samples from furnace-cooling are generally non-superconducting. One can recover superconductivity in such samples by subsequent annealing and quenching. FZ-grown crystals had negligible superconductivity. The anneal and quench treatment can yield significant shielding fractions in MG samples, but for the large FZ-grown crystals, the fraction is always small. EDX measurements on the FZ ingots indicate that the Cu concentration is substantially lower than the nominal value in the feed rod throughout most of the growth process.

The fact that quenching is essential indicates that the superconducting phase is metastable. In combination with the observation that shielding fractions are usually very small, we suggest that the superconductivity might be driven by a secondary phase that makes up a small volume fraction of the sample.

4 Anomalous phonon mode in $\mathbf{Fe_{1+y-z}Ni_zTe_{1-x}Se_x}$

In this Section, I present research characterizing anomalous phonon mode behavior in samples of the $Fe_{1+y}Te_{1-x}Se_x$ iron-based superconductor family, including nickel-doped compositions. This research is unpublished. I have had assistance in this research from Zhijun Xu, who was at U. C. Berkeley, Igor Zaliznyak, Guangyong Xu, Genda Gu, and John Tranquada of Brookhaven National Laboratory, David Fobes of Los Alamos National Laboratory, Barry Winn of Oak Ridge National Laboratory, and Jose Rodriguez-Rivera and Peter Gehring of the National Institute of Standards and Technology.

4.1 Abstract

We present neutron scattering studies on samples of five $Fe_{1+y-z}Ni_zTe_{1-x}Se_x$ compositions, focusing on a recently studied anomalous phonon branch. Though the dispersion of this branch appears to identify it as the c-axis polarized transverse acoustic mode branch, the branch can be clearly seen in the $HK0$ plane, where the neutron scattering intensity of c-axis polarized phonon modes should be zero. Also, this branch is clearly visible in Brillouin zones corresponding to forbidden Bragg peaks, even where the in-plane-polarized acoustic phonon modes are too weak to be detectable. We suggest that disorder may cause a depolarization of the c-axis polarized transverse acoustic modes, resulting in the anomalous visibility of this mode. No clearly anomalous behavior is seen in the temperature dependence of the dispersion or intensity of this mode. There may be a correlation between the ability to host superconductivity and the intensity of the anomalous phonon mode, as found from comparing anomalous mode intensities between superconducting and non-superconducting samples measured on the same instruments.

4.2 Introduction

The iron-based superconductors (FeBS) continue to be the source of debate as to the role of magnetic and orbital correlations in their superconducting and magnetic properties. Though neutron scattering experiments on these materials have focused mainly on the magnetic excitations in these compounds, there are other properties that are not well understood, such as the

recently reported anomalous phonon mode [10].

Generally, the FeBS phase diagrams have a magnetically ordered parent compound having long-range antiferromagnetic (AFM) order that sets in at a temperature T_N, with a structural phase transition at the same or slightly higher temperature T_S. For most FeBS, magnetic order is suppressed and superconductivity appears with sufficient electron- or hole-doping, though in the $Fe_{1+y}Te_{1-x}Se_x$ system these changes happen with isovalent substitution [112] (see Fig. 7). In $Fe_{1+y}Te_{1-x}Se_x$, superconductivity can be suppressed if the interstitial Fe content y is too high, or if another transition metal such as Ni is substituted for Fe [9]. Figure 8 shows the crystal structure of $FeTe_{1-x}Se_x$. At high temperatures, the crystal is tetragonal throughout the phase diagram with symmetry $P4/nmm$ [113]. Nickel substitution up to 10% does not appear to change this symmetry [114]. Below T_S, orthorhombic and monoclinic phases have been found in $Fe_{1+y}Te$, depending on y [115], and in $Fe_{1+y}Te_{1-x}Se_x$ for compositions not too far from FeSe there is a lower-temperature orthorhombic phase [113, 116].

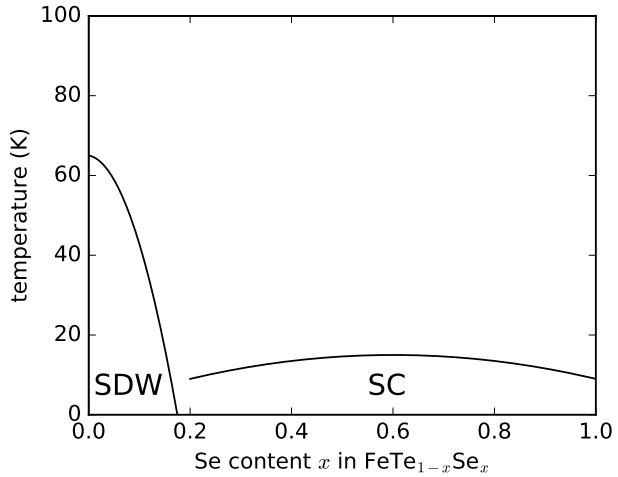

Figure 7: Schematic illustration of the phase diagram for $FeTe_{1-x}Se_x$, based on Ref. [112]. "SC" labels the superconducting region of the phase diagram, and "SDW" labels the region with spin-density wave antiferromagnetic order; the upper boundaries of these regions are the transition temperatures for superconductivity and antiferromagnetic order, respectively.

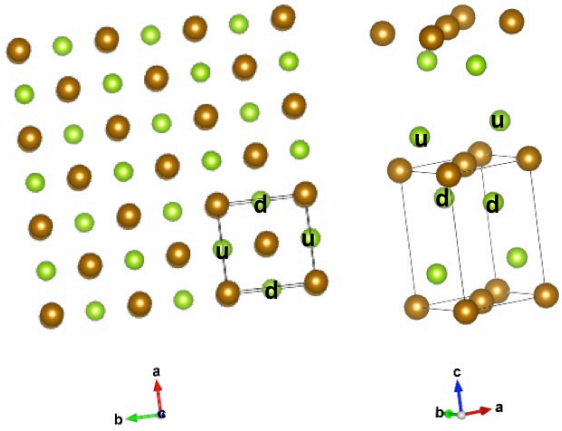

Figure 8: Crystal structure for $FeTe_{1-x}Se_x$ as seen from along the c-axis (left) and from the side (right). Yellow spheres are Fe, green spheres are anions (Te or Se). "u" and "d" label anions that are above and below the plane of Fe ions, respectively. Images generated by the software VESTA [117].

Binding forces are an important part of structural properties, and they can be probed by measuring the properties of the acoustic phonons or the elastic constants. Most of the studies of the acoustic phonons or elastic properties of FeBS have focused on anomalies around the structural phase transition [118–124]. Unusual behavior, however, was recently observed in the form of an anomalous phonon mode branch emanating from the (100) forbidden Bragg peak, as seen by neutron scattering [10]. (100), (210), and many other peaks at $L = 0$ reciprocal lattice wavevectors are forbidden due to the neutron scattering amplitudes from the two Se/Te anions canceling each other out[14]. ((H, K, L) denote coordinates in reciprocal space. See Fig. 9 for some of the forbidden peak positions.) Although acoustic phonons from symmetry-forbidden Bragg peak wavevectors are not themselves forbidden, the phonon's dynamic structure factor should approach zero as the phonon wavevector $\mathbf{q} \to \mathbf{0}$, where $\mathbf{q}$ is defined relative to the Brillouin zone (BZ) center wavevector $\mathbf{G}$ [37]. However, the measured $\hbar\omega$-dependence of the intensity of this mode was reported to be inconsistent with this requirement [10].

To further study this anomalous phonon mode, we have conducted inelastic neutron scattering experiments on a number of $Fe_{1+y}Te_{1-x}Se_x$ and $Fe_{1+y-z}Ni_zTe_{1-x}Se_x$ single crystals, studying the phonon modes in the $HK0$ and $H0L$ planes. We identify the anomalous phonon mode, which is most clearly seen emanating out from the (100) and (210) forbidden Bragg peaks, as the c-axis polarized transverse acoustic (TA′) phonon based on a comparison of its dispersion along $(H00)$ with the dispersion of the TA′ branch as seen along $(H0L)$. However, the neutron scattering intensity of such a mode in the $HK0$ plane is expected to be zero. The TA′ mode is clearly visible in the $HK0$ plane near forbidden Bragg peak wavevectors, which is unusual since the longitudinal acoustic (LA) and the ab-plane polarized transverse acoustic (TA) modes are sufficiently weak to be undetectable near these wavevectors. Two modes appear to be present along $(00L)$, even though only the presumptive c-axis polarized longitudinal acoustic mode should have non-zero

[14]For $L = 0$, the scattering amplitudes from each anion should not depend on the c-axis position. If we look at the crystal structure along the c-axis, as shown in Fig. 8 on the left, there are two anions per unit cell, one above the plane of Fe ions, and another below the plane; these are labeled "u" and "d". With $L = 0$, the effective symmetry is the checkerboard symmetry we see when we are allowed to ignore the difference between the "u" and "d" anions. As a result, peaks with $L = 0$ and odd $H + K$ are forbidden, as shown in Fig. 9.

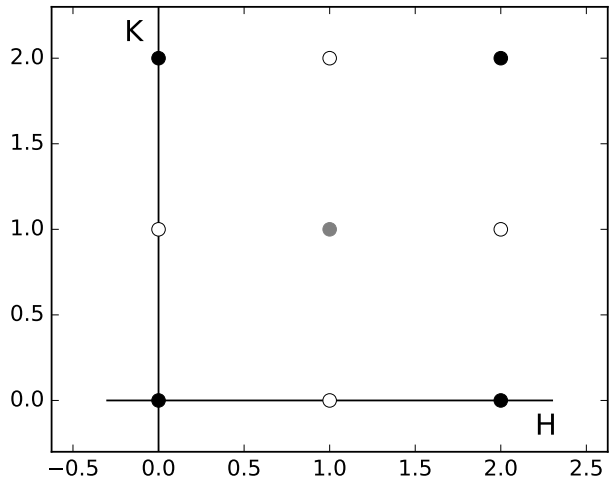

Figure 9: Schematic diagram for the expected elastic scattering peaks in the $HK0$ plane. Empty circles (e.g., at (100)) denote Bragg peaks forbidden by symmetry.

intensity along this line. We propose that disorder, perhaps related to variation in anion height for different anions, may explain the anomalous visibility of these modes. In addition, we provide evidence that superconducting samples may have more intense anomalous mode intensities in the $HK0$ plane than non-superconducting samples. There is no clear temperature dependence except for a slight softening from 4 to 300 K, and the temperature dependence of the anomalous mode intensity along ($H00$) roughly follows the Bose factor, as expected.

4.3 Experimental Details

Measurements were taken on $Fe_{1+y}Te_{1-x}Se_x$ and $Fe_{1+y-z}Ni_zTe_{1-x}Se_x$ single crystals grown by unidirectional solidification[9]. Samples of five compositions were measured: two superconducting samples (SC45 and SC65), and three non-superconducting samples (NSC45Ni10, NSC70, and FeTe); see Table 1 for detailed information. The non-superconductivity of NSC45Ni10 is presumed to be due to Ni-doping, which suppresses superconductivity [114], and the non-superconductivity of NSC70 is presumed to be due to excess

Table 1: Sample names, nominal compositions, T_C if superconducting, masses, lattice constants a and c used in defining reciprocal lattice parameters for data analysis, instruments used in neutron scattering measurements, and scattering plane.

name	nominal composition	T_C	mass	a (Å)	c (Å)	instrument	scattering plane
SC45	$FeTe_{0.55}Se_{0.45}$	15 K	23.4 g	3.79	6.03	MACS	$HK0$
						HYSPEC	$H0L$
NSC45Ni10	$Ni_{0.1}Fe_{0.9}Te_{0.55}Se_{0.45}$	none	12.3 g	3.79	6.03	MACS	$HK0$
						HYSPEC	$H0L$
						BT7	$H0L$
SC65	$Fe_{0.98}Te_{0.35}Se_{0.65}$	14 K	22 g	3.80	6.10	HYSPEC	$HK0$
NSC70	$Fe_{1.08}Te_{0.3}Se_{0.7}$	none	18.1 g	3.80	6.10	HYSPEC	$HK0$
FeTe	$Fe_{1.12}Te$	none	22 g	3.82	6.28	HYSPEC	$HK0$
						HYSPEC	$H0L$

iron, which is known to suppress superconductivity in samples with Se fractions within the superconducting region of the $FeTe_{1-x}Se_x$ phase diagram [125].

Inelastic neutron scattering experiments were performed on the HYSPEC time-of-flight spectrometer at the Spallation Neutron Source at Oak Ridge National Laboratory [126], the BT7 triple-axis spectrometer at the NIST Center for Neutron Research (NCNR) at the National Institute of Standards and Technology (NIST) [127], and the MACS triple-axis spectrometer equipped with a multi-analyzer at the NCNR [128]. For the MACS measurements on SC40 and NSC45Ni10, data were taken in the $HK0$ scattering plane, with E_f fixed to 5 meV; data sets corresponding to different energy transfers $\hbar\omega$ were obtained. For the BT7 measurements on NSC45Ni10, data were taken in the $H0L$ plane, with E_f fixed to 14.7 meV, collimations set to open-80′-s-80′-120′, and two pyrolitic graphite filters placed after the sample to remove signals from higher-order neutrons. For the HYSPEC measurements on SC65 and NSC70, data were taken in the $HK0$ scattering plane with an incident energy of $E_i = 20$ meV and a Fermi chopper frequency of 180 Hz. For $Fe_{1.12}Te$, measurements at HYSPEC were taken in both the $HK0$ and $H0L$ planes, with incident energies set to $E_i = 24$ and 15 meV and Fermi chopper frequencies set to 240 and 300 Hz, respectively. For the $Fe_{1.12}Te$ $H0L$ data, before further processing, averaging was performed within a sample rotation angle range of 3°, and a background obtained from an empty can scan at 300 K was subtracted. The HYSPEC measurements on SC40

and NSC45Ni10 were performed in the $H0L$ scattering plane, with $E_i = 20$ meV and a Fermi chopper frequency of 180 Hz. At MACS, measurements were also taken in the $HK0$ plane, with E_f fixed to 5 meV.

Unless otherwise noted, neutron scattering data taken in the $HK0$ plane were mapped into the $H \geq 0$, $K \geq 0$ quadrant by rotations by multiples of 90°, and data taken in the $H0L$ plane were mapped by reflection ("folded") into the $H \geq 0$, $L \geq 0$ quadrant. Some of the $HK0$ data were additionally folded about $H = K$ into the $H \geq K$ region as indicated in the text. These mappings were done prior to obtaining slices of the data or performing curve-fitting. In all intensity maps, the data were smoothed. All intensities are in arbitrary units, but are consistent for all data presented for the same sample measured on the same instrument in the same scattering plane. A tetragonal unit cell was used for data analysis, with lattice constants as listed in Table 1. All wavevectors are reported in reciprocal lattice units. Error bars represent statistical error and correspond to 1 standard deviation from the observed value unless otherwise noted.

4.4 Data and Analysis

4.4.1 Phonon dispersions

We start by showing the acoustic phonon branches in the $HK0$ plane in Figure 10. Fig. 10(a) shows a neutron scattering intensity map of the acoustic phonon modes at $\hbar\omega = 7.5$ meV for SC45 at 300 K. Three acoustic phonon branches can be seen, but only two are expected to be seen in the $HK0$ plane due to the expected mode polarization-dependence of the neutron scattering intensity. The dynamic structure factor (contained in the formula for single-phonon neutron scattering intensity) is as follows [37]:

$$\mathscr{F}(\mathbf{Q}) = \sum_j \frac{\bar{b}_j}{\sqrt{m_j}} (\mathbf{Q} \cdot \xi_{\mathbf{q},js}) e^{i\mathbf{Q}\cdot\mathbf{d}_j} e^{-W_j}. \tag{17}$$

Here, j labels the jth atom in the unit cell, m_j is the atom's mass, $\bar{b}_j$ is the nucleus's average neutron scattering length, d_j is the site of the jth nucleus, e^{-W_j} is the Debye-Waller factor, and $\xi_{\mathbf{q},js}$ is the phonon polarization vector of the jth nucleus and the sth phonon branch at wavevector $\mathbf{q}$ away from the nearest reciprocal lattice wavevector. Given the symmetry of the crystal structures of our samples for all the temperatures measured, the polarization vectors of modes at high-symmetry $\mathbf{q}$ should lie along high-symmetry

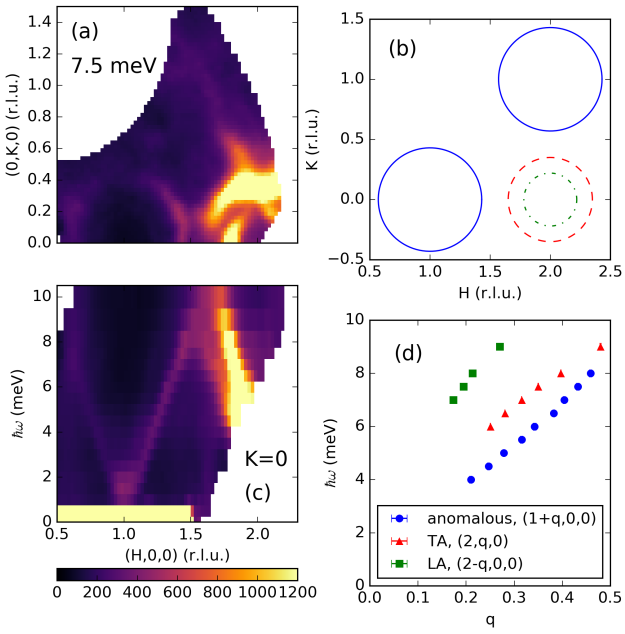

Figure 10: (a) Neutron scattering intensity maps showing the acoustic phonons for sample SC45 measured on MACS at $T = 300$ K in the $HK0$ plane. The data in (a) were taken at $\hbar\omega = 7.5$ meV. (b) Schematic diagram of the locations in the $HK0$ plane of the phonon branches of the anomalous (TA′) mode (blue solid line), the transverse acoustic (TA) mode (red dashed line), and the longitudinal acoustic (LA) mode (green dot-dashed line). (c) Neutron scattering intensity map for SC45 at $T = 300$ K as a function of energy transfer $\hbar\omega$ and momentum transfer along $(H00)$. The data in (c) were taken at $K = 0$ and averaged within $0 \leq K \leq 0.05$. Data displayed in (a) and (c) were folded across $H = 0$, $K = 0$, and $H = K$. (d) Dispersions of phonon branches for the $T = 300$ K SC45 data, with momentum transfer in terms of q obtained by constant-$\hbar\omega$ fits along $(H00)$ and $(2K0)$, as explained in the text. Data were averaged within $\Delta K = \pm 0.05$ for fits along $(H00)$ and $\Delta H = \pm 0.05$ for fits along $(2K0)$.

directions. For example, for wavevectors on the $(H00)$ line, there should be one mode polarized in the longitudinal direction, one mode polarized transversely in the ab-plane, and one mode polarized tranversely in the c-direction. The $\mathbf{Q} \cdot \xi$ factor is only nonzero for the longitudinal modes, so the phonon branch closest to (200) is determined to be the LA mode, and by similar reasoning the other branch near (200) is determined to be the TA branch polarized in the ab-plane since TA$'$ phonons, polarized transversely in the c-direction, should ideally have zero intensity within the $HK0$ plane. As we will show below, however, the third phonon branch, dispersing prominently out of (100) and (210), can be identified as the TA$'$ branch by matching its dispersion along $(H00)$ to that along $(H01)$, where the TA$'$ intensity should be nonzero. Nevertheless, the TA$'$ branch is clearly seen in the $HK0$ plane for all of the samples in the $Fe_{1+y-z}Ni_zTe_{1-x}Se_x$ family that we measured (i.e., those in Table 1) at all of the temperatures we measured (from 4 to 300 K).

The LA and TA modes appear to be so weak near the forbidden Bragg peaks (100) and (210) that they cannot be seen. This weak intensity can be explained by the requirement that the dynamic structure factor must approach zero as the static structure factor approaches zero (as it does for forbidden Bragg peaks):

$$\lim_{\mathbf{q}\to\mathbf{0}} |\mathscr{F}(\mathbf{Q})|^2 = \frac{|\mathbf{G}|^2}{M} |F_N(\mathbf{G})|^2 \tag{18}$$

where $\mathbf{G}$ is the Bragg peak wavevector, $\mathbf{q} = \mathbf{Q} - \mathbf{G}$, $M = \sum_j m_j$, and $F_N(\mathbf{G})$ is the static structure factor which is zero for forbidden peaks. However, the visibility of the TA$'$ branch near the forbidden peaks is unexpected.

Figure 10(b) shows a schematic diagram of the three acoustic phonon branches in the $HK0$ plane. Figure 10(c) shows an intensity map from the same data set as for Fig. 10(a), but with intensity plotted against $\hbar\omega$ and momentum along $(H00)$. The TA$'$ mode dispersing from (100) and the LA mode dispersing from the direction of (200) can clearly be seen. In addition, intensity is present underneath the LA mode, possibly indicating the presence of the anomalous mode near (200). By fitting to these data, the dispersions of the three branches along $(H00)$ and symmetry-equivalent wavevectors can be compared, as shown in Fig. 10(d). All three dispersions are distinct.

In Figure 11 we show dispersions along different directions, with plots of intensity against $\hbar\omega$ and momentum along with quantitative comparisons of the dispersions. Figures 11(a) and (c) show the TA$'$ branch along $(1.9, K, 0)$

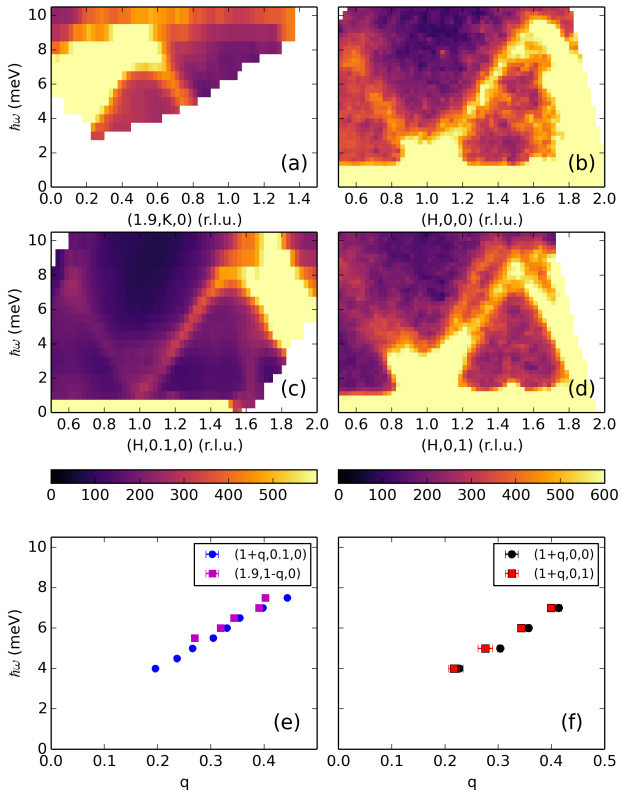

Figure 11: (a,c,e) Data showing a similar dispersion for the anomalous modes near (100) and (210). (b,d,f) Data showing a similar dispersion for the anomalous mode along (H00) and the c-axis polarized TA′ mode measured along (H01). All of these data were taken on SC45 at 300 K. (a) and (c) show data taken on MACS in the $HK0$ plane. In (a), data were averaged within $1.85 \leq H \leq 1.95$ and plotted along energy transfer $\hbar\omega$ and momentum transfer $(1.9, K, 0)$. In (c), the dispersions of the anomalous mode near (100) and (210) are plotted, as obtained from fits to constant-$\hbar\omega$ scans along $(H, 0.1, 0)$ and $(1.9, K, 0)$. (b) and (d) show data taken on HYSPEC in the $H0L$ plane. Data were averaged within $\Delta H = \pm 0.1$ and plotted along $\hbar\omega$ and either (H00) for (b) or (H01) for (d). In (f), the dispersions of the anomalous mode along (H00) and the c-polarized transverse acoustic mode along (H01) (the lower-energy mode dispersing from (101)) are plotted, as obtained from fits to constant-$\hbar\omega$ scans along (H00) and (H01).

and $(H, 0.1, 0)$, and the fitted values in Fig. 11(e) confirm that the branches near (100) and (210) have the same dispersions along symmetry-equivalent directions. (We compare $(1.9, K, 0)$ and $(H, 0.1, 0)$ rather than $(2K0)$ and $(H00)$ due to limited detector coverage along those lines.) Figures 11(b) and (d) show the branches along $(H00)$ and $(H01)$. Along $(H00)$, the TA$'$ branch is seen dispersing from (100) and the LA branch is seen dispersing from (200). Along $(H01)$, where we expect the TA$'$ branch to be visible along with the LA branch, both branches indeed disperse from (101) and (201). A comparison of the TA$'$ branches along $(H00)$ and $(H01)$ from fitting is shown in Fig. 11(f), confirming that the anomalous mode dispersing out of (100) is indeed the c-axis-polarized TA$'$ mode.

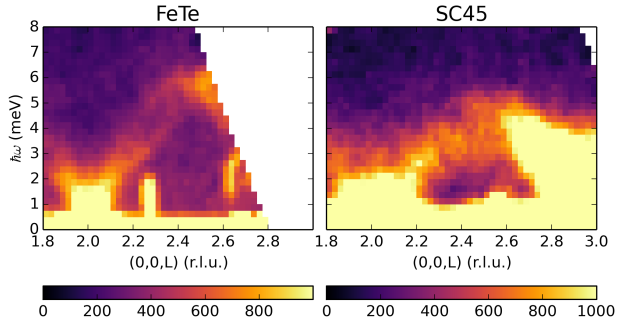

Figure 12: Neutron scattering intensity maps along energy transfer and $(00L)$ for FeTe and SC45 at 300 K from data taken in the $H0L$ plane. Data were averaged within $0 \leq H \leq 0.1$. The data taken for FeTe had higher resolution due to the lower E_i used (15 meV for FeTe, 20 meV for SC45).

Since the TA$'$ mode is anomalously visible along $(H00)$, one might suspect an anomalous visibility of a mode along $(00L)$, which, like $(H00)$, should only have nonzero intensity from longitudinal acoustic phonons due to the $\mathbf{Q} \cdot \xi$ factor. Fig. 12 shows intensity maps of modes along $(00L)$ for FeTe and SC45. We can see two modes dimly visible for FeTe (whose data was taken at lower incident energy E_i and thus better energy resolution). For SC45, the data are not clear enough to confirm the presence of two modes. Separate measurements of intensity vs. $\hbar\omega$ at certain wavevectors along this line are shown in Fig. 13 for NSC45Ni10. When we compare the data for different Brillouin zones, i.e, $(0, 0, 2.3)$ vs. $(0, 0, 4.3)$ and $(0, 0, 2.5)$ vs. $(0, 0, 4.5)$, we see a couple of behaviors that suggest that two modes are present, though the resolution

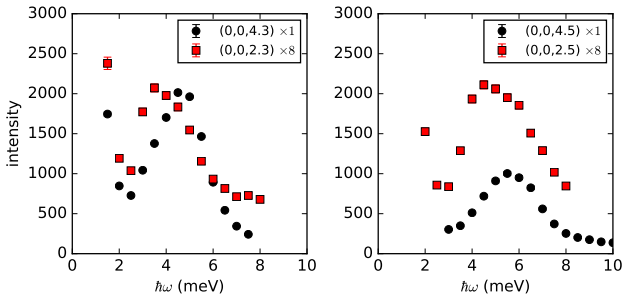

Figure 13: Phonon modes seen along $(00L)$ near (002) and (004) in NSC45Ni10 at 300 K as measured in constant-$\mathbf{Q}$ scans on BT7. The wavevectors are listed in the legends. Intensities at $(0, 0, 2.3)$ and $(0, 0, 2.5)$ were multiplied by 8 for ease of comparison.

is too broad to distinguish them clearly. First, the energy of the maximum of the phonon lineshape changes between BZs, shifting toward higher energy near (004) as compared to (002), and second, the wavevector-dependence of the intensity varies differently, with a marked drop in peak intensity for $(0, 0, 4.5)$ as compared to $(0, 0, 4.3)$, but little change for $(0, 0, 2.5)$ as compared to $(0, 0, 2.3)$. The simplest explanation is that two phonon modes are present, and their intensities vary in different manners as we move from the (002) BZ to (004), possibly presenting another case of a branch being visible even when it is expected to have zero intensity according to the $\mathbf{Q} \cdot \xi$ factor in Eq. 17.

More views of the acoustic phonon branches can be seen in Figure 14 for FeTe and NSC70, which shows neutron scattering intensity maps from data taken in the $HK0$ plane. Figures 14(a) and (b) confirm the anomalous visibility of the TA′ branch along $(H00)$ in these compositions. Data taken along $(H20)$ can be seen in Figure 14(c) and (d), showing the *ab*-polarized TA mode dispersing from (020). (A hint of the TA′ dispersing from (120) can also be seen for NSC70.) Surprisingly, in both samples the TA mode appears to transition from dispersing toward greater $|\hbar\omega|$ to flattening around $|\hbar\omega| \approx 10$ meV, rather than bending back toward (120) (or simply having intensity drop to undetectable values near (120)) as might be expected given that the phonon dispersion curves should have the periodicity of the reciprocal lattice. This behavior may be explainable by the symmetry of the crystal. The unit

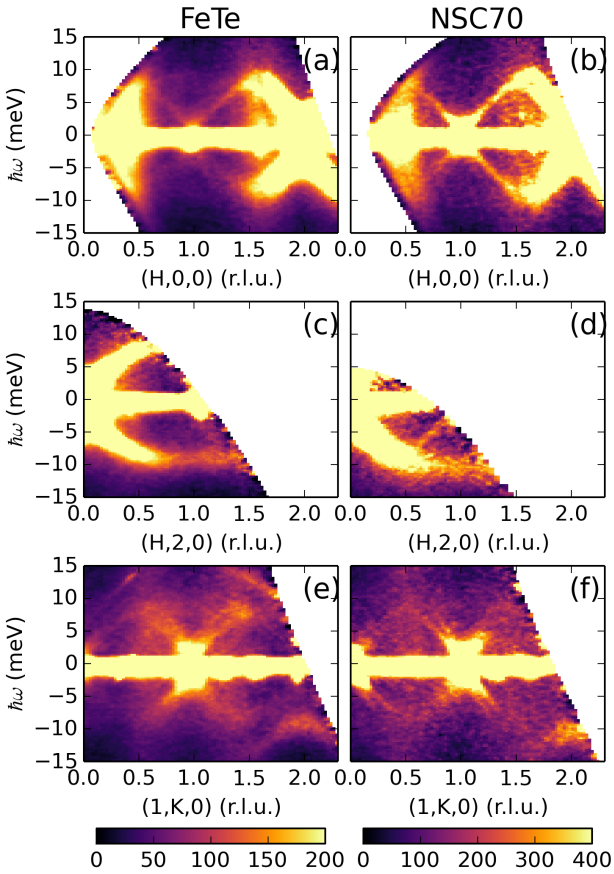

Figure 14: Phonon dispersion curves as seen from neutron scattering intensity maps of FeTe (a,c,e) and NSC70 (b,d,f) at 300 K along energy transfer $\hbar\omega$ and momentum transfer along (a,b) ($H00$), (c,d) ($H20$), and (e,f) ($1K0$). Data were taken in the $HK0$ plane. The data were averaged within, respectively, $0 \leq K \leq 0.1$, $0 \leq K \leq 0.1$, and $0.9 \leq H \leq 1.1$ for (a,b), (c,d), and (e,f). The incident energies were $E_i = 24$ meV for FeTe and $E_i = 20$ meV for NSC70. In addition to mapping the data into the $H \geq 0, K \geq 0$ quadrant via 90 degree rotations, the data in (a) and (b) were additionally folded across $H = K$.

cell of the system (Fig. 8) has Se/Te anions at $(0, 0.5)$ and $(0.5, 0)$ and Fe ions at $(0, 0)$ and $(0.5, 0.5)$ in the ab plane, with both Fe ions at $z = 0$ and each of the anions above and below the Fe-plane at a certain z value. Though the anions are positioned on opposite sides of the Fe-plane, the restoring forces on these ions for displacements within the xy plane should be the same due to the symmetry of the lattice, and thus one would expect phonons polarized in the ab plane to have a dispersion corresponding to a hypothetical 1-Fe unit cell resulting from both anions being functionally identical. Also, since $L = 0$, the neutron scattering contributions from the two anions should not depend on anion height. We may expect the dispersion to thus extend from (100) to (120), corresponding to an effectively 1-Fe unit cell symmetry for a 2-Fe unit cell notation. We note, though, that this argument should hold for the LA mode polarized in the ab plane as well, but we do not observe any sign of spectral weight connecting the (200) and (000) LA modes. As for the TA$'$ branch, for wavevectors in the $HK0$ plane these vibrations are along the c-axis, so that the effective symmetry due to the positions of the anions in the ab-plane is broken. Thus, for the TA$'$ branch, the bending toward (210) seen in Fig. 11(d) would be consistent with this explanation. Figure 14(e) and (f) show the acoustic phonons near (110) and another view of the flat part of the TA mode seen in Figures 14(c) and (d). The TA mode can be seen near -10 meV at $K = 2$ and appears to disperse toward greater $|\hbar\omega|$ in either K-direction.

We look at the temperature dependence of the TA$'$ dispersion along $(H00)$ in Figure 15 for SC45 and NSC45Ni10. Fits were done to constant-energy data subsets to map out the dispersions. We find little change in the dispersions except for a slight decrease in the steepness of the dispersion with heating.

4.4.2 Phonon intensities - temperature and composition dependence

To check the anomalous TA$'$ mode intensity for possible deviations from the expected temperature dependence of phonons, in Fig. 16 we plot integrated intensities obtained from fits for the TA$'$ mode along $(H00)$. The intensity is divided by $1/(1 - e^{-\hbar\omega/k_B T})$ to account for the expected Bose factor temperature dependence of phonons. Roughly speaking, the anomalous TA$'$ mode intensity does seem to follow the expected Bose factor dependence, though we note that there may be an additional intensity drop for wavevec-

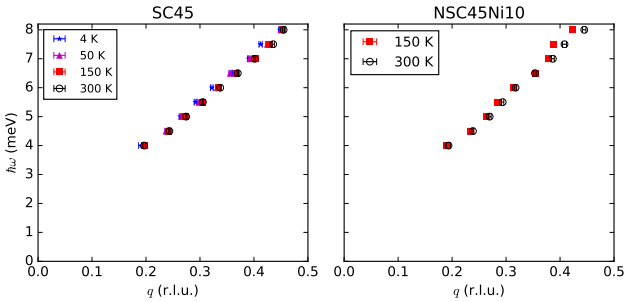

Figure 15: TA′ mode dispersion along $(H00)$ for data taken for SC45 and NSC45Ni10 at various temperatures on MACS. For each $\hbar\omega$ data set, a data subset averaged within $0 \leq K \leq 0.1$ and extending along $(H00)$ was obtained, then fitted to find the position $(1+q, 0, 0)$ of the anomalous phonon peak, with q plotted on the horizontal axis.

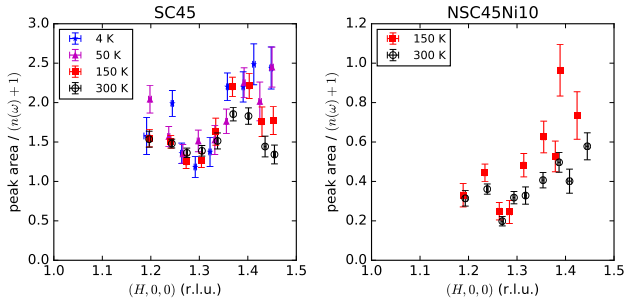

Figure 16: Integrated intensities from fits to TA′ phonon peaks along $(H00)$ for SC45 and NSC45Ni10 at various temperatures. Data were taken on MACS in the $HK0$ plane and integrated within $0 \leq K \leq 0.1$ before fitting. The integrated intensities were divided by $n(\omega)+1 = 1/(1-e^{-\hbar\omega/k_BT})$ to account for the typical Bose factor phonon temperature dependence. The $(H00)$ wavevectors plotted on the horizontal axis were found from fitting.

tors approaching the zone boundary ($H = 1.5$) which we cannot confirm or rule out due to the limited statistical quality of the data.

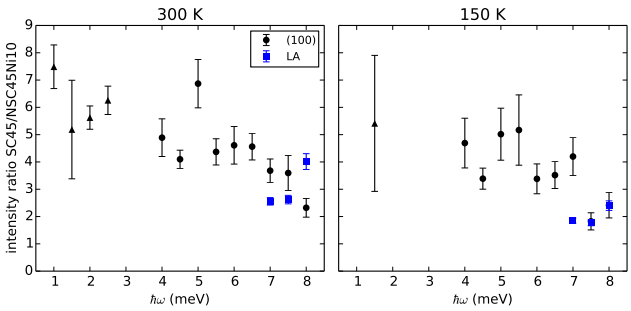

Figure 17: Ratios of the integrated intensities of TA′ mode phonon peaks along $(H00)$ of SC45 divided by those of NSC45Ni10, from data measured on MACS at 150 and 300 K in the $HK0$ plane. Intensities were found by fitting to the TA′ mode phonon peak in each constant-energy cut, averaging within $0 \leq K \leq 0.1$. Points marked with a black circle were found from fits to single phonon peaks at $(1 + q, 0, 0)$; points marked with a black triangle were found from fits to two phonon peaks at $(1 + q_1, 0, 0)$ and $(1 - q_2, 0, 0)$. Blue square markers represent fits to the LA mode along $(H00)$. The errors of the intensity ratios were found by propagating the errors of the individual intensity values found from the fits for each energy.

To check for variation with composition of the TA′ mode intensity along $(H00)$, Fig. 17 shows the ratios of the fitted TA′ intensities between SC45 and NSC45Ni10. For comparison, intensity ratios of similarly fitted LA mode peaks are also plotted. These results suggest that the anomalous TA′ mode intensity is more intense in SC45 than in NSC45Ni10, especially at low energies, after comparing with the intensity ratios of the LA mode in both samples.

For the data measured on HYSPEC, a cruder method of comparing phonon spectral weight was used. This method can be summarized as integrating the spectral weight in a broad region near (100), and comparing changes with respect to composition with a similar value obtained near (200) used for normalization. The integrated intensity near (100) should be almost entirely that of the anomalous TA′ mode intensity, judging from the undetectably small intensity of the other two modes near (100). The phonons

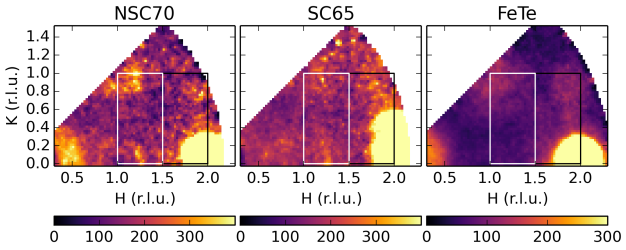

Figure 18: Neutron scattering intensity maps of NSC70, SC65, and FeTe in the $HK0$ plane at $\hbar\omega = -5$ meV. Data were taken on HYSPEC at 300 K. Data were mapped into the $H \geq K$ region by reflection across $H = K$ and averaged within $-5.25 \leq \hbar\omega \leq -4.75$ meV. The black rectangles represent the ranges of the cuts used in Fig. 19. The white rectangles represent the ranges of the cuts used in Fig. 20.

near (200) were used for normalization since the conventional LA and TA phonons have a large intensity near (200), but we should remember that the TA$'$ mode may also have anomalous intensity near (200), and thus this method of normalization may underestimate changes in anomalous TA$'$ intensity with composition. In each region, data were averaged within a certain H-range and plotted along K; the background was determined, and then these data subsets were numerically integrated along K with the background subtracted. To illustrate, Figure 18 shows constant-energy slices for data obtained at HYSPEC for NSC70, SC65, and FeTe at 300 K. Spectral weight near (200) corresponds to the LA and TA modes; these two modes would be clearly distinguishable if the color scale were set to a greater intensity range. We note that our SC65 sample had two domains with orientations in the $HK0$ plane separated by $\sim$8°-9°, explaining why the (200) phonon spectral weight is more spread out compared to the NSC70 and FeTe data. The black and white rectangles represent the regions used for integrating spectral weight near (200) and (100).

Figures 19 and 20 show the cuts along K used to integrate the spectral weight near (200) and (100). For Fig. 19, data were averaged within $1.5 \leq H \leq 2$ and $\Delta(\hbar\omega) = \pm 0.5$ meV. The greater intensity near (200) meant that data could be obtained at 1 meV step sizes, but the limited detector coverage for $\hbar\omega > 0$ meV meant that only neutron energy-gain (i.e., $\hbar\omega < 0$

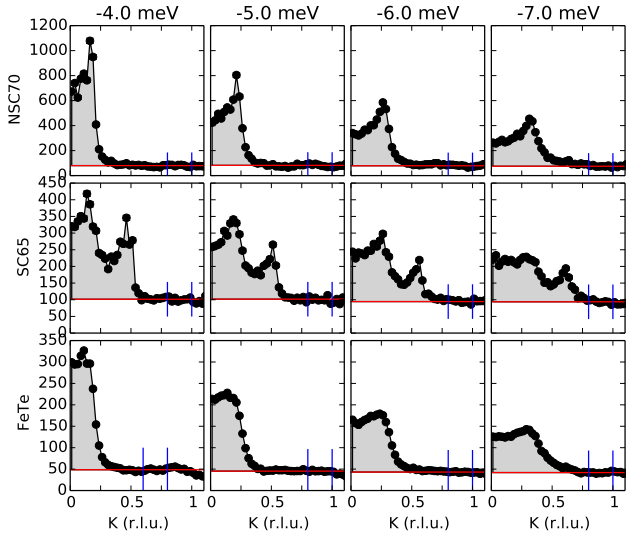

Figure 19: Neutron scattering intensity along K, averaged within $1.5 \leq H \leq 2$ and $\Delta(\hbar\omega) = \pm 0.5$ meV of the energy transfers listed on top for each column. The composition for each row is listed on the vertical axis. All data were taken at 300 K on HYSPEC in the $HK0$ plane. The shaded areas are the integrated phonon intensities near (200) used for normalization. The red lines denote the background level, determined by the mean intensity within the regions delimited by the blue lines.

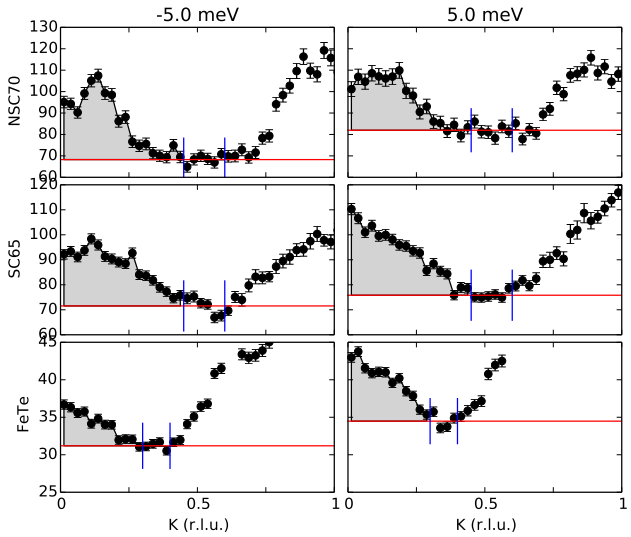

Figure 20: Neutron scattering intensity along K, averaged within $1 \leq H \leq 1.5$ and $\Delta(\hbar\omega) = \pm 1.5$ meV of the energy transfers listed on top for each column. The composition for each row is listed on the vertical axis. All data were taken at 300 K on HYSPEC in the $HK0$ plane. The shaded areas are the integrated phonon intensities near (100), used for comparing the relative strengths of the anomalous TA$'$ mode intensity. The red lines denote the background level, determined by the mean intensity within the regions delimited by the blue lines.

meV) scattering data was used. For Fig. 20, data were averaged within $1 \leq H \leq 1.5$ and $\Delta(\hbar\omega) = \pm 1.5$ meV. In both sets of plots, the background, shown as a red line, was calculated by finding the mean of the intensity within the regions delimited by the vertical blue lines, which were located by eye to find an appropriate background region. The shaded areas correspond to the values computed by numerical integration along K of the spectral weight. For the data in Fig. 19, the background is fortunately clearly distinguishable from the (200) phonon spectral weight. The two peaks in the SC65 cuts are due to the two domains present in this sample. For the data in Fig. 20, there is more ambiguity in distinguishing background from (100) phonon spectral weight, though for NSC70 the distinction is relatively clear.

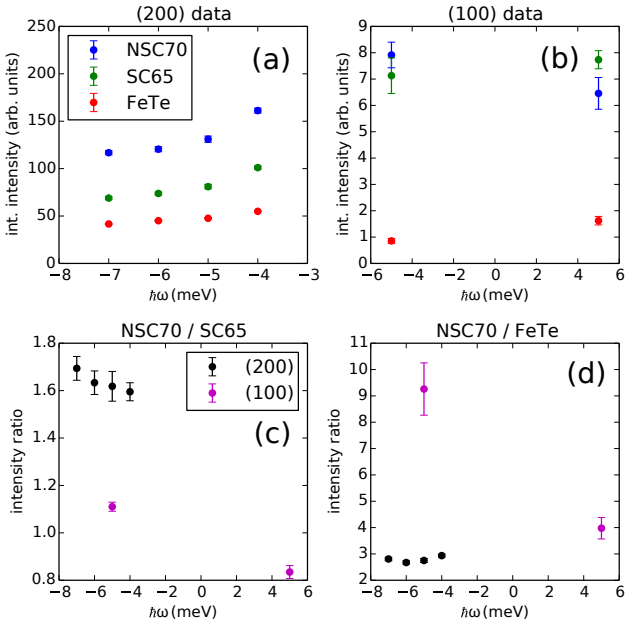

Figure 21: (a) Integrated intensities near (200) corresponding to the gray regions in the plots in Fig. 19. (b) Integrated intensities near (100) corresponding to the gray regions in the plots in Fig. 20. See text for details of integration. (c) Ratios of the integrated intensities shown in (a) and (b) for the NSC70 intensities divided by the SC65 intensities. (d) Ratios of the integrated intensities shown in (a) and (b) for the NSC70 intensities divided by the FeTe intensities.

Figure 21 shows the results of computing the integrated areas of the shaded regions in Figures 19 and 20[15]. Fig. 21(a) and (b) show the integrated intensities near (200) and (100), respectively. Fig. 21(c) and (d) show the calculated intensity ratios from the data shown in Figures 21(a) and (b). In Fig. 21(c), the NSC70/SC65 (200) intensity ratios seem consistent with each other, and while the (100) intensity ratios show a much larger mutual discrepancy, both values are well beneath the (200) intensity ratios. These results suggest that the anomalous TA′ mode intensity is relatively weaker in NSC70 than in SC65, which, together with our earlier intensity comparisons for SC45 and NSC45Ni10, suggest a correlation between the ability of $Fe_{1+y-z}Ni_zTe_{1-x}Se_x$ compounds to host superconductivity, and the intensity of the anomalous TA′ mode intensity in the $HK0$ plane.

For completeness, we also compare the intensity ratios for NSC70 and FeTe. Both values for the ratio of the intensities of the (100) spectral weight are larger than the four ratios for the (200) spectral weight, suggesting that the FeTe anomalous TA′ mode intensity is relatively weak compared to NSC70; however the two values obtained for the (100) integrated intensities are clearly inconsistent with each other, and better data are needed to more quantitatively estimate the anomalous TA′ mode intensities in FeTe.

4.5 Discussion

Our primary result is that the c-axis polarized transverse acoustic mode, which we have denoted the TA′ mode, has nonzero intensity in the $HK0$ plane, even though c-axis polarized modes in the $HK0$ plane should have zero intensity according to the $\mathbf{Q} \cdot \xi$ factor in Eq. 17. Also, a second mode appears to be visible along $(00L)$, which should be forbidden for the same reason. Another characteristic of the TA′ anomalous intensity is that it is clearly visible near forbidden Bragg peaks, even though modes which are allowed to be visible in the $HK0$ plane (and which are clearly visible near a non-forbidden Bragg peak) have intensities so weak as to be undetectable in our data near these wavevectors.

[15]Numerical integration was done by the rectangular method. For the error bars, two contributions were added in quadrature. The first contribution was from propagating the error of the sum of the individual intensities. The second contribution was from the uncertainty of the background, which was defined as the standard deviation of the mean of the points sampled in computing the background times the range in K of the area of integration.

To explain this anomalous behavior, we should check our assumptions. For instance, we assumed that, for wavevectors in the $HK0$ plane, one of the three acoustic modes was polarized purely along the c-direction. This assumption follows from group theory[16], given the reported symmetries of $Fe_{1+y-z}Ni_zTe_{1-x}Se_x$ within the temperature ranges we measured and the assumption of a perfect crystal. However, it is not difficult to imagine that an obstacle in the lattice would alter the directions of atomic vibrations, and there are a number of sources of disorder present in this system, e.g., interstitial iron and Te/Se substitutional disorder. Local structural fluctuations due to proximity of the system to an ordered phase, such as the orbital ordering transition reported for $Fe_{1+y}Te$ [130], may also play a role [10].

For illustration, we provide a picture of how Te/Se chemical disorder may explain some of our findings. As noted above, the TA$'$ mode has anomalous behavior, such as its prominence near forbidden Bragg peaks and its visibility in the $HK0$ plane in general despite the ab-polarized TA mode not having similarly anomalous intensity in the $H0L$ plane. Why does the TA$'$ branch show anomalous behavior and not the other two branches? One possibility may be that Te/Se substitutional disorder results in positional disorder along the c-axis, due to Se and Te having two distinct c-axis locations [131]. As a result, the restoring forces along the c-direction may be different from site to site; while we would expect the restoring forces in the ab-plane to also be affected, we might presume that they are less affected, leading to less anomalous behavior in lattice vibrations in the ab-plane. Now, $Fe_{1+y}Te$ does have anomalous TA$'$ mode intensity despite the absence of Te/Se substitutional disorder, so that kind of disorder cannot be the sole cause, though the data in Fig. 21(d) suggest that the anomalous TA$'$ mode intensity is significantly weaker in FeTe.

As for the visibility of the anomalous mode near forbidden Bragg peaks, we note that the cause of the forbiddenness of these peaks is due to a combination of the anions' ab-plane positions being at high-symmetry locations, and of the $L = 0$ constraint which ignores c-axis positioning. For acoustic mode oscillations polarized in the ab-plane, both anions move roughly together, and the relative positioning of the anions in the ab-plane during vibration might not deviate strongly from that in equilibrium that resulted in the peaks being forbidden. On the other hand, for vibrations (ideally)

[16]For example, one could follow the procedure in Ch. 11 of Ref. [129] given the high-temperature tetragonal $P4/nmm$ symmetry.

along the c-direction, any ab-plane displacements (the only kind that can be detected by neutrons for an arbitrary $HK0$ wavevector) would be due to disorder and not necessarily expected to be in similar directions. More detailed analysis is needed to determine how plausible this picture is, and quantitatively, how neutron scattering intensity should be affected.

As for the possible correlation between the anomalous TA$'$ intensity along ($H00$) or within $HK0$ and the ability to host superconductivity, it is not clear how the correlation could arise. If the disorder were due to chemical disorder, one would assume that, for similar Se content x, non-superconducting samples would have greater disorder than superconducting samples due either to interstitial iron or nickel substitution, and naively one might assume that samples with greater disorder would have a more intense anomalous mode. However, we see the opposite trend between SC45 and NSC45Ni10 and between SC65 and NSC70. On the other hand, we could consider the possibility of the disorder being the result of proximity to an ordered phase. The ferro-orbital ordering reported in Ref. [130] for $Fe_{1+y}Te$ is only present at low-temperature. There do appear to be magnetic excitations that are correlated with the ability to host superconductivity [39], but they too show a large temperature-dependence, and at higher temperatures ($\sim$300 K) the magnetic excitations for superconducting samples approach those seen in non-superconducting samples. Chemical disorder, on the other hand, should be temperature-independent in the range of our measurements. Unfortunately, the intensity temperature-dependence data in Fig. 16 are not quite good enough to determine whether the chemical disorder or magnetic/orbital fluctuations picture is more likely to be the case. More data on other samples is needed to test the correlation between anomalous TA$'$ mode intensity and the ability to host superconductivity, and more precise data and further analysis is needed to see which potential causes are likely to be responsible for the anomalous TA$'$ mode intensity.

4.6 Summary

The acoustic phonon branches of five $Fe_{1+y-z}Ni_zTe_{1-x}Se_x$ compositions were investigated by neutron scattering. We further characterized the anomalous phonon branch reported in Ref. [10]. Based on the dispersion, we identified the anomalous mode to be the c-polarized TA$'$ mode. However, the neutron scattering intensity of this mode in the $HK0$ plane is expected to be zero. Also, the TA$'$ branch is clearly visible in BZs corresponding to forbidden

Bragg peaks even though the LA and TA branches are too weak to be detected in these BZs. A possible explanation for these anomalous behaviors may be disorder causing deviation of the polarization of lattice vibrations, but more analysis is needed to determine which kinds of disorder are likely to be responsible. No clear anomalous temperature dependence in the dispersion or intensities of the TA$'$ mode along $(H00)$ was observed. When comparing data from different compositions on the same instrument, a possible tendency was observed for superconducting samples to have greater anomalous TA$'$ mode intensities.

5 Magnetic excitations in superconducting $La_{1.9}Ca_{1.1}Cu_2O_{6+\delta}$

In this Section, I present neutron scattering experiments on $La_{1.9}Ca_{1.1}Cu_2O_{6+\delta}$, a bilayer cuprate superconductor made superconducting by high-pressure annealing in an oxygen-containing atmosphere. This research is unpublished. I have had help from Genda Gu and Ruidan Zhong in synthesizing this material, from Guangyong Xu and John Tranquada in analyzing the neutron scattering data, and from Alexander Kolesnikov of Oak Ridge National Laboratory for providing assistance for our neutron scattering experiments as instrument scientist at the SEQUOIA instrument at the Spallation Neutron Source.

5.1 Abstract

We report inelastic neutron scattering on a single crystal of the bilayer cuprate compound $La_{1.9}Ca_{1.1}Cu_2O_{6+\delta}$ made superconducting by high-pressure annealing in an oxygen-containing atmosphere. The observed magnetic excitations are commensurate at low energy transfer, rather than incommensurate as seen in other superconducting hole-doped cuprates. However, the temperature dependence of the intensity of the excitations is inconsistent with that reported for the commensurate excitations in weakly hole-doped, non-superconducting cuprates.

5.2 Introduction

The mechanism of superconductivity in the high-T_C cuprate superconductors is still not well understood, but magnetic interactions are thought to play a role, and neutron scattering measurements have shown a trend in the evolution of magnetic excitations with hole doping. The cuprate superconductors consist of many families of similar materials, each with CuO_2 planes that are thought to be responsible for the superconductivity, and each having a similar phase diagram [132] such as that shown in Fig. 22. The undoped "parent compound" has antiferromagnetic order below a certain temperature. With doping, magnetic order is gradually suppressed and superconductivity is induced. The superconducting transition temperature T_C as a function of doping forms a dome in the phase diagram, with "optimal doping" occurring

at maximum T_C, and "underdoped" and "overdoped" samples having less or greater than optimal doping, respectively. Either hole- or electron-doping can be done, yielding roughly similar phase diagrams.

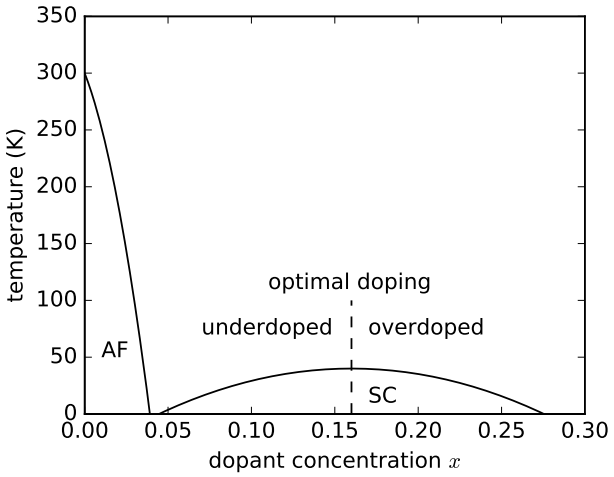

Figure 22: Schematic illustration of the cuprate phase diagram, based on the phase diagram for $La_{2-x}Sr_xCuO_4$ [133]. "SC" labels the superconducting region of the phase diagram, and "AF" labels the region with long-range antiferromagnetic order; the upper boundaries of these regions represent the transition temperatures for superconductivity and antiferromagnetic order, respectively.

Doping can be done by element substitution or by controlling the amount of oxygen in the lattice. For example, the "La-214" family, which has La_2CuO_4 as the parent compound, can be made superconducting either by substituting La with Ca, Sr, or Ba ($La_{2-x}Ae_xCuO_4$ with Ae=Ca, Sr, or Ba), or by adding interstitial oxygen ($La_2CuO_{4+\delta}$) through electrochemical means or by annealing at high pressure in an oxygen-containing atmosphere. One important difference between these two doping methods is that, for relatively low temperatures ($T < 400$ K), substituted Ca, Sr, or Ba tends to be fixed to certain sites, whereas the interstitial oxygen atoms tend to remain mobile [12]. For certain δ values, at low enough temperatures an ordered superlattice of interstitial oxygen may form, with certain "stages" possible which are characterized by the periodicity of the structural modulation along the

c-axis [12, 134]. For δ in between ordered phases, phase separation into these phases and the parent compound can occur when the system is cooled into a miscibility gap.

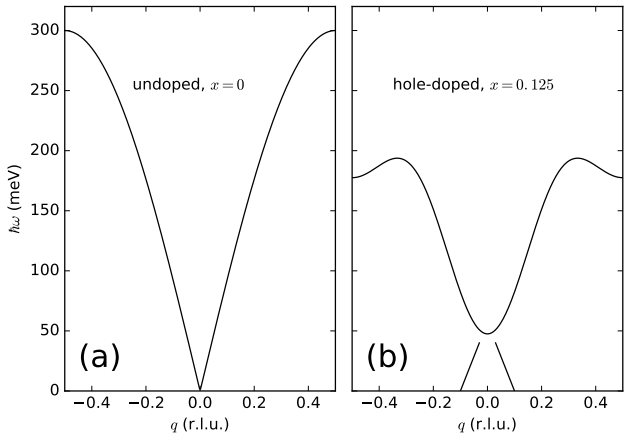

Figure 23: Schematic depiction of how the dispersion of the magnetic excitations changes with hole-doping in the cuprates (a) for the parent compound and (b) for sufficient hole-doping. Momentum q is defined in reciprocal lattice units away from a magnetic Brillouin zone center along [100]. Dispersions are roughly based on those shown in Ref. [21].

In light of the common belief that magnetic interactions may play an important role in the superconductivity of the cuprates, the magnetic excitations of the cuprates have been carefully studied by neutron scattering, and, for hole-doping, a trend has emerged. For parent compounds, magnetic excitations take the form of antiferromagnetic spin waves dispersing out from the magnetic Bragg peaks at wavevectors $\mathbf{Q}_{AF}$ [135] (see Fig. 23(a)). The energies and intensities of the spin wave dispersion appear to match what is theoretically predicted [136]. With increased doping in the hole-doped cuprates, the magnetic excitations near $\mathbf{Q}_{AF}$ tend to transform into an "hourglass"-shaped dispersion where spectral weight rises from elastic incommensurate positions around $(0.5, 0.5)$, reaches a bottleneck at a crossing energy, then disperses away from $(0.5, 0.5)$ for higher energy transfers (see Fig. 23(b)). (These coordinates correspond to the HK-plane in reciprocal lattice units for a pseudotetragonal unit cell; these excitations are diffuse along L.) After

scaling by the nearest-neighbor magnetic interaction energy J, the hourglass dispersions of many hole-doped cuprates, including $La_{2-x}Ba_xCuO_4$ (LBCO), $La_{2-x}Sr_xCuO_4$ (LSCO), $YBa_2Cu_3O_{6+\delta}$ (YBCO), and $Bi_{2+x}Sr_{2-x}CaCu_2O_{8+\delta}$ (BSCCO) have a similar shape [11]. Incommensurate magnetic excitations have also been reported for oxygen-doped $La_2CuO_{4+\delta}$ [12]. On the other hand, in electron-doped cuprates, commensurate spin-wave magnetic excitations may persist to optimal doping, such as in $Nd_{2-x}Ce_xCuO_4$ (NCCO) [137] and $Pr_{1-x}LaCe_xCuO_{4-\delta}$ (PLCCO) [138, 139].

A number of changes in the magnetic excitations can occur as a function of temperature. For superconducting compositions, as one cools below T_C, a "spin gap" of decreased neutron scattering intensity below a certain energy may form, together with an increase in intensity above the spin gap known as the "resonance". The resonance has been reported in YBCO, BSCCO, $Tl_2Ba_2CuO_{6+\delta}$, $HgBa_2CuO_{4+\delta}$, and LSCO [140–142]. The resonance can be sharply-peaked in energy (i.e., resolution-limited), such as in YBCO and $Tl_2Ba_2CuO_{6+\delta}$, or broad, as in BSCCO ($\Delta E \sim 13$ meV) [143]. Substituting Ni for Cu in $YBa_2(Cu_{1-y}Ni_y)_3O_7$ was reported to broaden the energy-width of the resonance without changing the carrier concentration, suggesting that the broader width of the resonance was related to disorder [140, 144]. The energy of the resonance E_r appears to scale roughly with T_C, and is around 40 meV in optimally doped YBCO with $T_C = 93$ K [140]. The resonance is usually found near the hourglass dispersion crossing energy, and is thus commensurate; however, the resonance is found at incommensurate positions in LSCO since T_C is substantially lower in LSCO (relative to J) than in the other cuprates where a resonance has been found [21]. Similar resonance-like features have also been observed in inelastic neutron scattering experiments on iron-based superconductors and heavy fermion superconductors [141]. There is not yet agreement on an explanation for the resonance in the cuprates, despite numerous experimental studies and theoretical proposals. Descriptions of the resonance have been proposed in both itinerant-spin and localized-spin pictures [143].

As for non-superconducting, weakly hole-doped cuprates, less attention has been paid to how their magnetic excitation intensities change with temperature, but when the intensities at various energies are plotted with respect to temperature, a peak is seen which lies at greater temperature for greater energy transfers, at least within $\sim 2 \leq \hbar\omega \leq 45$ meV [145]. This behavior corresponds to an ω/T scaling relation for $\chi''(\mathbf{Q}, \omega)$, the intensity divided by the Bose factor. Data for $La_{1.965}Ba_{0.035}CuO_4$ [146] and $YBa_2Cu_3O_{6.33}$ [147]

are qualitatively consistent with this trend, with both showing an increase in intensity with temperature for sufficiently large $\hbar\omega$ (e.g., $\geq$5 meV for $La_{1.965}Ba_{0.035}CuO_4$), and with differences in temperature approaching zero for even higher $\hbar\omega$.

Given the quirks that individual families of the cuprates exhibit, it is helpful to compare the properties of a large number of these families to identify common characteristics. One family that has been relatively infrequently studied is $La_{2-x}(Ca,Sr)_xCaCu_2O_{6+\delta}$ (La-2126), which is a bilayer variant of the single-layer La-214 family. While La-214 can be made superconducting by substitution of La with Ca, Sr, or Ba or by introducing interstitial oxygen, for La-2126, there is a limited stability range for Ca/Sr substitution, so high-pressure oxygen annealing that induces excess oxygen δ is needed in addition to Ca/Sr substitution to dope La-2126 to the point of bulk superconductivity [148]. Due to the relative rarity of high-pressure ($\sim$670 MPa) furnaces, there have not yet been inelastic neutron scattering experiments on large single crystals of annealed, superconducting La-2126 compounds, though elastic and inelastic measurements were performed on single crystals of unannealed, non-superconducting $La_{1.9}Ca_{1.1}Cu_2O_{6+\delta}$ and unannealed, weakly-superconducting $La_{1.85}Sr_{0.15}CaCu_2O_{6+\delta}$ [149]. These measurements showed long-range antiferromagnetic (AFM) order in $La_{1.9}Ca_{1.1}Cu_2O_{6+\delta}$ and short-range AFM order in $La_{1.85}Sr_{0.15}CaCu_2O_{6+\delta}$, with ordering commensurate in both cases. A tetragonal-to-orthorhombic structural phase transition upon cooling has been observed for both $La_{2-x}Sr_xCaCu_2O_{6+\delta}$ and $La_{2-x}Ca_{1+x}Cu_2O_{6+\delta}$ [149, 150].

We have successfully grown a $La_{1.9}Ca_{1.1}Cu_2O_{6+\delta}$ single crystal and induced superconductivity by high-pressure oxygen annealing. We report neutron scattering measurements on this crystal, finding magnetic excitations that are commensurate at low energy transfers, similar to those of undoped or weakly hole-doped cuprates. However, the temperature-dependence of the intensity, which decreases with temperature for energy transfers above 8 meV, is much different from those seen in weakly hole-doped cuprates, where the intensity increases with temperature for comparable ranges of temperature and energy transfer. We also see superstructural peaks that may indicate the presence of ordering due to interstitial oxygen atoms.

5.3 Materials and Methods

Measurements were taken on a 6.2g $La_{1.9}Ca_{1.1}Cu_2O_{6+\delta}$ single crystal grown by the traveling solvent floating zone method [151] and annealed under a high-pressure mixture of 20% oxygen and 80% argon in a hot isostatic press. The sample measured with neutron scattering was subjected to three separate annealing treatments within a two-week period: 1180°C at 100 kPSI for 10 hours, 1150°C at 90 kPSI for 5 hours, and finally 1130°C at 80 kPSI for 16 hours.

Magnetization measurements were performed using a Quantum Design Magnetic Properties Measurement System. Samples measured for susceptibility measurements were cooled quickly from 300 to 20 K in ∼2 minutes by inserting into the magnetometer when it was already cooled below 20 K. Inelastic neutron scattering experiments were performed on the SEQUOIA time-of-flight spectrometer at the Spallation Neutron Source at Oak Ridge National Laboratory [152]. Samples measured for neutron scattering were cooled from 300 to 4 K in ∼1 hour[17]. Two incident energies E_i were used: 40 meV and 120 meV, with most of our analysis focusing on the $E_i = 40$ meV data. The settings for the T_0 and Fermi chopper (F1) frequencies were as follows: at $E_i = 40$ meV, $T_0 = 30$ Hz and F1=180 Hz; at $E_i = 120$ meV, $T_0 = 60$ Hz and F1=240 Hz; and at $E_i = 300$ meV, $T_0 = 120$ Hz and F1=480 Hz. Data were taken at 4, 55, and 200 K. Each data set for a given E_i and temperature took ∼14 hours to obtain. A tetragonal unit cell with lattice parameters $a = 3.83$ Å and $c = 19.36$ Å was used in neutron scattering data analysis. All wavevectors are reported in reciprocal lattice units as (H, K, L). In all neutron scattering intensity maps, the data were smoothed, and white regions represent a lack of data due to the region existing outside the coverage area of the detector. All neutron scattering data were mapped into the region of $H \geq 0$, $K \geq 0$, and $L \geq 0$ by reflection across $H = 0$, $K = 0$ and $L = 0$ before further processing unless otherwise noted. Error bars represent statistical error and correspond to 1 standard deviation from the observed value.

[17] We note that oxygen-doped $La_2CuO_{4+\delta}$ shows somewhat lower T_C and much higher diamagnetic shielding fractions when cooling quickly rather than slowly [134]. Thus, annealed $La_{1.9}Ca_{1.1}Cu_2O_{6+\delta}$ may have different superconducting behavior in our susceptibility measurements than in our neutron scattering measurements due to the different cooling rates. We have not yet measured the susceptibility under slow-cooling.

5.4 Data and Analysis

5.4.1 Magnetic susceptibility

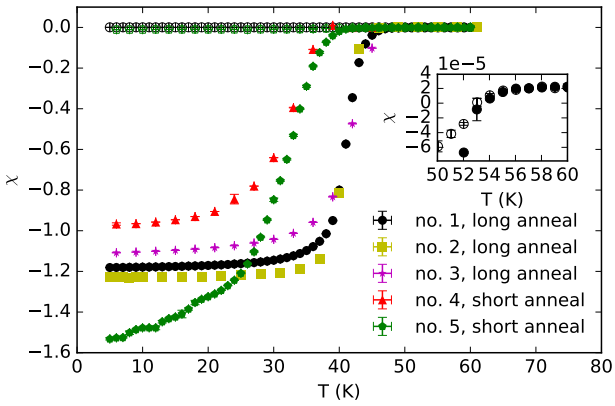

Figure 24: Diamagnetic shielding signals from several samples with nominal composition $La_{1.9}Ca_{1.1}Cu_2O_{6+\delta}$ after high pressure oxygen annealing. χ is the magnetic susceptibility. Samples no. 1, no. 2, and no. 3 were annealed in three consecutive treatments within two weeks: 1180°C at 100 kPSI for 10 hours, 1150°C at 90 kPSI for 5 hours, and 1130°C at 80 kPSI for 16 hours. Samples no. 4 and no. 5 were annealed only once, at 1180°C at 100 kPSI for 10 hours. Sample no. 3 was cut from the inside of a larger annealed piece, whereas the other samples were measured as-annealed. A 10 Oe field was applied, and data were taken under zero-field-cooling (closed symbols) and field-cooling (open symbols, for samples no. 1 and no. 5) conditions. The inset shows a zoomed-in version of the data for sample no. 1, highlighting the onset of the superconducting transition near 55 K. The masses of samples 1 through 5 were all within 29 to 159 mg. The magnetic susceptibility χ was calculated assuming a density of 6.244 g/cm^3, which was calculated from the lattice constants listed in Ref. [149] assuming a composition of $La_{1.9}Ca_{1.1}Cu_2O_6$.

As evidence for the bulk superconductivity of the crystal used for neutron scattering, in Fig. 24 we show magnetic susceptibility χ vs. temperature for five smaller annealed samples with nominal composition $La_{1.9}Ca_{1.1}Cu_2O_{6+\delta}$. An ideal superconductor should completely shield its bulk from applied magnetic fields, corresponding to a magnetic susceptibility under zero-field-cooling

of $\chi = -1$ that would indicate $\sim$100% superconducting volume fraction; thus, we can say that all of the samples measured were bulk superconductors. ($\chi < -1$ is allowed due to the demagnetization effect.) All samples present in Fig. 24 were measured as-annealed, except for no. 3, which was cut from the center of a larger as-annealed piece to verify that oxygen could penetrate deeply enough to make the whole sample superconducting. Samples no. 1, no. 2, and no. 3 were annealed with the full annealing treatment described in Section 5.3, the same annealing conditions as for the crystal whose neutron scattering data is presented below. Samples no. 4 and no. 5 were only annealed once, at 1180°C at 100 kPSI for 10 hours. The samples annealed for the longer treatment exhibited bulk superconductivity at higher temperatures than for samples annealed for the shorter treatment, and appear to have a sharper transition to the superconducting state. These results suggest that longer annealing times led to increased oxygen doping and higher T_C in a larger portion of the sample, though more annealing experiments are needed to clarify these trends. We note that, though bulk superconductivity appeared between 40 to 45 K, the onset of the diamagnetism could be as high as 55 K as seen for sample no. 1 in the inset of Fig. 24.

5.4.2 Neutron scattering

Elastic neutron scattering data for $T = 4$, 55, and 200 K are shown in Fig. 25. The left column shows data at $K = 0$, and the right column shows data at $K = 0.5$. For $K = 0$, structural Bragg peaks are expected for even integer $H + K + L$. In addition, though, superstructural Bragg peaks can be seen at many points $(0.5n, 0, 1.25m)$ for integer n and m. Superstructural peaks in oxygen-doped $La_2CuO_{4+\delta}$ have been attributed to distortion due to the presence of interstitial oxygen [134], and a similar effect may be present in our annealed $La_{1.9}Ca_{1.1}Cu_2O_{6+\delta}$ sample. There does not seem to be a substantial temperature dependence in the intensity of these peaks up to 200 K, suggesting that the interstitial oxygen atoms responsible for the ordering may be fixed rather than mobile within 4 to 200 K. Along the L direction at integer H, diffuse scattering and possibly additional peaks can be seen, which may indicate structural disorder along the c-direction. Part of this disorder may be due to intergrowth-like defects of $La_{2-x}Ca_xCuO_{4+\delta}$ within $La_{2-x}Ca_{1+x}Cu_2O_{6+\delta}$, as detected in another annealed, superconducting $La_{1.9}Ca_{1.1}Cu_2O_{6_\delta}$ crystal by transmission electron microscopy and electron diffraction [153].

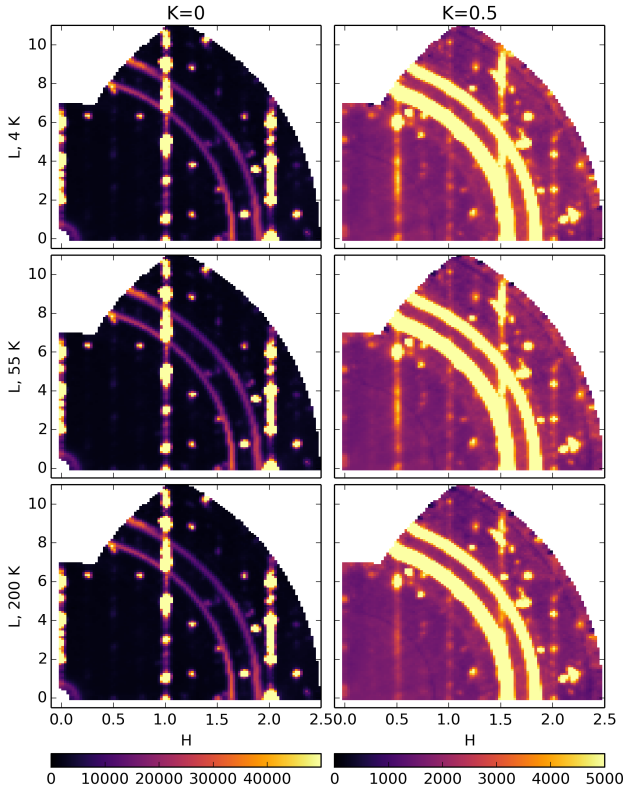

Figure 25: Elastic neutron scattering intensity maps in the $(H, 0, L)$ and $(H, 0.5, L)$ planes at 4, 55, and 200 K. Data were averaged within $\Delta K = \pm 0.1$ r.l.u. about $K = 0$ for the left column and $K = 0.5$ for the right column. Data were also averaged within $-0.5 \leq \hbar\omega \leq 0.5$ meV.

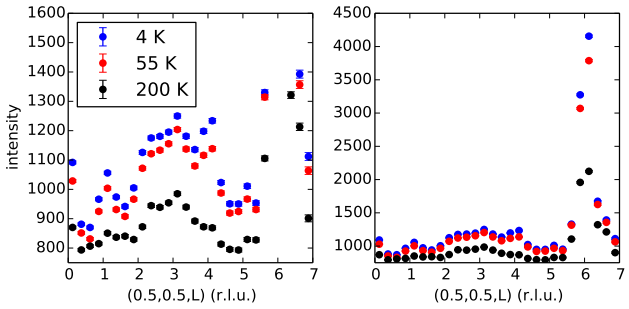

Figure 26: Elastic neutron scattering intensity along $(0.5, 0.5, L)$, averaged within $0.4 \leq H \leq 0.6$, $0.4 \leq K \leq 0.6$, and $-0.5 \leq \hbar\omega \leq 0.5$, at three different temperatures. Both subplots show the same data at different intensity scales.

For half-integer H and $K = 0.5$, clear peaks are only seen for $L = 6$, in contrast to unannealed $La_{1.9}Ca_{1.1}Cu_2O_{6+\delta}$, where peaks corresponding to orthorhombic and long-range AFM order were clearly seen at all integer L [149][18]. The intensity along $(0.5, 0.5, L)$ can be seen in more detail in Fig. 26. Weak peaks may be present for some integer L values such as $L = 1, 3, 4$, and 5, along with the strong peak at $L = 6$. These weak peaks are much weaker than those seen in unannealed $La_{1.9}Ca_{1.1}Cu_2O_{6+\delta}$ [149], suggesting little 3-dimensional antiferromagnetic order in our crystal. These peaks seem to decrease substantially from 55 to 200 K, roughly consistent with the temperature dependence of the AFM and orthorhombic order in unannealed $La_{1.9}Ca_{1.1}Cu_2O_{6+\delta}$ [149].

Diffuse scattering rods can be seen along L at half-integer H and $K = 0.5$; these rods were also seen in unannealed $La_{1.9}Ca_{1.1}Cu_2O_{6+\delta}$ and were identified as magnetic 2-dimensional correlations [149]. Similar 2-dimensional magnetic correlations were seen in weakly-doped $La_{2-x}Ba_xCuO_4$ [154]. The temperature-dependence of the intensity of these diffuse scattering rods can

[18]Since the orthorhombic symmetry corresponds to a small distortion from a tetragonal unit cell, we used a tetragonal unit cell, but the consequence of not using the orthorhombic unit cell is the appearance of orthorhombic structural Bragg peaks at half-integer H and K. If the symmetry is orthorhombic, Bragg peaks are expected to appear at half-integer H and K and even integer $L \neq 0$. AFM Bragg peaks are expected at half-integer H and K and all integer $L \neq 0$ [149].

be seen in Fig. 26. Remarkably, the temperature-dependence of the diffuse intensity of these rods is much different for annealed and unannealed $La_{1.9}Ca_{1.1}Cu_2O_{6+\delta}$. Our data on annealed $La_{1.9}Ca_{1.1}Cu_2O_{6+\delta}$ shows only a small decrease in intensity from 4 to 55 K, unlike the decrease by roughly half seen for unannealed $La_{1.9}Ca_{1.1}Cu_2O_{6+\delta}$ from ∼10 to 50 K at $(0.5, 0.5, 2.5)$ [149]. Interestingly, underdoped $La_{2-x}Ba_xCuO_4$ samples with $0.0125 \leq x \leq 0.035$ also showed large drops in the intensity of elastic 2-dimensional magnetic correlations at this wavevector when heating from 1.5 to 35 K [154], suggesting a link between underdoped LBCO and unannealed $La_{2-x}Ca_{1+x}Cu_2O_{6+\delta}$ and a contrast with the behavior in our more heavily doped crystal. (We note that, although we describe the data in Fig. 26 as "elastic", measurements with finer energy-resolution might reveal that a portion of the 2-dimensional magnetic correlations is actually quasielastic. In $La_{2-x}Ba_xCuO_4$ with $x = 0.0125$, although the bulk of the intensity was an elastic component whose intensity dropped quickly from 1.5 to 35 K, a weaker inelastic component within $0.15 \leq \hbar\omega \leq 0.8$ survived to above 160 K [154].)

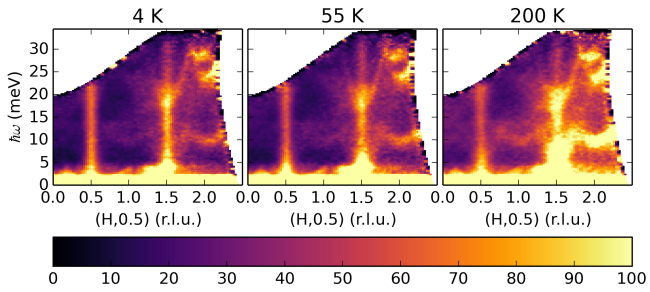

Figure 27: Neutron scattering intensity maps focusing on the temperature-dependence of the steeply-dispersing magnetic excitations and the optic phonons. Data are plotted along energy transfer $\hbar\omega$ and $(H, 0.5, 3)$ directions, averaged within $2 \leq L \leq 4$ and $0.4 \leq K \leq 0.6$. Data taken at $E_i = 40$ meV.

We now turn to the inelastic neutron scattering data. Figure 27 shows that the magnetic excitations are commensurate, dispersing steeply out from $K = 0.5$ and $H = 0.5$ or 1.5 wavevectors. Intensity is plotted against $\hbar\omega$ and H with $K = 0.5$. (As for L, the excitations at half-integer H and K have

a broad, sinusoidal L-dependence, as shown below, so data were averaged near $L = 3$ to focus on wavevectors where the magnetic excitation intensity was maximum and to choose an L-range with a reasonably large $\hbar\omega$-range.) Various optic phonon modes dispersing horizontally can also be seen, with intensity increasing, as expected, with temperature and $|\mathbf{Q}|$. Another view of the magnetic excitations can be seen in Fig. 28, which shows data taken with a higher incident energy ($E_i = 120$ meV, rather than $E_i = 40$ meV for Fig. 28) to probe a greater range of $\hbar\omega$ and $\mathbf{Q}$. The magnetic excitations are seen to disperse steeply and remain near half-integer H and K up to at least 100 meV, though they are expected to eventually disperse outwards toward Brillouin zone boundaries. It is remarkable that the commensurate magnetic excitations seen in Figures 27 and 28 resemble those in the weakly hole-doped La-214 compound $La_{1.965}Ba_{0.035}CuO_4$ [146], since cuprates hole-doped to the point of inducing superconductivity typically have incommensurate low-energy magnetic excitations [11]. There may be exceptions; underdoped, superconducting $HgBa_2CuO_{4+\delta}$ may be another example of a superconducting hole-doped cuprate with commensurate magnetic excitations. However, the dispersion in underdoped $HgBa_2CuO_{4+\delta}$ is much different from that seen in our data, with a gap below $\hbar\omega \approx 30$ meV and a clear dispersion above $\sim$60 meV [155], rather than the lack of a gap and much steeper dispersion seen in our data.

Figure 29 shows the neutron scattering intensity in the $(H, K, 3)$ plane at various temperatures and energy transfers. At $\hbar\omega = 4$ meV, slash-like features from spurious scattering are, unfortunately, present, and may possibly arise from multiple scattering in which Bragg scattering within the sample is followed by incoherent scattering within surrounding materials. For other $\hbar\omega$, the main features are the magnetic excitations at $(0.5, 0.5, 3)$ and $(1.5, 0.5, 3)$, and the optic phonon features seen at 20 and 24 meV. No incommensurate magnetic scattering intensity is apparent. There is no sign of a low-energy gap in the magnetic excitations; $(H, K, 3)$ intensity maps for $\hbar\omega < 4$ meV (not shown) show a peak down to 2.5 meV, below which possible signals become overpowered by elastic scattering intensity.

In Fig. 30, we show the L-dependence of the magnetic excitations at $(0.5, 0.5, L)$ and $(1.5, 0.5, L)$. To see the L-dependence of the magnetic excitations more clearly, the right column plots intensity along $(0.5, 0.5, L)$ and $(1.5, 0.5, L)$ at the same energy transfers used for the intensity maps on the left. At $(0.5, 0.5, L)$ and $(1.5, 0.5, L)$, we see a broad hump along L, roughly centered near $L = 3$ (except at $\hbar\omega = 20$ meV, where there is a large contribu-

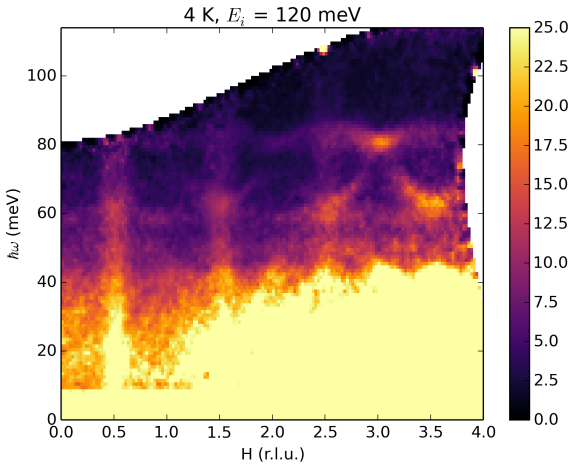

Figure 28: Neutron scattering intensity maps for $E_i = 120$ meV and $T = 4$ K, highlighting the steepness of the magnetic excitations at the magnetic wavevectors $\mathbf{Q}_{AF}$. Data averaged within $0.4 \leq K \leq 0.6$ and $0 \leq L \leq 10$.

tion to the spectral weight from an optic phonon) and having a minimum near $L = 0$. This L-dependence of the magnetic excitations is due to the bilayer magnetic structure factor, as seen in bilayer cuprates such as $YBa_2Cu_3O_{6+\delta}$ [156] and $La_{1.85}Sr_{0.15}CaCu_2O_{6+\delta}$ [149].

To quantitatively estimate the intensity of the $(0.5, 0.5, 3)$ spectral weight and see changes with temperature and energy transfer, we fit 2-dimensional Gaussian functions of the $\mathbf{Q}$ components H and K having the form

$$p_0 + p_1 H + p_2 K + \frac{4A \ln 2}{\pi \kappa_H \kappa_K} e^{-\left(\frac{(H-H_0)^2}{\kappa_H^2} + \frac{(K-K_0)^2}{\kappa_K^2}\right) \ln 2} \tag{19}$$

to data in the $(H, K, 3)$ plane at certain energy transfers. The parameters p_0, p_1, p_2, A, H_0, K_0, κ_H, and κ_K were all allowed to vary freely in fitting. The fitted integrated intensity A is plotted for various temperatures and energy transfers in Figure 31(a). We see that there is a clear decrease in intensity with increasing temperature for $8 \leq \hbar\omega \leq 20$ meV. This temperature dependence does not appear consistent with that of the commensurate magnetic excitations found in underdoped hole-doped cuprates such as $La_{1.96}Sr_{0.04}CuO_4$ [145], $La_{1.965}Ba_{0.035}CuO_4$ [146], or $YBa_2Cu_3O_{6.33}$ [147], where the intensity either increases or remains constant with heating in a similar energy and

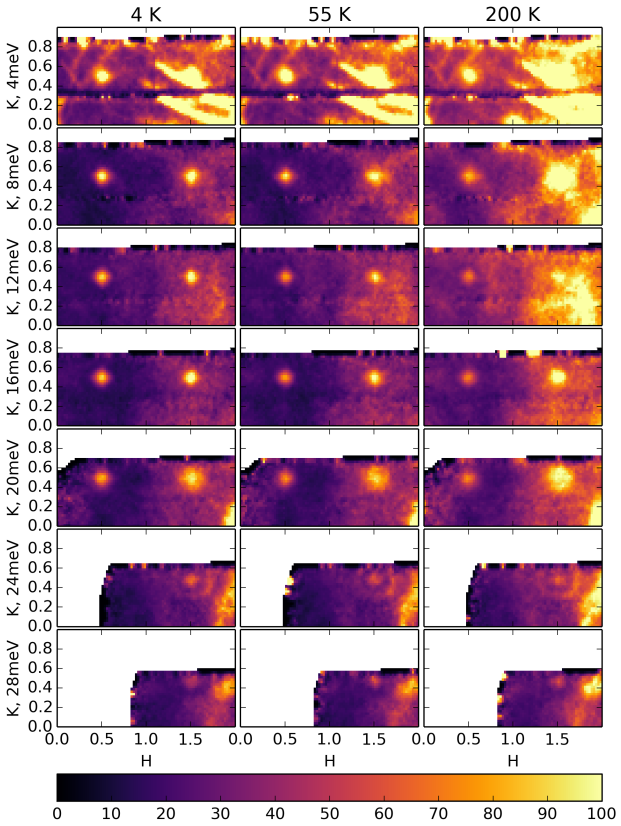

Figure 29: Neutron scattering intensity maps along H and K, averaged within $2 \leq L \leq 4$ and $\Delta(\hbar\omega) = \pm 1$ meV about the energy transfers listed on the vertical axes. The peaks at $(0.5, 0.5, 3)$ and $(1.5, 0.5, 3)$ are magnetic excitations.

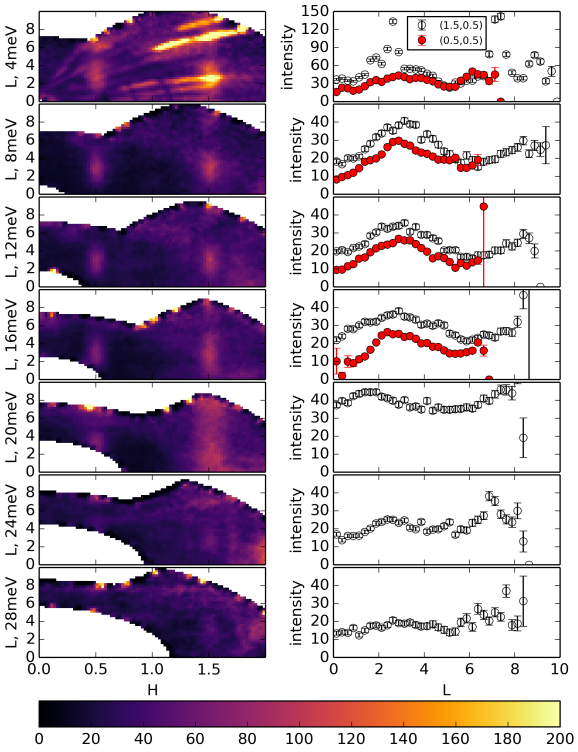

Figure 30: L-dependence of the magnetic excitations at $(0.5, 0.5, L)$ and $(1.5, 0.5, L)$. The left column shows neutron scattering intensity maps in the HL plane, averaged within $0.4 \leq K \leq 0.6$ and within $\Delta(\hbar\omega) = \pm 1$ meV around the energy transfers listed on the vertical axes. Data were taken at $T = 4$ K and $Ei = 40$ meV. The right column shows the intensities of the magnetic excitations along L, averaged within $0.4 \leq K \leq 0.6$, $0.4 \leq H \leq 0.6$ for filled red markers and $1.4 \leq H \leq 1.6$ for open black markers, and $\Delta(\hbar\omega) = \pm 1$ meV around the energy transfers listed on the vertical axes of the left column.

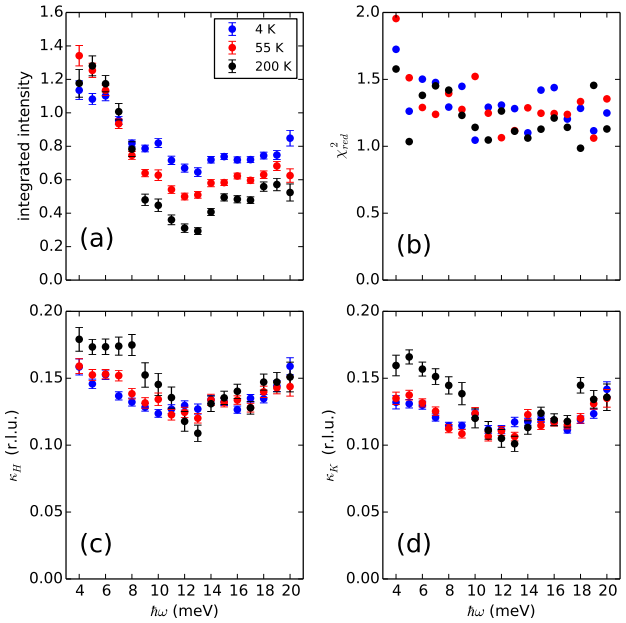

Figure 31: Parameters from fitting of 2-dimensional Gaussian functions to the (0.5, 0.5, 3) magnetic excitations at various energy transfers and temperatures, as detailed in the text. All fitted data subsets were first averaged within $2 \leq L \leq 4$ and $\Delta(\hbar\omega) = \pm 0.5$ meV. (a) Integrated intensities from fits. (b) Reduced χ^2 goodness-of-fit parameter for each fit. (c, d) Width parameters κ_H and κ_K. Errors in the fitted parameters correspond to one standard deviation.

temperature range. The decrease in intensity from 4 to 55 K ($T_C \approx$ 40-45 K) is reminiscent of the superconducting resonance, but there appears not to be a spin gap, and the decrease with temperature is very broad and below where we might expect the resonance to be ($\sim$20 meV, based on trends seen in other cuprates [141]). Unfortunately, we lack clear data to see if the temperature-dependence in Fig. 31 continues to higher energy transfers.

Figure 31(b) shows the reduced χ^2 goodness-of-fit parameter for each fit, showing the satisfactory quality of the fitting. Figures 31(c) and (d) show the width parameters κ_H and κ_K corresponding to full-width-at-half-maximum values along the H and K directions, respectively. Little change in the width of the $(0.5, 0.5, 3)$ peak is seen between 4 and 55 K, but this peak seems to broaden slightly below $\sim$10 meV for 200 K. The upward shift in κ_H compared to the κ_K values is likely an artifact of mapping data into $H > 0$ by reflection about $H = 0$.

5.5 Discussion

To summarize our results:

1. Our annealed $La_{1.9}Ca_{1.1}Cu_2O_{6+\delta}$ crystal is likely a bulk superconductor. The transition temperature for samples annealed under similar conditions is around $\sim$40-45 K, which is somewhat less than the $T_C = 53.5$ K value found for the same nominal composition in Ref. [153]. Longer annealing time seems to increase T_C and sharpen the transition width.

2. Despite the bulk superconductivity, we observe commensurate magnetic excitations similar to those seen in non-superconducting, weakly hole-doped cuprates in the related La-214 system.

3. The temperature-dependence of these magnetic excitations, though, is inconsistent with those in the weakly hole-doped cuprates. While the decrease of intensity upon heating across T_C from 4 to 55 K is suggestive of a resonance, we do not see a spin gap. More temperature-dependence data is needed to clarify whether the change from 4 to 55 K is part of a broader trend that also explains the even lower intensity at 200 K.

4. We also looked at the elastic (or quasielastic) scattering intensity from $(0.5, 0.5, L)$, representing 2-dimensional magnetic correlations. In unannealed, non-superconducting $La_{1.9}Ca_{1.1}Cu_2O_{6+\delta}$ and weakly-doped $La_{2-x}Ba_xCuO_4$,

the intensity dropped quickly with increasing temperature, whereas in our annealed, superconducting $La_{1.9}Ca_{1.1}Cu_2O_{6+\delta}$ crystal, the intensity remained strong to higher temperatures. In weakly-doped $La_{2-x}Ba_xCuO_4$, the decrease in elastic intensity was accompanied by an increase in inelastic intensity at low energies [154], suggesting that the spins that were ordered at low temperatures became more free to move (but still having significant dynamic spin-spin correlations) at higher temperatures. A similar shift from elastic to inelastic scattering intensity is possible in our data, but our energy resolution was too broad to distinguish these two contributions.

5. Superstructure peaks are present which may indicate ordering due to interstitial oxygen. In oxygen-doped $La_2CuO_{4+\delta}$, there is evidence for phase separation at low temperatures due to the mobility of interstitial oxygen ions, so we may speculate that phase separation may be present in La-2126 as well.

We do not yet have an explanation which ties together all of these findings, but we can discuss possibilities. The main question is whether phase separation of interstitial oxygen ions plays a role, as it does in the related La-214 compounds $La_2CuO_{4+\delta}$ [12] and $La_{2-x}Sr_xCuO_{4+\delta}$ [157], though phase separation can be suppressed in the La-214 system as in $La_{2-x}Nd_xCuO_{4+\delta}$ and $La_{2-x}Bi_xCuO_{4+\delta}$ [158–160]. The presence of superstructure peaks, assuming they indicate interstitial-oxygen-related order, suggest that phase separation may be present in our crystal as in $La_2CuO_{4+\delta}$. If so, we might expect that the superconductivity arises from ordered, oxygen-rich regions, while the magnetic behavior associated with weakly-doped cuprates would arise from oxygen-poor regions. However, there are a number of issues that would need explanation. First, $La_2CuO_{4.045}$ was shown to have, at $\hbar\omega = 2$ meV, incommensurate peaks arising from superconducting regions as well as a commensurate peak arising from non-superconducting regions [12]. However, we see no sign of incommensurate magnetic excitations in our data. The incommensurate magnetic excitations may simply be too diffuse or be too close to the commensurate excitations to be distinguishable, but there would remain the question of how to explain the atypical temperature-dependence of the commensurate excitations.

A second possibility is that there is a single phase, with additional oxygen resulting in additional doping. Though this is not the behavior seen in $La_2CuO_{4+\delta}$, as mentioned above certain dopants appear to suppress phase

separation, and we might imagine that $La_{1.9}Ca_{1.1}Cu_2O_{6+\delta}$ is structurally different enough to also suppress phase separation. A single phase picture would provide a natural explanation for the variation in T_C found under different annealing treatments for the same nominal composition.

Either way, we would still have to reconcile the presence of commensurate magnetic excitations with superconductivity. Although an hourglass dispersion has been seen in the magnetic excitations of superconducting La-214, YBCO, and BSCCO compounds [11], exceptions do exist, such as for underdoped $HgBa_2CuO_{4+\delta}$ [155], though the magnetic excitations in annealed $La_{1.9}Ca_{1.1}Cu_2O_{6+\delta}$ appear much different from those in underdoped $HgBa_2CuO_{4+\delta}$. We do not yet have an explanation for the temperature-dependence of the magnetic excitations. The temperature-dependence may be associated with superconductivity, but many superconducting hole-doped cuprates have a temperature-dependence in the form of a resonance peak (broad or sharp) and a spin gap, and we do not see such clear features. Data for more temperatures (especially around T_C), at higher energy transfers at $(0.5, 0.5, 3)$, or at better momentum- or energy-resolution may clarify many of these issues.

5.6 Summary

A single crystal of $La_{1.9}Ca_{1.1}Cu_2O_{6+\delta}$ made superconducting by high-pressure annealing in the presence of oxygen was measured by inelastic neutron scattering, and the magnetic excitations were found to be commensurate, unlike the incommensurate excitations seen in most other superconducting hole-doped cuprates. The temperature dependence of the intensity of these excitations consists of a decrease in intensity with temperature above 8 meV for $T = 4$, 55, and 200 K; this decrease is much different from the temperature-dependence of the magnetic excitations in weakly hole-doped cuprates. Further research is needed to clarify the relationship between magnetic excitations and superconductivity in $La_{2-x}Ca_{1+x}Cu_2O_{6+\delta}$, especially the possible role of phase separation involving interstitial oxygen.

6 Phonon coupling to dynamic short-range polar order in the relaxor ferroelectric $\mathbf{Pb(Mg_{1/3}Nb_{2/3})_{0.68}Ti_{0.32}O_3}$

In this Section, I present our neutron scattering research on the relaxor ferroelectric 68% $PbMg_{1/3}Nb_{2/3}O_3$-32% $PbTiO_3$. The first subsection is an overview of relaxor ferroelectrics as they pertain to this research. The rest of this section is mostly reprinted from Ref. [161]. Copyright is held by the American Physical Society. The coauthors include myself, Zhijun Xu of U. C. Berkeley, Barry Winn of Oak Ridge National Laboratory, Chris Stock of the University of Edinburgh, Peter Gehring at the National Institute of Standards and Technology, Robert Birgeneau of U. C. Berkeley, and Guangyong Xu of Brookhaven National Laboratory.

6.1 Overview of relaxor ferroelectrics and short-range order

Relaxor ferroelectrics have been studied due to interest in their potential dielectric and piezoelectric applications [16, 162, 163], and due to interest in how the properties of dielectric and ferroelectric materials change in the presence of charge or electric dipole disorder. In this subsection I will give a brief overview of relaxor ferroelectric properties and the system $(1-x)$PMN-xPT ($Pb(Mg_{1/3}Nb_{2/3})_{1-x}Ti_xO_3$) which exhibits these properties for a range of compositions.

A conventional ferroelectric crystal is a crystal that has a net electric dipole moment in the absence of applied electric field, whose dipole moment can be flipped by application of a sufficiently strong electric field [164]. In ferroelectric crystals, there is long-range "polar order", i.e., the crystal structure is such that the "natural" primitive unit cell has a nonzero electric dipole moment [165]. Conventional ferroelectrics show a well-defined ferroelectric transition from a high-temperature unpolarized paraelectric state into an ordered polarized state below a Curie temperature T_C. Signals of this transition can be seen in properties such as the real part of the dielectric function, $\epsilon'(\omega)$, which peaks sharply at T_C for low frequencies [166]. Relaxor ferroelectrics, on the other hand, typically show a broad peak in $\epsilon'(\omega)$ as a function of temperature at low frequencies, and, in contrast to conventional ferroelectrics, the temperature of the peak's maximum intensity does

not correspond to a phase transition. Furthermore, at audio frequencies, the temperature at which $\epsilon'(\omega)$ is maximum is frequency-independent in conventional ferroelectrics, whereas this temperature has a substantial "frequency dispersion" in relaxors.

Relaxors are associated with a large degree of chemical disorder and inhomogeneity, but it may be instructive to first look at simpler systems such as homogeneous dielectric materials with dipole impurities. Dipole impurities can be introduced by certain element substitutions; for example, if the larger K^+ ion in KCl is replaced with the smaller Li^+ ion, the Li^+ can occupy a number of off-center positions, producing a dipole moment. For ordinary dielectric materials, the interaction between these dipole impurities results in a dipolar glass state at low temperatures [166]. For highly polarizable dielectric materials, impurity dipoles polarize surrounding regions creating polar nanoregions (PNRs), and the effects are less trivial. For example, the incipient ferroelectrics $SrTiO_3$ and $KTaO_3$, which are perovskites with the formula ABO_3 (see Fig. 32), are highly polarizable at low temperature due to having a soft mode frequency that goes to zero as the temperature goes to zero [166]. In doped incipient ferroelectrics such as $K_{1-x}Li_xTaO_3$, a dielectric function $\epsilon'(\omega)$ with frequency dispersion similar to that in relaxors has been seen, except with the response being weaker and peaking at much lower temperature [166][19].

One of the most-studied systems with relaxor behavior is $(1-x)$PMN-xPT. This system has a perovskite crystal structure with Pb^{2+} on the A-site. The B-site is occupied by Mg^{2+}, Nb^{5+}, and Ti^{4+} which may be randomly or partially ordered, with "chemically ordered regions" and disordered regions having domain sizes that depend on composition and annealing conditions [170][20]. For pure PMN, a microstructure of chemically ordered and disordered

[19] A similar frequency dispersion is found in the magnetic susceptibility of spin glasses, which are materials where the interactions between magnetic moments are frustrated due to disorder [167].

[20] To be precise, in $Pb(Mg_{1/3}Nb_{2/3})O_3$ and similar compounds such as $Pb(Mg_{1/3}Ta_{2/3})O_3$ (PMT), this partial ordering consists of every other unit cell (in a sublattice of a NaCl-like structure) having the B-site occupied solely by Nb^{5+}, while the other unit cells have the B-site randomly occupied by Nb^{5+} and Mg^{2+} [170, 171]. Some samples have been made to consist almost entirely of partially-ordered domains, such as Zr-doped PMT [171] subjected to a certain annealing treatment; even with partial-ordering, the relaxor property of the frequency dispersion of $\epsilon'(\omega)$ persists. In contrast, $Pb(Sc_{0.5}Ta_{0.5})O_3$ (PST) can, with a certain annealing treatment, have complete ordering on the B-site, in which case the frequency dispersion of $\epsilon'(\omega)$ seen in disordered

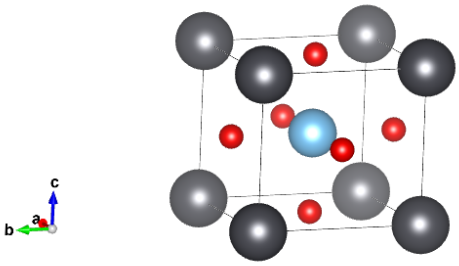

Figure 32: Unit cell for perovskite crystal structures with formulas ABO_3. Corner spheres are on the A-site, the center sphere is on the B-site, and the small spheres on the faces are the oxygen atoms. Image generated by the software VESTA [117].

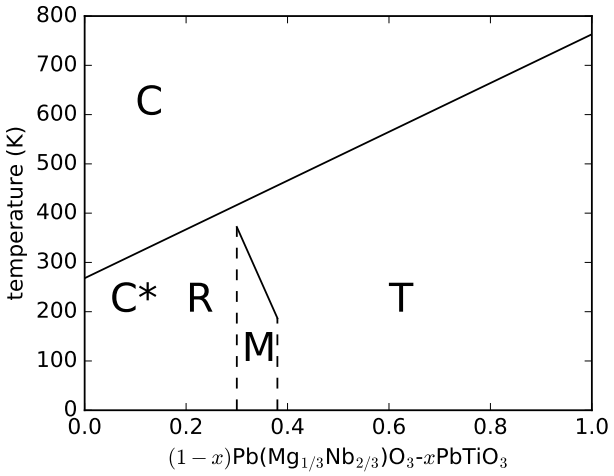

Figure 33: Schematic phase diagram of $(1-x)\mathrm{Pb}(\mathrm{Mg}_{1/3}\mathrm{Nb}_{2/3})\mathrm{O}_3$-$x\mathrm{PbTiO}_3$, based off of phase diagrams generated from x-ray diffraction and dielectric function measurements [168, 169]. "C", "R", "M", and "T" stand for "cubic", "rhombohedral", "monoclinic", and "tetragonal" symmetries, respectively. "C*" is the low-x phase believed to be cubic but whose precise nature is the subject of controversy.

regions has been reported with ordered domains of size ∼2-3 nm [170, 173]; the microstructure cannot be altered by annealing treatments [170]. Doping with Ti appears to shrink the size of chemically ordered regions [174]. Despite the complicated chemical order/disorder microstructure in $(1-x)$PMN-xPT, this microstructure should not change in the temperature range of our neutron scattering experiments in this Section since the ions are immobile in this range [170]. Thus, changes in short-range order shown in neutron scattering experiments below, say, 1000 °C can be attributed to correlated displacements of ions from their equilibrium positions, as explained below.

A rough schematic diagram for $(1-x)$PMN-xPT is shown in Fig. 33. The material has the same pseudocubic crystal structure throughout, with distortions from the high-temperature cubic symmetry into other symmetries in various regions of the phase diagram. The precise symmetry in many regions of the phase diagram has been the subject of controversy. For the morphotropic phase boundary region labeled by "M"[21], several monoclinic and orthorhombic phases have been proposed, and the phase observed may be dependent on whether and how electric field is applied [176]. Though the piezoelectric coefficient d_{33} maximizes in this region [14], the same maximization of piezoelectric properties at a morphotropic phase boundary has been observed in $Pb(Zr_{1-x}Ti_x)O_3$ [177, 178], which does not exhibit relaxor properties such as the frequency dispersion of $\epsilon'(\omega)$. Though there seems to be a connection between having high piezoelectric coefficients and having a morphotropic phase boundary region with lower symmetry phase(s), there is the continuing question of why relaxor systems such as $(1-x)$PMN-xPT have such exceptionally high piezoelectric coefficients [179].

Another example of the structural complexity of the relaxors is the "skin effect": For the "C*" region, experiments with less penetrating structural probes such as lower-energy (e.g., 10.7 keV) X-rays observe a rhombohedral phase while more penetrating probes such as neutrons or higher-energy (e.g., 67 keV) X-rays show a cubic phase [15]. This cubic phase has been the subject of much study and is sometimes called "phase X" [15]. The boundary between a clear rhombohedral bulk phase and an apparently cubic phase may be within $0.2 \leq x \leq 0.27$ [180]. For zero field, the crystal structure

PST is no longer present [172].

[21] A morphotropic phase boundary is a phase boundary crossed by changes in composition or pressure [175]. In this case the phase boundary is not a simple boundary between two phases but a transition region with lower-symmetry phases whose precise nature is still the subject of research.

can be described by the same cubic space group at all temperatures, but with evidence for increasing displacements of Pb ions from their equilibrium positions upon cooling [176]. For $x > 0$, there are signs of a structural phase transition between the high-temperature cubic and "C*" phases, such as broadening of a Bragg peak or an increase in lattice strain [15]. For $x = 0$, a ferroelectric transition around $T_C = 217$ K can be seen, but only if cooled through T_C in the present of a sufficiently large dc electric field [181].

In the low x, low temperature region, the system exhibits relaxor properties that disappear after we increase x beyond the morphotropic phase boundary region. One example is the frequency dispersion of $\epsilon'(\omega)$ [182], but there is also short-range polar order measured by X-ray and neutron scattering that is unique to the relaxor region of the phase diagram [183]. Short-range order refers to static or quasi-static correlations in the positions of nuclei that decay as the distance between nuclei goes to infinity, as opposed to long-range order, in which correlations are nonzero for displacements corresponding to a lattice vector even at large distances, and zero for non-lattice vector displacements. Neutron and X-ray scattering can measure these short-range correlations, which take the form of "diffuse scattering", i.e., intensity at wavevectors surrounding reciprocal lattice vectors[22].

Numerous experiments on the relaxors have shown evidence of short-range order below a certain temperature, often explained in terms of "polar nano-regions" (PNRs). PNRs are small regions polarized in random directions that were first proposed to explain a deviation from linearity in the optical index of refraction vs. temperature at the "Burn's temperature" $T_d \approx 620$ K in PMN [18, 184]. Neutron diffuse scattering has shown an onset of short-range order below T_d, and also weaker short-range order that persists up to at least 900 K and is probably due to the chemical ordering previously discussed [185]. Because the short-range order that appears below T_d is assumed to be related to the PNRs, it is referred to as "short-range polar order"[23]. Neutron scattering measurements with high energy resolution have

[22]Since the Bragg peak is expected to already have some width due to the resolution of the instrument, the Bragg peak is often fitted with a Gaussian function so that the remaining intensity above the background can be determined to be the diffuse scattering. Another source for confusion is that, for X-rays, "diffuse scattering" can refer to "thermal diffuse scattering", which is intensity arising from phonons.

[23]To be more precise, any short-range order arising from displacements of ions from their equilibrium crystallographic positions can be decomposed, for each wavevector $\mathbf{q}$ away from the Brillouin zone center, into displacements of the center-of-mass and displacements

been able to show that the diffuse scattering is not entirely elastic, i.e., that there are correlations between different times for the ionic shifts contributing to the short-range polar order [17]. Thus, we say that the short-range polar order is "dynamic" rather than static.

The short-range order associated with relaxors appears to depend on the presence of strong random electric fields due to the random substitution of ions of different valences on a crystallographic site. Evidence for this conclusion comes from a comparison of the neutron diffuse scattering from four different perovskite compounds, specifically, $K_{1-x}Li_xTaO_3$ and $KTa_{1-x}Nb_xO_3$ with same-valence substitution, and $Pb(Mg_{1/3}Nb_{2/3})O_3$ and $(Na_{1/2}Bi_{1/2})TiO_3$ with different-valence substitution [188]. A similar conclusion was reached when comparing the diffuse scattering from $(1-x)$PMN-xPT and the same-valence substituted $Pb(Zr_{1-x}Ti_x)O_3$ [189]. Although there have been numerous theoretical studies on the role of random fields in various systems, there is still not a good understanding of how these theories relate to relaxor properties [176].

Studying the relationship between the short-range polar order and the lattice vibrations can give insight into structural properties. One example is the relationship between elastic constants and acoustic phonon velocities along certain directions. Ideally, if the behavior of the acoustic phonon properties could be better understood, then one might understand how the inhomogeneity in the material affects elastic or piezoelectric properties. Thus, there have been a number of studies focusing on the relationship between the phonons and the short-range polar order [19, 190]. Some quantitative models for coupling between two phonon modes and between short-range-order (as seen by diffuse scattering) and a phonon mode have been used. In Ref. [190], phonon spectra of PMN obtained in different Brillouin zones were compared and fitted to models of these two types of coupling. The phonon-phonon coupling model assumed that the lattice vibrations at a certain wavevector had a lineshape (neutron scattering intensity as a function of energy transfer) corresponding to the response of two coupled, damped harmonic oscillators

of atoms relative to each other. This decomposition is analogous to decomposing phonon polarization vectors at $\mathbf{q} \neq \mathbf{0}$ into those of the acoustic and optic modes at $\mathbf{q} = \mathbf{0}$ (e.g., as done in Ref. [186]), where the acoustic mode components correspond to the center-of-mass shift component and the "short-range polar order" arises from components analogous to the optic mode components. It should be noted, however, that a center-of-mass shift component has been observed in the diffuse scattering of PMN in addition to the center-of-mass preserving component [187].

driven at a certain frequency. The diffuse scattering-phonon coupling model assumed the lineshape had a functional form derived from a formalism for crystals with orientational disorder [191]. The authors in Ref. [190] found that there was little evidence of phonon-phonon coupling, whereas changes in both acoustic phonon lineshapes and diffuse scattering intensity between different Brillouin zones indicated strong diffuse scattering-phonon coupling. Evidence for diffuse scattering-phonon coupling was also found in the similar relaxor $0.955Pb(Zn_{1/3}Nb_{2/3})O_3$-$0.045PbTiO_3$, where changes in both the diffuse scattering and acoustic phonons were seen under electric-field-cooled conditions as compared to zero-field-cooled conditions [19].

Below, we extend the study of the relationship between short-range polar order and phonon properties on another relaxor, 0.68PMN-0.32PT, comparing changes in diffuse scattering under field-cooled and zero-field-cooled conditions. Compared to the similar study with applied electric field [19], there are a couple essential differences. First, field was applied along a different direction, [001], such that the field was unlikely to simply shift the size of ferroelectric domains polarized along different directions. In contrast, the field in Ref. [19] was aligned along [111], and a corresponding shift in diffuse scattering components was seen in that study rather than the simple suppression seen in our data below. Second, we focused on phonons at wavevectors along a different high-symmetry direction, specifically, along the $\langle 100 \rangle$ directions rather than the $\langle 110 \rangle$ directions. The diffuse scattering in lead-based relaxors such as $(1-x)$PMN-xPT is anisotropic, extend much further along the $\langle 110 \rangle$ directions than the $\langle 100 \rangle$ directions in a butterfly-like pattern [17]. Rather than focusing on the butterfly wings of the diffuse scattering, we look at diffuse scattering and phonons along the $\langle 100 \rangle$ to have a more complete view of the relation between the phonons and diffuse scattering. We see evidence for a coupling between the short-range polar order and transverse acoustic and optic phonons, with notable differences from the similar phonon-diffuse scattering coupling previously investigated [19], and we describe our work in detail below.

6.2 Abstract

We report neutron inelastic scattering experiments on single crystal $PbMg_{1/3}Nb_{2/3}O_3$ doped with 32% $PbTiO_3$, a relaxor ferroelectric that lies close to the morphotropic phase boundary. When cooled under an electric field $\mathbf{E} \parallel [001]$ into tetragonal and monoclinic phases, the scattering cross section from transverse acoustic (TA) phonons polarized parallel to $\mathbf{E}$ weakens and shifts to higher energy relative to that under zero-field-cooled conditions. Likewise, the scattering cross section from transverse optic (TO) phonons polarized parallel to $\mathbf{E}$ weakens for energy transfers $4 \leq \hbar\omega \leq 9$ meV. However, TA and TO phonons polarized perpendicular to $\mathbf{E}$ show no change. This anisotropic field response is similar to that of the diffuse scattering cross section, which, as previously reported, is suppressed when polarized parallel to $\mathbf{E}$, but not when polarized perpendicular to $\mathbf{E}$. Our findings suggest that the lattice dynamics and dynamic short-range polar correlations that give rise to the diffuse scattering are coupled.

6.3 Introduction

Relaxor ferroelectrics have great potential for applications due to their piezoelectric and dielectric properties [16, 162, 163], but there is much that is not understood about how their properties arise on a microscopic level [15]. The composition of many relaxors is related to simple perovskites with the ABO_3 formula, but with one cation site randomly filled with two or more cations of different valences, resulting in strong, disordered electric fields. For the relaxor $PbMg_{1/3}Nb_{2/3}O_3$ (PMN), the B^{4+} site is occupied by Mg^{2+} and Nb^{5+}. The variation in valence can be reduced by doping with an ion of intermediate valence, e.g., Ti^{4+} in the case of PMN doped with x fraction of $PbTiO_3$ ($(1-x)$PMN-xPT). The resulting $(1-x)$PMN-xPT phase diagram shows four basic regions [168, 178, 192]: a cubic paraelectric phase at high temperature for all x; a region with relaxor behavior for low x with either cubic or rhombohedral symmetry; a tetragonal, conventional ferroelectric region for high x; and a morphotropic phase boundary (MPB) region between the relaxor and tetragonal regions. The piezoelectric coefficients d_{33} are very large in the MPB region and abruptly drop for higher x [14, 16, 193, 194]; understanding this behavior and exploiting the large piezoelectricity provide much of the motivation for exploring relaxor ferroelectrics. These $(1-x)$PMN-xPT solid solutions with small x exhibit clear relaxor behavior characterized

by large dielectric constants which have a broad maximum with respect to temperature and are highly frequency-dispersive within this range. These relaxor behaviors are widely believed to be associated with polar nano-regions (PNR) or other short-range polar order, as shown by numerous X-ray and neutron diffuse scattering studies [17, 187, 195–205].

We have previously characterized two distinct components of the diffuse scattering in $(1-x)$PMN-xPT, which we label T1 and T2 [206] as shown in Fig. 34(a). These labels are intended to refer to the related phonons where a T1 mode is a transversely polarized phonon propagating along $\langle 100 \rangle$ and a T2 mode is a transversely polarized phonon propagating along $\langle 110 \rangle$. For example, near (100), a TA_1 phonon mode would refer to the transverse acoustic phonon mode propagating along the [010] or [001] directions with polarization along [100], while near (110), a TA_2 phonon mode would refer to the transverse acoustic phonon mode propagating along $[1\bar{1}0]$ with [110] polarization.

The two diffuse scattering components can be distinguished by their anisotropic responses when field-cooled (FC), i.e., after applying electric field above the ferroelectric transition temperature T_C and then cooling below T_C. With a field applied along [111], a redistribution of T2-diffuse scattering intensity between two differently-oriented components polarized along [110] and $[1\bar{1}0]$ has been observed in the structurally similar perovskite $Pb(Zn_{1/3}Nb_{2/3})_{1-x}Ti_xO_3$ ($(1-x)$PZN-xPT) [207–209] and in PMN [210]. This situation has been interpreted in terms of a domain effect, in which applying a [111] field creates a single [111]-polarized ferroelectric domain (as opposed to the eight possible $\langle 111 \rangle$-polarized domains present in the zero-field cooled state) that favors certain orientations of polar nanoregions (PNR), resulting in the redistribution of diffuse scattering intensities along certain $\langle 110 \rangle$ directions [209]. An electric field along [001], on the other hand, does not seem to significantly affect the T2-diffuse scattering in the $H0L$ plane [211]. A [001] field does, however, affect the T1-diffuse scattering, but the T1-diffuse scattering does not show a redistribution of scattering intensity under an external field. Instead, a suppression of [001]-polarized T1-diffuse scattering occurs under [001]-field cooling, while the [100]-polarized T1-diffuse scattering remains unaffected, as has been shown in $(1-x)$PZN-xPT [206, 212]. This behavior is not due to a domain effect; otherwise, we would expect the intensity and other characteristics of the T1-diffuse scattering near [001] under zero-field-cooling (ZFC) to be in between those near [001] and [100] under FC conditions. Thus, the changes induced by a [001]

field should be due to changes within domains rather than changes in the sizes of domains, in contrast to applying a [111] field.

Ultimately, we would like to know how the local structures that give rise to the diffuse scattering affect bulk properties. When these local structures are intriniscally altered by, say, application of electric field, changes in the bulk structure would reveal connections between bulk and local structures. Phonons provide important measures of the dynamic properties of the bulk lattice, and their couplings to the diffuse scattering are therefore one of the key issues to pursue in understanding relaxor properties. For example, transverse acoustic phonons propagating along $\langle 110 \rangle$ (TA_2-phonons) are expected to couple with T2-diffuse scattering modes [190]. Evidence for this diffuse-TA_2 phonon coupling has been shown with the help of an external [111] electric field, which breaks the pseudo-cubic symmetry and reveals a clear difference between TA_2 phonons measured near (220) and $(2\bar{2}0)$ [19]. It would be interesting to see if there is a similar coupling between phonons and diffuse scattering along the T1 directions under a [001] field, given that the effect of a [001] field is not a domain effect like that of a [111] field, but coupling between the T1-diffuse modes and the TA_1 or TO_1 phonon modes has not yet been thoroughly studied.

In this Section we report neutron scattering experiments on 0.68PMN-0.32PT with a field applied along [001]. When cooled below $T_C \approx 430$ K [211], in addition to the expected suppression of T1-diffuse scattering measured near (001), we also see a clear change in the intensities of the TA_1 phonons near (001), whereas the TA_1 phonons near (100) are unaffected. These changes illustrate that there may be a TA_1-phonon/T1-diffuse mode coupling, evocative of the TA_2-phonon/T2-diffuse mode coupling previously seen in PZN-4.5%PT [19]. This coupling appears to be limited to large-wavelength phonons. In addition, we observed a suppression of spectral weight for the transverse optic phonons in the T1 direction (TO_1 phonons) within 4 to 9 meV near (002), but no change was seen near (200). The changes in the TA_1 and TO_1 phonons were present at 400 K but much less pronounced at 200 K.

6.4 Experimental Details

We purchased a 0.68PMN-0.32PT single crystal from TRS Ceramics with dimensions $10 \times 10 \times 2$ mm^3 and large [001] faces. The (001) surfaces were coated with gold to ensure a uniform equipotential surface during the appli-

cation of a field $\mathbf{E} \parallel [001]$. Field was only applied during field cooling, and only along [001]. Another 0.68PMN-0.32PT crystal from the same source was measured to have a cubic-tetragonal transition at $T_C \approx 430$ K and a tetragonal-monoclinic transition near 355 K, both measured on cooling [211]. Neutron inelastic scattering experiments were performed on the HYSPEC time-of-flight spectrometer at the Spallation Neutron Source at Oak Ridge National Laboratory [152]. The software package Mantid was used in the processing of the data [213]. The incident energy E_i was set to 20 meV. The crystal symmetry was pseudocubic with lattice parameter $a = 4.00$ Å. All neutron scattering momentum transfers $\mathbf{Q}$ are reported in terms of reciprocal lattice units (r.l.u.), and energy transfers $\hbar\omega$ are reported in meV. Measurements were performed in the $H0L$ scattering plane. Fields of 0.5-8.0 kV/cm were used. The T1-diffuse scattering at (001) changed significantly with a field of 0.5 kV/cm, and had almost no additional change with higher field, indicating that 0.5 kV/cm was sufficient to alter the T1-polarized short-range order. For pseudocolor plots, the data were smoothed. Error bars represent statistical error and correspond to 1 standard deviation from the observed value.

6.5 Data and Analysis

In Fig. 34(b), the temperature dependence of the T1-diffuse scattering near (001) is shown with neutron scattering intensity measured at wavevector $\mathbf{Q} = (-0.125, 0, 1)$ for FC and ZFC conditions. For temperatures up through 400 K a clear suppression of intensity is seen with applied field, but this difference disappears above the ferroelectric transition between 400 and 450 K. In Figures 34(c) and 34(d) we show that the suppression of T1-diffuse scattering under FC conditions is direction-dependent, being absent for [100]-polarized diffuse scattering measured near (100) (Fig. 34(c)) but present for [001]-polarized diffuse scattering near (001) (Fig. 34(d)). These data were taken at 200 K as transverse scans across the Bragg peaks. The direction dependence of the suppression of T1-diffuse scattering under [001]-field cooling is consistent with previous reports on the related $(1-x)$PZN-xPT system [206, 212].

Fig. 35 shows the dispersions of the TA_1 phonons near (100) and (001) under FC and ZFC conditions, in which a change in intensity under field can be seen near (001) but not (100). These are pseudocolor plots of intensity vs. energy and momentum transfer in slices across (100) and (001) at 400

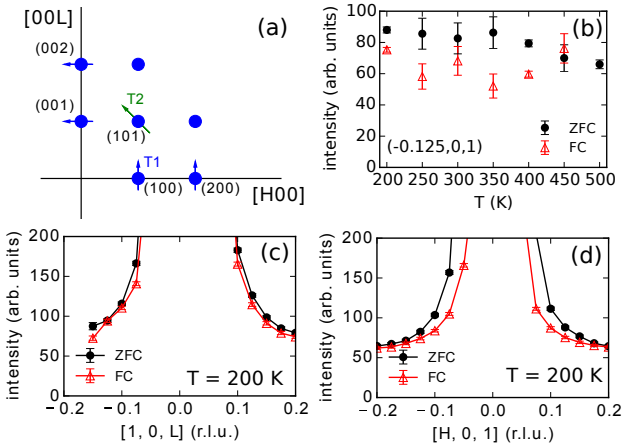

Figure 34: (a) Schematic diagram of the $H0L$ plane in reciprocal space. The blue and green arrows indicate the T1 and T2 directions, respectively. (b) Temperature dependence of T1-diffuse neutron scattering, shown via intensity at wavevector $\mathbf{Q} = (-0.125, 0, 1)$ and energy transfer $\hbar\omega = 0$ meV plotted as a function of temperature. The intensity was integrated within $0.95 \leq L \leq 1.05$ r.l.u., $-0.1375 \leq H \leq -0.1125$ r.l.u., and $-0.5 \leq \hbar\omega \leq 0.5$ meV. (c,d) Field-dependence of diffuse scattering near (100) and (001), shown from elastic neutron scattering intensity plotted along $[10L]$ and $[H01]$ at 200 K for zero-field-cooled (ZFC) and field-cooled (FC) conditions. Data were integrated within ± 0.5 meV for $\hbar\omega$, and ± 0.05 r.l.u. for the H and L directions for (c) and (d), respectively.

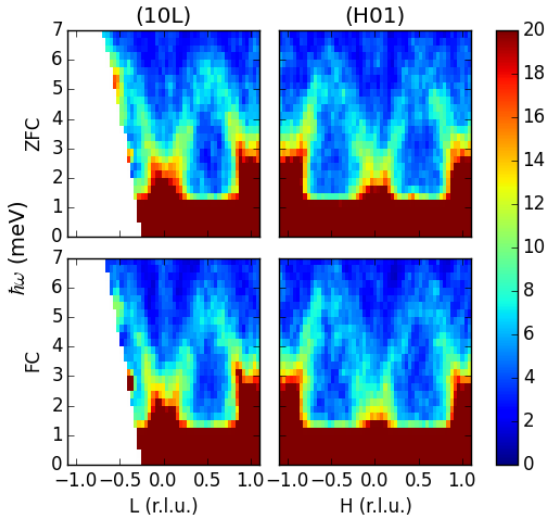

Figure 35: Pseudocolor plots of transverse acoustic phonons near (100) (left) and (001) (right), for ZFC (top) and FC (bottom) conditions. Neutron scattering intensity (indicated by color, in arbitrary units) is plotted against energy and momentum transfer. The intensities were averaged within ±0.05 r.l.u. along H for (10L) and L for (H01). These data were taken at 400 K. White areas represent lack of data.

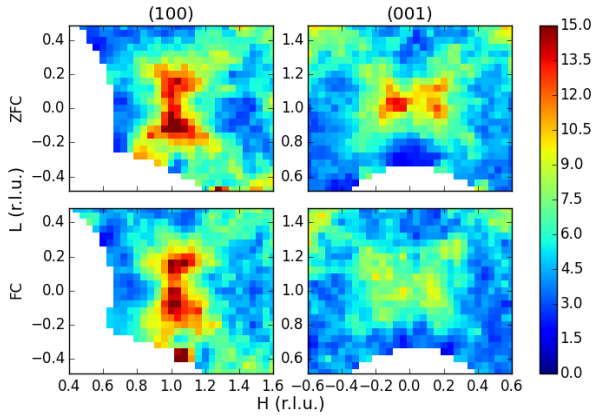

Figure 36: Pseudocolor plots of transverse acoustic phonons in the $H0L$ plane near (100) (left) and (001) (right), for ZFC (top) and FC (bottom) conditions, illustrating the suppression of phonon spectral weight with field near (001) but not (100). Neutron scattering intensity (indicated by color in arbitrary units) is plotted against energy and momentum transfer. These data were taken at 400 K and averaged within $1.5 \leq \hbar\omega < 2.5$ meV. White areas represent a lack of data.

K. The TA_1 phonons disperse out from the Bragg peaks and have maxima around roughly 5-6 meV. The width of the phonons with respect to energy is evident. The effect of field can be seen more clearly in Fig. 36, which shows the phonon intensities near (100) and (001) in a similar pseudocolor plot, but in the $H0L$ plane with $\hbar\omega$ fixed at 2 meV. There is a clear decrease in intensity with field near (001), but no clear change near (100).

For a clearer view of how the phonon dispersion is affected by field, in Fig. 37 we show intensity plotted as a function of $\hbar\omega$ for momenta at $(-q,0,1)$ and $(1,0,q)$ for various q values, taken at 400 K. We can see that there is little change near (100) for all q, but near (001) a clear change is seen, with both a suppression of intensity and an increase in energy transfer for $q = 0.1$ (and possibly also $q = 0.2$). These data suggest that the electric field effect is strongest for low q. We note that we have not seen a clear field effect on longitudinal acoustic (LA) phonons measured along [100] near (100) and along [001] near (001), or on TA2 phonons measured along $[\bar{1}01]$ near (101), suggesting that the [001]-field primarily affects T1-phonons. This situation is similar to how T1-diffuse scattering intensities respond to [001] fields, with T1-diffuse scattering suppressed near Bragg peaks with wavevector $\mathbf{G} \parallel [001]$ but unaffected for $\mathbf{G} \parallel [100]$ [206, 212], and similar to the lack of effect on the $(H0L)$ zone T2-diffuse scattering by a [001] field [211].

The transverse optic modes near (200) and (002) at 400 K are shown in Fig. 38. (Faint spectral weight from these modes were also seen near (100) and (001) but were too weak to clearly discern.) Each panel consists of a pseudocolor plot of the scattering intensity, with energy transfer plotted on the vertical axes and momentum transfer in the transverse direction across the Bragg peaks plotted on the horizontal axes. The dispersion exhibits the "waterfall effect" seen in other $(1-x)$PMN-xPT and $(1-x)$PZN-xPT compositions [214–221], where, at small q, the TO_1 phonon softens, approaches the TA_1 mode energies, and becomes highly damped. Unfortunately, this effect made it difficult to measure the TA_1 modes at small q near (200) or (002), and we could not discern changes with field.

Some suppression of spectral weight under FC conditions can be seen in Fig. 39, which shows pseudocolor plots of constant-energy slices at $\hbar\omega = 6$ meV and 400 K. Specifically, a slight decrease can be seen near (002) with field-cooling, but no change is clear near (200). For a clearer view of the spectral weight suppression, Fig. 40 shows constant-energy cuts made along the transverse directions across the (200) and (002) Bragg peaks. In each panel, scattering intensity is plotted against momentum transfer for data

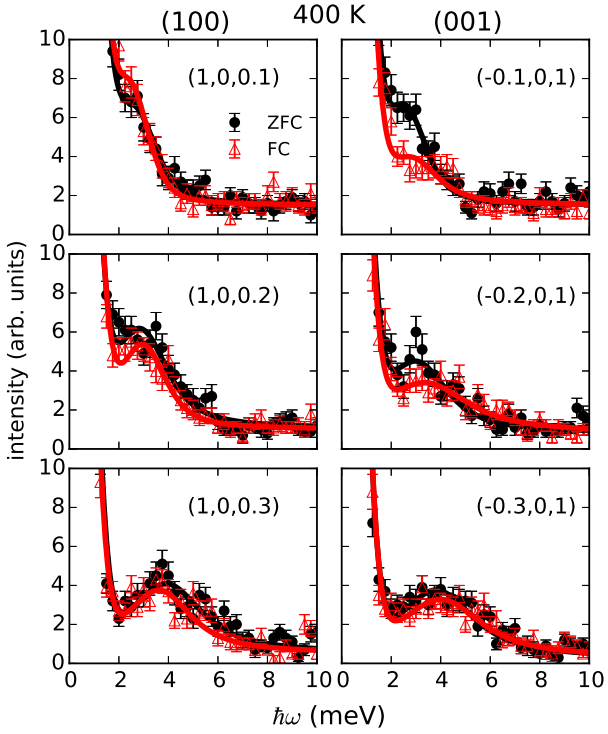

Figure 37: Constant-**Q** cuts of transverse acoustic phonon lineshapes, with neutron scattering intensity plotted against energy transfer $\hbar\omega$. Data were taken at 400 K. The data were averaged over ± 0.05 r.l.u. in both the H- and L-directions. The Brillouin zones in which the data were taken are displayed at the top of each column of subplots. ZFC data are represented by black circles, and FC data are represented by red triangles. The plotted lines are the result of fitting each data set to the sum of a Gaussian function for elastic scattering and Voigt functions for the acoustic phonons.

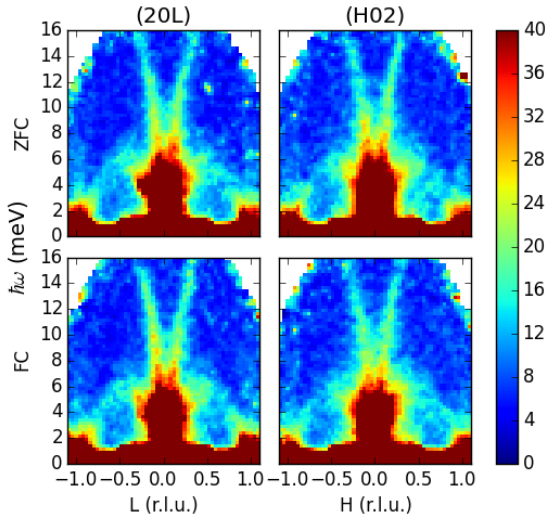

Figure 38: Pseudocolor plots illustrating the transverse optic modes near (200) (right) and (002) (left) for ZFC (top) and FC (bottom) conditions, with neutron scattering intensity plotted as color (in arbitrary units) as a function of energy and momentum transfer. The data were integrated within ± 0.1 r.l.u. along H for $(20L)$ and L for $(H02)$. White areas represent lack of data.

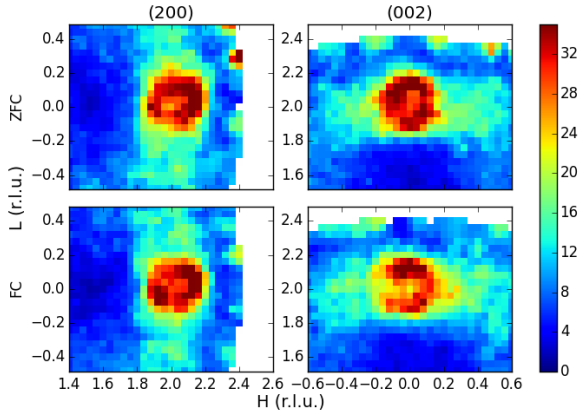

Figure 39: $H0L$ slices at 400 K and $5.5 \leq \hbar\omega \leq 6.5$ meV, focusing on the TO phonons near (200) and (002). These are pseudocolor plots, with intensity plotted as color (in arbitrary units), and momentum transfer along $(2, 0, L)$ and $(H, 0, 2)$ delimited on the axes. White areas represent lack of data.

taken under ZFC and FC conditions. We see that there is a consistent suppression of spectral weight near (002) but not near (200). This suppression can be seen from 4 to 9 meV; we note that the difference disappears outside of this range. As for the TO_1 phonon energy, it is difficult to observe changes in the TO_1 dispersions due to their steepness and to the phonons becoming highly damped at small q. For comparison, we note that in conventional ferroelectrics there have been examples of optic modes being affected by field [222, 223], and the effect is only predicted to be large for soft modes close to zero energy in the vicinity of a structural phase transition [224].

To illustrate the effect of temperature, in Fig. 41 we show representive data of the TA_1 and TO_1 modes at 200 K to contrast with the 400 K data in Figures 37 and 40, respectively. In Fig. 41(a), we show a constant-$\mathbf{Q}$ cut showing the TA_1 mode at $(-0.1, 0, 1)$. In Fig. 41(b), we show a constant-$\hbar\omega$ cut at 8 meV showing the TO_1 mode. In both plots, we see a similar suppression of intensity near (001) and (002). We also saw a similar lack of change near (200) (not plotted), but near (100) a spurious feature prevented us from determining if there was a change in TA_1 phonon spectral weight. From these data, we can see that the field effect at 200 K seems to be less

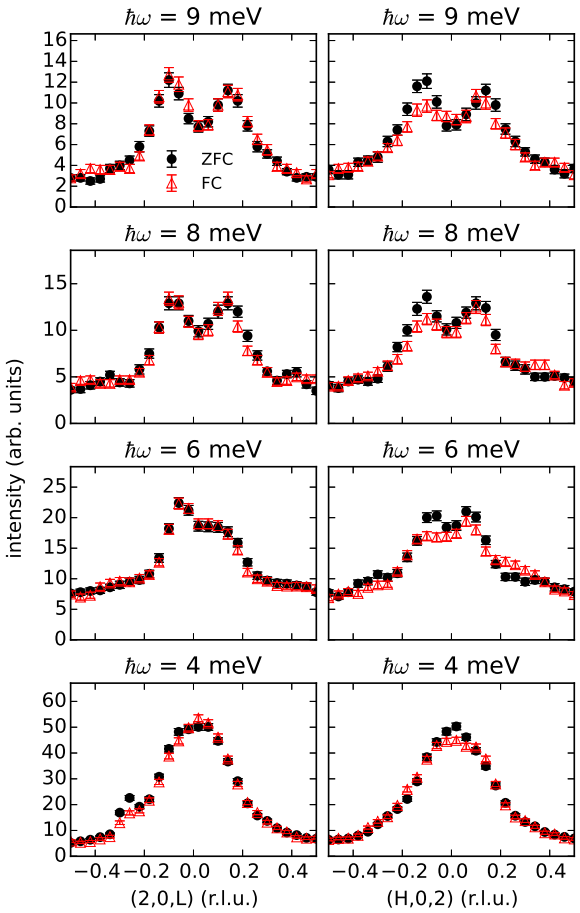

Figure 40: Constant-energy cuts across the transverse optic modes along $(20L)$ (right) and $(H02)$ (left) for $\hbar\omega = 4$, 6, 8, and 9 meV, integrated over $1.9 \leq H \leq 2.1$ for (20L) and $1.9 \leq L \leq 2.1$ for (H02), and within an energy range of ± 0.5 meV. For each subplot, neutron scattering intensity is plotted against momentum transfer. All data were taken at 400 K.

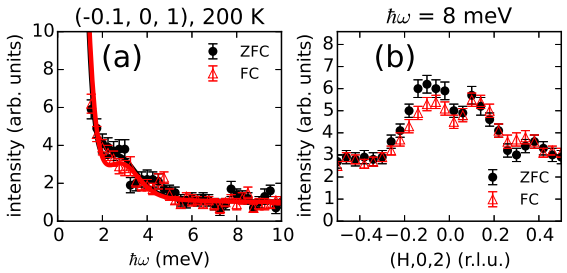

Figure 41: Neutron scattering scans at 200 K showing less change between ZFC and FC conditions near (001) and (002) than in the 400 K data in Figures 37 and 40. (a) Constant-**Q** scan at $(-0.1, 0, 1)$, with intensity plotted against energy transfer. Data were integrated within ± 0.05 r.l.u. in the H and L directions. (b) Constant-$\hbar\omega$ scan at $\hbar\omega = 8$ meV, with intensity plotted against momentum transfer. Data were integrated within $7.5 \leq \hbar\omega \leq 8.5$ meV and $1.9 \leq L \leq 2.1$ r.l.u.

pronounced than that at 400 K, at least for the acoustic phonon mode.

6.6 Discussion

The electric field effects observed in our measurements can be summarized as (i) there is no [001] field effect on the longitudinal acoustic (LA) modes, or on the transverse acoustic modes propagating along the $\langle 110 \rangle$ (TA_2) directions; (ii) for TA_1 phonons polarized along $\langle 001 \rangle$, we observed, after field-cooling, a reduction of intensity and increase of phonon energy near Bragg peak wavevectors **G** $\parallel$ [001], but no field effect was observed for TA_1 modes near **G** $\parallel$ [100]. For diffuse scattering, a similar pattern in response to field-cooling along [001] has been seen, with intensity suppression for **G** $\parallel$ [001], but not for **G** $\parallel$ [100] [206, 212]. A much smaller effect on low energy TO modes is also observed following the same rule, i.e., a reduction of intensity near the bottom of the TO mode measured for **G** $\parallel$ [001], but no effect for **G** $\parallel$ [100]. These results imply that a coupling exists between the diffuse scattering along $\langle 001 \rangle$ (the T1-diffuse scattering) and the TA_1 and/or TO_1 phonon modes along the same directions.

Previous work has shown a strong coupling between the diffuse scattering along the $\langle 110 \rangle$ directions (the T2-diffuse scattering) and the TA_2 phonon modes in these lead-based relaxor materials [19]. The diffuse-phonon cou-

pling along the $\langle 001 \rangle$ (T1) and $\langle 110 \rangle$ (T2) directions share some common features. For example, when the diffuse scattering is suppressed by the external field, we always see a hardening of the corresponding TA phonon mode, suggesting that interaction between the PNR and the phonons tends to drive the phonons softer, for both the T1 and T2 modes. This tendency suggests that short-range polar order is likely related to lattice instabilities in these relaxor compounds.

On the other hand, the T1 and T2 modes differ in many aspects too:

(i) For the case of the T2 modes, the field effect on the PNR (and thus on the T2-diffuse scattering) is indirect. An external field along [111] helps establish a single domain ferroelectric phase with [111] polarization. The change in the population of each domain induces a redistribution of PNR with different polarizations, resulting in the redistribution of T2-diffuse scattering intensities in reciprocal space. For example, under a [111] field there is an enhancement of the T2-diffuse scattering near the (220) Bragg peak, but a reduction of the T2-diffuse scattering near the $(\bar{2}20)$ Bragg peak. The TA_2 phonon near (220) softens, while the phonon near $(\bar{2}20)$ hardens. On the other hand, in zero field, all $\langle 111 \rangle$ domains are present to an equal degree. Measurements in zero field of the TA_2 phonons near (220) or $(\bar{2}20)$ average over both hardened and softened phonons, and the role of the [111] field is merely to obtain results for a single domain.

However, the [001] field effects on the T1-diffuse scattering and T1-phonons are not domain related. This can be demonstrated by comparing the ZFC and FC results. Under FC conditions, one only sees changes (relative to the ZFC results) for $\mathbf{G} \parallel [001]$, but no change for $\mathbf{G} \parallel [100]$. If these changes were due to domain effects, one would have expected the ZFC results to lie in between (in intensity, energy, etc.) the FC results measured for $\mathbf{G} \parallel [100]$ and [001]. This is not the case. Therefore, the effect of the [001] field is more intrinsic, with the field directly affecting the short-range order and consequently the related phonon modes.

(ii) While there is no evidence of diffuse-TO coupling for the T2 modes [19], in our sample there appears to be a weak diffuse-TO coupling for $\mathbf{G} \parallel \langle 001 \rangle$ (TO_1 modes).

(iii) The diffuse-phonon coupling for the T2 modes is strong throughout the entire Brillouin zone, but the coupling for the T1 modes is only present for a small range of q values ($\sim$0.1 to 0.2 r.l.u.) away from $\mathbf{G}$. This anisotropy of the diffuse-TA coupling revealed by our electric field measurements is also consistent with previous reports [225].

In order to understand these results, we consider the origin of the diffuse scattering and short-range orders in relaxors. The local random electric field generated by the B-site cations are believed to play important roles in Pb-based relaxor systems [176, 226–230]. A direct link between the diffuse scattering in these relaxors and the random field has been demonstrated by comparing two isostructures with and without random B-site valences [189]. The random field in the system prevents long-range order from developing and induces short-range orders that also grow with cooling.

The diffuse scattering intensities are not entirely static, and have a strong dynamic component [206, 231, 232], which is consistent with our results. Indeed, in our work, the coupling between the T1-diffuse scattering and the TA_1 phonon appeared weaker at 200 K than 400 K, where the dynamic component has also been shown to decrease with cooling [231, 232] below T_C. The existence of these dynamic/quasi-elastic components has been explained by theoretical work [233, 234], and is essential for the coupling between the diffuse scattering and phonons.

The weak coupling of the T1-diffuse scattering to the TO_1 mode can be understood from the fact that the short-range orders consist of a combination of acoustic (strain) and optic (polar) types of atomic shifts [206, 208]. The polar component of the short-range order can couple to the TO mode, and is also essential for the short-range order to respond to an external field. The coupling will likely diminish quickly when the TO phonon energy increases and moves further away from the quasi-elastic component of the diffuse scattering, as is the case in our measurements. A more detailed understanding of the competing interactions on a microscopic level, such as the role of the Pb-O bond, whose covalent nature is said to be responsible for ferroelectricity in $PbTiO_3$[235], would be desired, but is beyond the scope of this paper.

The anisotropy of the diffuse-phonon coupling between the T1 and T2 directions is more intriguing. The T2-diffuse scattering is significantly stronger than the T1-diffuse scattering, extends to a larger q-range in reciprocal space, and interacts with TA phonons along almost the entire branch. Overall, we could consider a picture where each PNR is actually a "core" of a region of short-range correlated $\langle 110 \rangle$ atomic shifts, contributing to the broader T2-diffuse scattering; whereas the polar/strain field surrounding the core extends to a much greater range, and contributes to the narrower T1-diffuse scattering. (These core regions, being the PNRs, should not be confused with the virtually temperature-independent chemical disorder/short-range order that persists up to at least 900 K [185]; the PNRs are local polar structures that

Table 2: C_{44} and $(C_{11}-C_{12})/2$ elastic constant data from neutron scattering experiments in units of 10^{11}N/m^2. 0.68PMN-0.32PT values calculated from data taken at 400 K; all other values calculated from data at 300 K.

Material	C_{44}	$(C_{11}-C_{12})/2$
PMN [225]	0.53(3)	0.48(6)
0.68PMN-0.32PT	0.56(5)	0.23(4)
0.955PZN-0.045PT [19]		0.26(4)
$PbTiO_3$ [245]	0.72(2)	0.63(1)

appear at the Burn's temperature T_d and grow with cooling.) The atomic shifts within the PNRs would be significantly larger than those in the surrounding region, leading to a much stronger T2-diffuse scattering than the weaker T1-diffuse scattering. The core of the short-range order, the PNRs, result from the local strong random field and cannot be directly suppressed by an external field [19, 208, 209]. However, the weaker polar/strain field around the core is less robust and can be partially modified by external field, showing the intrinsic field effect on the T1-diffuse scattering and its coupling to TA_1 and TO_1 phonon modes discussed in this paper.

An analog to this situation has recently been considered [236, 237] where strong but dilute random fields are inserted into a system with a weak continous random field. Theoretical work involving a magnetic system with a random field [237] suggested that a large correlation length or even a weak long-range order could be achieved. If we map the PNRs to the strong random field in the magnetic system, the large spin correlation length proposed by the theoretical work can be related to the weak polar/strain field surrounding the PNRs which gives the T1-diffuse scattering. Although not an exact analog, this picture does provide a crude description of the origin of the two types of diffuse scattering. For a better understanding of the source of these diffuse scattering components and their coupling to lattice dynamics, more detailed experimental work is required. Though numerous models have been proposed by various groups attempting to describe the diffuse scattering and short-range orders in these relaxor systems [198, 204, 238–244], our results simply suggest that there is a clear anisotropy in the diffuse scattering, their field dependence, and their coupling to the related phonon modes measured along $\langle 100 \rangle$ and $\langle 101 \rangle$ directions.

We can compare elastic constants derived from the TA_1 and TA_2 phonon energies in our data with values reported for similar materials to get insight into the tendency for lattice instability in the T1 and T2 directions. Our values and those for related compounds in the literature are displayed in Table 2. From our data, we obtained the elastic constant quantities $C_{44} = 0.56(5)$ and $(C_{11} - C_{12})/2 = 0.23(4)$ in units of 10^{11} N/m^2 based on the TA_1 and TA_2 phonons measured near (001) and (101) at $T = 400$ K. The value of C_{44} is slightly larger than in PMN but smaller than in $PbTiO_3$ [225]. $(C_{11} - C_{12})/2 = 0.23(4)$ shows a bigger change, being significantly reduced from its value in PMN, suggesting an increased lattice instability when the system approaches the morphotropic phase boundary. In fact, a similar value of $(C_{11} - C_{12})/2 = 0.26(4)$ can be obtained from phonon data on PZN-4.5%PT [19].

The diffuse-phonon coupling discussed in this paper can also affect how one determines the elastic constants. We calculated the phonon velocities from our FC data rather than our ZFC data since we believe the FC velocities more closely resemble the velocities expected for $q \to 0$. First, the diffuse-phonon coupling is expected to diminish as $q \to 0$ [186]. Second, since the diffuse-phonon coupling tends to reduce the phonon energy (as discussed in this paper and Refs. [19, 225]), at non-zero q the elastic constants should be calculated from data taken after this coupling effect is removed, such as after diffuse scattering is suppressed by field. For ZFC conditions, the value for C_{44} can be about 15% smaller than in FC conditions. This difference is in fact an artifact of calculating the phonon velocity using (reduced) phonon energies at non-zero q (we used data taken at $q = 0.1$ and $q = 0.1 \times \sqrt{2}$ r.l.u. for the calculation in the T1 and T2 directions, respectively). If one could obtain the phonon velocity using smaller q values near $q = 0$ where the diffuse-phonon coupling diminishes, the difference between ZFC and FC data should become negligible.

6.7 Summary

We have observed, when comparing field-cooling and zero-field-cooling conditions for different Brillouin zones with a field along [001], a change in the lattice dynamics of 0.68PMN-0.32PT that correlates with changes in diffuse scattering. Specifically, under field cooling we see a reduction of intensity and an increase of phonon energy for the TA_1 mode measured near (001) and propagating along [100] ($\langle 001 \rangle$-polarized), but no change for TA_1 phonons

near (100) and propagating along [001] ($\langle 100 \rangle$-polarized). This field effect is only clearly seen for wavevectors around 0.1 to 0.2 r.l.u. away from the Bragg peak. Meanwhile, the T1-diffuse scattering near (001) is suppressed under field-cooling, but is unaffected near (100). A similar effect is seen for the TO_1 mode, which is slightly suppressed near (002) from 4 to 9 meV, but unaffected near (200). No clear field effect has been seen for the longitudinal modes near (001) or (100), or for the TA_2 mode near (101). The similarities in the effect of field on the T1-diffuse scattering near (001) and (100), the TA_1 phonons near (001) and (100), and the TO_1 phonons near (002) and (200) suggest the presence of diffuse-TA and diffuse-TO mode coupling which resembles the mode coupling observed in the T2 directions in related relaxor materials.

7 Conclusions

This dissertation has covered research on four disparate systems, the proposed topological superconductor $Cu_xBi_2Se_3$ (Sec. 3), the iron-based superconductor family $Fe_{1+y}Te_{1-x}Se_x$ (Sec. 4), the cuprate superconductor $La_{1.9}Ca_{1.1}Cu_2O_{6+\delta}$ (Sec. 5), and the relaxor ferroelectric $Pb(Mg_{1/3}Nb_{2/3})_{0.68}Ti_{0.32}O_3$ (0.68PMN-0.32PT) (Sec. 6). One thing these materials all have in common is deviation from perfect crystalline order. Although disorder and inhomogeneity is often neglected as a first approximation in understanding the properties of materials, it may be helpful to review these systems to remind ourselves of the many ways disorder and inhomogeneity can be present.

In $Cu_xBi_2Se_3$, our materials synthesis experiments highlight conditions beneficial for producing samples with large superconductivity, and hint that a metastable impurity phase may be responsible for the superconductivity. Unfortunately, we do not yet have a clearer picture of where the superconductivity arises, and plausible alternative viewpoints exist, such as that suggesting that Cu-intercalated Bi_2Se_3 is simply very sensitive to factors such as mechanical stress that may cause the material to lose the ability to superconduct [246]. Nevertheless, one should be mindful of the possibility that a secondary phase may be present and responsible for a property such as superconductivity, as in the iron-based superconductor $K_xFe_{2-y}Se_2$ [106–109].

$Cu_xBi_2Se_3$ and $K_xFe_{2-y}Se_2$ also present examples of the importance of time in materials synthesis, and how inhomogeneity and disorder are affected by it. A high-temperature phase can sometimes be preserved by quickly cooling from that phase before the material has a chance to equilibrate. This is the case for the superconducting phase in $K_xFe_{2-y}Se_2$ [104]. The relaxor ferroelectric $Pb(Sc_{0.5}Ti_{0.5})O_3$ provides another example, with ordering of Sc and Ti present under long annealing temperatures, and disorder present if the system is cooled quickly from high temperatures [172][24]. A third example is the $La_2CuO_{4+\delta}$ system, where interstitial oxygen atoms are mobile at 300 K but frozen at lower temperatures; the superconducting transition temperature and volume fraction both change depending on how fast one cools from 300 to <50 K [134]. In our neutron scattering experiments on the similar compound $La_{1.9}Ca_{1.1}Cu_2O_{6+\delta}$, we saw superstructural peaks suggestive

[24] On the other hand, the relaxor $Pb(Mg_{1/3}Nb_{2/3})O_3$ (and presumably Ti-doped variants such as the material we studied in Section 6) do not change their ordering tendencies under different annealing conditions, possibly due to having an order-disorder transition that is well below temperatures at which ions are mobile on a reasonable time-scale [170].

of ordering induced by interstitial oxygen atoms, but a better understanding of the possibility of phase separation in this system is needed.

Many of these materials have multiple types of disorder and inhomogeneity. For example, in relaxor ferroelectrics such as 0.68PMN-0.32PT, the "B" site (in the perovskite formula ABO_3) is, to some degree, randomly occupied by Mg, Nb, and Ti atoms. However, there are some nanoscale regions which have partial ordering on the B-site, and other regions with disorder [170]. In addition to this chemical disorder, polar short-range order sets in below a certain temperature, as seen from neutron diffuse scattering [185]. The cuprates provide more examples of multiple types of disorder and inhomogeneity. Most cuprates have some form of chemical disorder, with possible effects on the superconducting transition temperature [247] or on the energy width of the neutron scattering "resonance" feature [140]. In addition, electronic inhomogeneity may be present in the form of charge or spin stripes [21]. Also, as mentioned above, phase segregation involving interstitial oxygen is present in $La_2CuO_{4+\delta}$, and we speculate that it could be present in $La_{1.9}Ca_{1.1}Cu_2O_{6+\delta}$.

Vibrational properties can be affected in many ways by deviations from perfect crystalline order. In Section 4, I presented a case that, in $Fe_{1+y}Te_{1-x}Se_x$, the anomalous visibility of a phonon branch for certain wavevectors may be due to disorder. In this case, the disorder would result in depolarization of phonon modes. Similarly, the lattice vibrations of 0.68PMN-0.32PT appear to be coupled to short-range polar order, as shown in Section 6. Application of electric field appeared to suppress short-range order polarized in certain directions, which in turn affected phonon intensities and energies.

Overall, in each of these systems, our research addressed an important issue in understanding the material's properties. In $Cu_xBi_2Se_3$, our materials synthesis experiments highlighted conditions beneficial for producing samples with large superconducting volume fractions, and suggested that a metastable impurity phase may be responsible for the superconductivity. In neutron scattering experiments on $Fe_{1+y-z}Ni_zTe_{1-x}Se_x$, we further characterized an anomalous phonon mode visible at wavevectors where the expected phonons should not be visible, and proposed that disorder may explain the visibility of this mode. In $La_{1.9}Ca_{1.1}Cu_2O_{6+\delta}$, we conducted inelastic neutron scattering experiments on an annealed, superconducting single crystal; surprisingly, the magnetic excitations were commensurate, unlike those seen in hole-doped superconducting cuprates. Judging from the similar compound $La_2CuO_{4+\delta}$, there could be superstructural ordering and phase separation

involving interstitial oxygen in oxygen-doped $La_{1.9}Ca_{1.1}Cu_2O_{6+\delta}$. Lastly, in $Pb(Mg_{1/3}Nb_{2/3})_{0.68}Ti_{0.32}O_3$, we conducted neutron scattering experiments involving applied electric field and compared data taken under field-cooled and zero-field-cooled conditions. We interpreted anisotropic changes in diffuse scattering and transversly polarized phonon characteristics as indicating a coupling between these phonons and short-range polar order. As different as these four systems may be, they each show a potential example of the role of disorder and inhomogeneity, whether in the form of secondary phases, chemical disorder, or short-range order, in the properties of materials.

References

[1] Y. S. Hor, A. J. Williams, J. G. Checkelsky, P. Roushan, J. Seo, Q. Xu, H. W. Zandbergen, A. Yazdani, N. P. Ong, and R. J. Cava. Superconductivity in $Cu_xBi_2Se_3$ and its Implications for Pairing in the Undoped Topological Insulator. *Phys. Rev. Lett.*, 104(5):057001, February 2010. doi: 10.1103/PhysRevLett.104.057001. URL `http://link.aps.org/doi/10.1103/PhysRevLett.104.057001`.

[2] Liang Fu and Erez Berg. Odd-Parity Topological Superconductors: Theory and Application to $Cu_xBi_2Se_3$. *Phys. Rev. Lett.*, 105(9):097001, August 2010. doi: 10.1103/PhysRevLett.105.097001. URL `http://link.aps.org/doi/10.1103/PhysRevLett.105.097001`.

[3] Satoshi Sasaki, M. Kriener, Kouji Segawa, Keiji Yada, Yukio Tanaka, Masatoshi Sato, and Yoichi Ando. Topological Superconductivity in $Cu_xBi_2Se_3$. *Phys. Rev. Lett.*, 107(21):217001, November 2011. doi: 10.1103/PhysRevLett.107.217001. URL `http://link.aps.org/doi/10.1103/PhysRevLett.107.217001`.

[4] M. Z. Hasan and C. L. Kane. Colloquium: Topological insulators. *Rev. Mod. Phys.*, 82(4):3045–3067, November 2010. doi: 10.1103/RevModPhys.82.3045. URL `http://link.aps.org/doi/10.1103/RevModPhys.82.3045`.

[5] Shingo Yonezawa. Bulk Topological Superconductors. *AAPPS Bulletin*, 26(3):3–11, June 2016. URL `http://arxiv.org/abs/1604.07930`. arXiv: 1604.07930.

[6] Yoichi Kamihara, Takumi Watanabe, Masahiro Hirano, and Hideo Hosono. Iron-Based Layered Superconductor $La[O_{1-x}F_x]FeAs$ (x = 0.05-0.12) with T_c = 26 K. *J. Am. Chem. Soc.*, 130(11):3296–3297, February 2008. ISSN 0002-7863. doi: 10.1021/ja800073m. URL `http://dx.doi.org/10.1021/ja800073m`.

[7] Cao Wang, Linjun Li, Shun Chi, Zengwei Zhu, Zhi Ren, Yuke Li, Yuetao Wang, Xiao Lin, Yongkang Luo, Shuai Jiang, Xiangfan Xu, Guanghan Cao, and Zhu'an Xu. Thorium-doping–induced superconductivity up to 56 K in $Gd_{1-x}Th_xFeAsO$. *EPL*, 83(6):67006,

2008. ISSN 0295-5075. doi: 10.1209/0295-5075/83/67006. URL http://stacks.iop.org/0295-5075/83/i=6/a=67006.

[8] Zhi-An Ren, Wei Lu, Jie Yang, Wei Yi, Xiao-Li Shen, Zheng-Cai Li, Guang-Can Che, Xiao-Li Dong, Li-Ling Sun, Fang Zhou, and Zhong-Xian Zhao. Superconductivity at 55 K in Iron-Based F-Doped Layered Quaternary Compound Sm[$O_{1-x}F_x$]FeAs. *Chinese Phys. Lett.*, 25(6): 2215, 2008. ISSN 0256-307X. doi: 10.1088/0256-307X/25/6/080. URL http://stacks.iop.org/0256-307X/25/i=6/a=080.

[9] Jinsheng Wen, Guangyong Xu, Genda Gu, J M Tranquada, and R J Birgeneau. Interplay between magnetism and superconductivity in iron-chalcogenide superconductors: crystal growth and characterizations. *Reports on Progress in Physics*, 74(12):124503, December 2011. ISSN 0034-4885, 1361-6633. doi: 10.1088/0034-4885/74/12/124503. URL http://iopscience.iop.org/0034-4885/74/12/124503.

[10] David M. Fobes, Igor A. Zaliznyak, Zhijun Xu, Genda Gu, Xu-Gang He, Wei Ku, John M. Tranquada, Yang Zhao, Masaaki Matsuda, V. Ovidu Garlea, and Barry Winn. "Forbidden" phonon: dynamical signature of bond symmetry breaking in the iron chalcogenides. *arXiv:1509.05930 [cond-mat]*, September 2015. URL http://arxiv.org/abs/1509.05930. arXiv: 1509.05930.

[11] Masaki Fujita, Haruhiro Hiraka, Masaaki Matsuda, Masato Matsuura, John M. Tranquada, Shuichi Wakimoto, Guangyong Xu, and Kazuyoshi Yamada. Progress in Neutron Scattering Studies of Spin Excitations in High-T_c Cuprates. *Journal of the Physical Society of Japan*, 81(1):011007, 2012. doi: 10.1143/JPSJ.81.011007. URL http://jpsj.ipap.jp/link?JPSJ/81/011007/.

[12] B. O. Wells, Y. S. Lee, M. A. Kastner, R. J. Christianson, R. J. Birgeneau, K. Yamada, Y. Endoh, and G. Shirane. Incommensurate Spin Fluctuations in High-Transition Temperature Superconductors. *Science*, 277(5329):1067–1071, August 1997. ISSN 0036-8075, 1095-9203. doi: 10.1126/science.277.5329.1067. URL http://science.sciencemag.org/content/277/5329/1067.

[13] Thomas R. Shrout and Jr. Fielding, J. Relaxor ferroelectric materials. In *Ultrasonics Symposium, 1990. Proceedings., IEEE 1990*, pages 711–720 vol.2, December 1990. doi: 10.1109/ULTSYM.1990.171456.

[14] Yiping Guo, Haosu Luo, Di Ling, Haiqing Xu, Tianhou He, and Zhiwen Yin. The phase transition sequence and the location of the morphotropic phase boundary region in $(1-x)[Pb(Mg_{1/3}Nb_{2/3})O_3]$–$x PbTiO_3$ single crystal. *J. Phys.: Condens. Matter*, 15(2):L77, January 2003. ISSN 0953-8984. doi: 10.1088/0953-8984/15/2/110. URL http://iopscience.iop.org/0953-8984/15/2/110.

[15] Guangyong Xu. Competing Orders in PZN–xPT and PMN–xPT Relaxor Ferroelectrics. *J. Phys. Soc. Jpn.*, 79(1):011011, January 2010. doi: 10.1143/JPSJ.79.011011. URL http://jpsj.ipap.jp/link?JPSJ/79/011011/.

[16] Seung-Eek Park and Thomas R. Shrout. Ultrahigh strain and piezoelectric behavior in relaxor based ferroelectric single crystals. *J. Appl. Phys.*, 82(4):1804–1811, August 1997. ISSN 0021-8979, 1089-7550. doi: 10.1063/1.365983. URL http://scitation.aip.org/content/aip/journal/jap/82/4/10.1063/1.365983.

[17] Guangyong Xu. Probing local polar structures in PZN-xPT and PMN-xPT relaxor ferroelectrics with neutron and x-ray scattering. *J. Phys.: Conf. Ser.*, 320(1):012081, September 2011. ISSN 1742-6596. doi: 10.1088/1742-6596/320/1/012081. URL http://iopscience.iop.org/1742-6596/320/1/012081.

[18] Gerald Burns and F. H. Dacol. Crystalline ferroelectrics with glassy polarization behavior. *Phys. Rev. B*, 28(5):2527–2530, September 1983. doi: 10.1103/PhysRevB.28.2527. URL http://link.aps.org/doi/10.1103/PhysRevB.28.2527.

[19] Guangyong Xu, Jinsheng Wen, C. Stock, and P. M. Gehring. Phase instability induced by polar nanoregions in a relaxor ferroelectric system. *Nat. Mater.*, 7(7):562–566, July 2008. ISSN 1476-1122. doi: 10.1038/nmat2196. URL http://www.nature.com/nmat/journal/v7/n7/abs/nmat2196.html.

[20] *Frontiers in Crystalline Matter: From Discovery to Technology*. National Academies Press, Washington, D.C., October 2009. ISBN 978-0-309-13800-0. URL http://www.nap.edu/catalog/12640.

[21] John M. Tranquada. Spins, stripes, and superconductivity in hole-doped cuprates. *AIP Conference Proceedings*, 1550:114–187, August 2013. doi: 10.1063/1.4818402. URL http://scitation.aip.org/content/aip/proceeding/aipcp/10.1063/1.4818402.

[22] Govindhan Dhanaraj, Kullaiah Byrappa, Vishwanath (Vish) Prasad, and Michael Dudley. Crystal Growth Techniques and Characterization: An Overview. In Dr Govindhan Dhanaraj Dr, Prof Kullaiah Byrappa, Dr Vishwanath Prasad Dr, and Prof Michael Dudley Dr, editors, *Springer Handbook of Crystal Growth*, pages 3–16. Springer Berlin Heidelberg, 2010. ISBN 978-3-540-74182-4 978-3-540-74761-1. URL http://link.springer.com/chapter/10.1007/978-3-540-74761-1_1. DOI: 10.1007/978-3-540-74761-1_1.

[23] B. N. Brockhouse, H. E. Abou-Helal, and E. D. Hallman. Lattice vibrations in iron at 296°K. *Solid State Communications*, 5(4): 211–216, April 1967. ISSN 0038-1098. doi: 10.1016/0038-1098(67)90258-X. URL http://www.sciencedirect.com/science/article/pii/003810986790258X.

[24] U. Patel, J. Hua, S. H. Yu, S. Avci, Z. L. Xiao, H. Claus, J. Schlueter, V. V. Vlasko-Vlasov, U. Welp, and W. K. Kwok. Growth and superconductivity of $FeSe_x$ crystals. *Applied Physics Letters*, 94(8): 082508, February 2009. ISSN 0003-6951, 1077-3118. doi: 10.1063/1.3093838. URL http://scitation.aip.org/content/aip/journal/apl/94/8/10.1063/1.3093838.

[25] P. W. Bridgman. Certain Physical Properties of Single Crystals of Tungsten, Antimony, Bismuth, Tellurium, Cadmium, Zinc, and Tin. *Proceedings of the American Academy of Arts and Sciences*, 60(6):305–383, 1925. ISSN 0199-9818. doi: 10.2307/25130058. URL http://www.jstor.org/stable/25130058.

[26] Donald C. Stockbarger. The Production of Large Single Crystals of Lithium Fluoride. *Review of Scientific Instruments*, 7(3):133–136, March 1936. ISSN 0034-6748, 1089-7623. doi: 10.1063/1.1752094.

URL http://scitation.aip.org/content/aip/journal/rsi/7/3/10.1063/1.1752094.

[27] S.H. Han, G.D. Gu, Y. Shao, G.J. Russell, and N. Koshizuka. The effect of annealing on the superconducting properties and structure of Bi-2212 single crystals. *Physica C: Superconductivity*, 246(1–2): 22–28, May 1995. ISSN 0921-4534. doi: 10.1016/0921-4534(95)00137-9. URL http://www.sciencedirect.com/science/article/pii/0921453495001379.

[28] R. J. Cava. Structural Chemistry and the Local Charge Picture of Copper Oxide Superconductors. *Science*, 247(4943):656–662, February 1990. ISSN 0036-8075, 1095-9203. doi: 10.1126/science.247.4943.656. URL http://www.sciencemag.org/content/247/4943/656.

[29] Hanna A. Dabkowska and Antoni B. Dabkowski. Crystal Growth of Oxides by Optical Floating Zone Technique. In Govindhan Dhanaraj, Kullaiah Byrappa, Vishwanath Prasad, and Michael Dudley, editors, *Springer Handbook of Crystal Growth*, pages 367–391. Springer Berlin Heidelberg, 2010. ISBN 978-3-540-74761-1. URL http://www.springerlink.com/content/x731731u71468736/abstract/.

[30] S. M. Koohpayeh. Single crystal growth by the traveling solvent technique: A review. *Progress in Crystal Growth and Characterization of Materials*, May 2016. ISSN 0960-8974. doi: 10.1016/j.pcrysgrow.2016.03.001. URL http://www.sciencedirect.com/science/article/pii/S0960897416300018.

[31] R. Y. Chen, S. J. Zhang, J. A. Schneeloch, C. Zhang, Q. Li, G. D. Gu, and N. L. Wang. Optical spectroscopy study of the three-dimensional Dirac semimetal $ZrTe_5$. *Phys. Rev. B*, 92(7):075107, August 2015. doi: 10.1103/PhysRevB.92.075107. URL http://link.aps.org/doi/10.1103/PhysRevB.92.075107.

[32] I.R. Fisher, M.C. Shapiro, and J.G. Analytis. Principles of crystal growth of intermetallic and oxide compounds from molten solutions. *Philosophical Magazine*, 92(19-21):2401–2435, May 2012. ISSN 1478-6435. doi: 10.1080/14786435.2012.685192. URL http://dx.doi.org/10.1080/14786435.2012.685192.

[33] W Chen and Z. G Ye. Top seeded solution growth and characterization of piezo-/ferroelectric $(1-x)\mathrm{Pb}(\mathrm{Zn}_{1/3}\mathrm{Nb}_{2/3})\mathrm{O}_3$–$x\mathrm{PbTiO}_3$ single crystals. *Journal of Crystal Growth*, 233(3):503–511, December 2001. ISSN 0022-0248. doi: 10.1016/S0022-0248(01)01596-2. URL `http://www.sciencedirect.com/science/article/pii/S0022024801015962`.

[34] X. Zhao, G. Yu, Y.-C. Cho, G. Chabot-Couture, N. Barišić, P. Bourges, N. Kaneko, Y. Li, L. Lu, E. M. Motoyama, O. P. Vajk, and M. Greven. Crystal Growth and Characterization of the Model High-Temperature Superconductor $\mathrm{HgBa}_2\mathrm{CuO}_{4+\delta}$. *Advanced Materials*, 18 (24):3243–3247, December 2006. ISSN 1521-4095. doi: 10.1002/adma.200600931. URL `http://onlinelibrary.wiley.com/doi/10.1002/adma.200600931/abstract`.

[35] Vitali A. Tatartchenko. Shaped Crystal Growth. In *Springer Handbook of Crystal Growth*. Springer, 2010.

[36] Chul-Ho Lee, Nobuhisa Kaneko, Syoichi Hosoya, Kenji Kurahashi, Shuichi Wakimoto, Kazuyoshi Yamada, and Yasuo Endoh. Growth of large single crystals using the improved lamp-image floating-zone furnace: application to $\mathrm{La}_{2-x}\mathrm{Sr}_x\mathrm{CuO}_4$. *Superconductor Science and Technology*, 11(9):891–897, September 1998. ISSN 0953-2048, 1361-6668. doi: 10.1088/0953-2048/11/9/011. URL `http://iopscience.iop.org/0953-2048/11/9/011`.

[37] Gen Shirane, Stephen M. Shapiro, and John M. Tranquada. Neutron Scattering with a Triple-Axis Spectrometer. Cambridge University Press, Cambridge, United Kingdom, 2002.

[38] Stephen William Lovesey. *Theory of Neutron Scattering from Condensed Matter*, volume 1. Clarendon Press, Oxford, United Kingdom, 1984.

[39] Zhijun Xu, J. A. Schneeloch, Jinsheng Wen, E. S. Božin, G. E. Granroth, B. L. Winn, M. Feygenson, R. J. Birgeneau, Genda Gu, I. A. Zaliznyak, J. M. Tranquada, and Guangyong Xu. Thermal evolution of antiferromagnetic correlations and tetrahedral bond angles in superconducting $\mathrm{FeTe}_{1-x}\mathrm{Se}_x$. *Phys. Rev. B*, 93(10):104517, March 2016. doi: 10.1103/PhysRevB.93.104517. URL `http://link.aps.org/doi/10.1103/PhysRevB.93.104517`.

[40] Rahul Roy. Topological superfluids with time reversal symmetry. *arXiv:0803.2868*, March 2008. URL http://arxiv.org/abs/0803.2868.

[41] Satoshi Sasaki, Zhi Ren, A. A. Taskin, Kouji Segawa, Liang Fu, and Yoichi Ando. Odd-Parity Pairing and Topological Superconductivity in a Strongly Spin-Orbit Coupled Semiconductor. *Phys. Rev. Lett.*, 109(21):217004, November 2012. doi: 10.1103/PhysRevLett.109.217004. URL http://link.aps.org/doi/10.1103/PhysRevLett.109.217004.

[42] D. J. Thouless, M. Kohmoto, M. P. Nightingale, and M. den Nijs. Quantized Hall Conductance in a Two-Dimensional Periodic Potential. *Phys. Rev. Lett.*, 49(6):405–408, August 1982. doi: 10.1103/PhysRevLett.49.405. URL http://link.aps.org/doi/10.1103/PhysRevLett.49.405.

[43] Xiao-Liang Qi and Shou-Cheng Zhang. Topological insulators and superconductors. *Rev. Mod. Phys.*, 83(4):1057–1110, October 2011. doi: 10.1103/RevModPhys.83.1057. URL http://link.aps.org/doi/10.1103/RevModPhys.83.1057.

[44] Pedram Roushan, Jungpil Seo, Colin V. Parker, Y. S. Hor, D. Hsieh, Dong Qian, Anthony Richardella, M. Z. Hasan, R. J. Cava, and Ali Yazdani. Topological surface states protected from backscattering by chiral spin texture. *Nature*, 460(7259):1106–1109, August 2009. ISSN 0028-0836. doi: 10.1038/nature08308. URL http://www.nature.com/nature/journal/v460/n7259/abs/nature08308.html.

[45] Liang Fu. Topological Crystalline Insulators. *Phys. Rev. Lett.*, 106 (10):106802, March 2011. doi: 10.1103/PhysRevLett.106.106802. URL http://link.aps.org/doi/10.1103/PhysRevLett.106.106802.

[46] Timothy H. Hsieh, Hsin Lin, Junwei Liu, Wenhui Duan, Arun Bansil, and Liang Fu. Topological crystalline insulators in the SnTe material class. *Nat Commun*, 3:982, July 2012. doi: 10.1038/ncomms1969. URL http://www.nature.com/ncomms/journal/v3/n7/full/ncomms1969.html.

[47] Y. Tanaka, Zhi Ren, T. Sato, K. Nakayama, S. Souma, T. Takahashi, Kouji Segawa, and Yoichi Ando. Experimental realization of a topological crystalline insulator in SnTe. *Nature Physics*, 8(11):800–803, September 2012. ISSN 1745-2473. doi: 10.1038/nphys2442. URL http://www.nature.com/nphys/journal/v8/n11/abs/nphys2442.html.

[48] Markus Eschbach, Martin Lanius, Chengwang Niu, Ewa Młyńczak, Pika Gospodarič, Jens Kellner, Peter Schüffelgen, Mathias Gehlmann, Sven Döring, Elmar Neumann, Martina Luysberg, Gregor Mussler, Lukasz Plucinski, Markus Morgenstern, Detlev Grützmacher, Gustav Bihlmayer, Stefan Blügel, and Claus M. Schneider. BiTe: a dual topological insulator. *arXiv:1604.08886 [cond-mat]*, April 2016. URL http://arxiv.org/abs/1604.08886. arXiv: 1604.08886.

[49] Fan Zhang, C. L. Kane, and E. J. Mele. Topological Mirror Superconductivity. *Phys. Rev. Lett.*, 111(5):056403, August 2013. doi: 10.1103/PhysRevLett.111.056403. URL http://link.aps.org/doi/10.1103/PhysRevLett.111.056403.

[50] Roger S. K. Mong, Andrew M. Essin, and Joel E. Moore. Antiferromagnetic topological insulators. *Phys. Rev. B*, 81(24):245209, June 2010. doi: 10.1103/PhysRevB.81.245209. URL http://link.aps.org/doi/10.1103/PhysRevB.81.245209.

[51] Rundong Li, Jing Wang, Xiao-Liang Qi, and Shou-Cheng Zhang. Dynamical axion field in topological magnetic insulators. *Nat Phys*, 6(4):284–288, April 2010. ISSN 1745-2473. doi: 10.1038/nphys1534. URL http://www.nature.com/nphys/journal/v6/n4/full/nphys1534.html.

[52] A. Alexandradinata, Zhijun Wang, and B. Andrei Bernevig. Topological Insulators from Group Cohomology. *Phys. Rev. X*, 6(2):021008, April 2016. doi: 10.1103/PhysRevX.6.021008. URL http://link.aps.org/doi/10.1103/PhysRevX.6.021008.

[53] Zhijun Wang, A. Alexandradinata, R. J. Cava, and B. Andrei Bernevig. Hourglass fermions. *Nature*, 532(7598):189–194, April 2016. ISSN 0028-0836. doi: 10.1038/nature17410. URL http://www.nature.com/nature/journal/v532/n7598/full/nature17410.html.

[54] Oskar Vafek and Ashvin Vishwanath. Dirac Fermions in Solids: From High-Tc Cuprates and Graphene to Topological Insulators and Weyl Semimetals. *Annual Review of Condensed Matter Physics*, 5(1):83–112, 2014. doi: 10.1146/annurev-conmatphys-031113-133841. URL http://dx.doi.org/10.1146/annurev-conmatphys-031113-133841.

[55] Yoichi Ando. Topological Insulator Materials. *J. Phys. Soc. Jpn.*, 82(10):102001, October 2013. ISSN 0031-9015. doi: 10.7566/JPSJ.82.102001. URL http://journals.jps.jp/doi/abs/10.7566/JPSJ.82.102001.

[56] S. M. Young, S. Zaheer, J. C. Y. Teo, C. L. Kane, E. J. Mele, and A. M. Rappe. Dirac Semimetal in Three Dimensions. *Phys. Rev. Lett.*, 108 (14):140405, April 2012. doi: 10.1103/PhysRevLett.108.140405. URL http://link.aps.org/doi/10.1103/PhysRevLett.108.140405.

[57] Xiangang Wan, Ari M. Turner, Ashvin Vishwanath, and Sergey Y. Savrasov. Topological semimetal and Fermi-arc surface states in the electronic structure of pyrochlore iridates. *Phys. Rev. B*, 83(20):205101, May 2011. doi: 10.1103/PhysRevB.83.205101. URL http://link.aps.org/doi/10.1103/PhysRevB.83.205101.

[58] Su-Yang Xu, Ilya Belopolski, Nasser Alidoust, Madhab Neupane, Guang Bian, Chenglong Zhang, Raman Sankar, Guoqing Chang, Zhujun Yuan, Chi-Cheng Lee, Shin-Ming Huang, Hao Zheng, Jie Ma, Daniel S. Sanchez, BaoKai Wang, Arun Bansil, Fangcheng Chou, Pavel P. Shibayev, Hsin Lin, Shuang Jia, and M. Zahid Hasan. Discovery of a Weyl Fermion semimetal and topological Fermi arcs. *Science*, page aaa9297, July 2015. ISSN 0036-8075, 1095-9203. doi: 10.1126/science.aaa9297. URL http://science.sciencemag.org/content/early/2015/07/15/science.aaa9297.

[59] B.Q. Lv, H.M. Weng, B.B. Fu, X.P. Wang, H. Miao, J. Ma, P. Richard, X.C. Huang, L.X. Zhao, G.F. Chen, Z. Fang, X. Dai, T. Qian, and H. Ding. Experimental Discovery of Weyl Semimetal TaAs. *Phys. Rev. X*, 5(3):031013, July 2015. doi: 10.1103/PhysRevX.5.031013. URL http://link.aps.org/doi/10.1103/PhysRevX.5.031013.

[60] Z. K. Liu, B. Zhou, Y. Zhang, Z. J. Wang, H. M. Weng, D. Prabhakaran, S.-K. Mo, Z. X. Shen, Z. Fang, X. Dai, Z. Hussain, and

Y. L. Chen. Discovery of a Three-Dimensional Topological Dirac Semimetal, Na_3Bi. *Science*, 343(6173):864–867, February 2014. ISSN 0036-8075, 1095-9203. doi: 10.1126/science.1245085. URL http://science.sciencemag.org/content/343/6173/864.

[61] Steven R. Elliott and Marcel Franz. Colloquium: Majorana fermions in nuclear, particle, and solid-state physics. *Rev. Mod. Phys.*, 87(1):137–163, February 2015. doi: 10.1103/RevModPhys.87.137. URL http://link.aps.org/doi/10.1103/RevModPhys.87.137.

[62] Martin Leijnse and Karsten Flensberg. Introduction to topological superconductivity and Majorana fermions. *Semicond. Sci. Technol.*, 27(12):124003, December 2012. ISSN 0268-1242, 1361-6641. doi: 10.1088/0268-1242/27/12/124003. URL http://iopscience.iop.org/0268-1242/27/12/124003.

[63] Liang Fu and C. L. Kane. Superconducting Proximity Effect and Majorana Fermions at the Surface of a Topological Insulator. *Phys. Rev. Lett.*, 100(9):096407, March 2008. doi: 10.1103/PhysRevLett.100.096407. URL http://link.aps.org/doi/10.1103/PhysRevLett.100.096407.

[64] L. Andrew Wray, Suyang Xu, Yuqi Xia, Dong Qian, Alexei V. Fedorov, Hsin Lin, Arun Bansil, Liang Fu, Yew San Hor, Robert J. Cava, and M. Zahid Hasan. Spin-orbital ground states of superconducting doped topological insulators: A Majorana platform. *Phys. Rev. B*, 83(22):224516, June 2011. doi: 10.1103/PhysRevB.83.224516. URL http://link.aps.org/doi/10.1103/PhysRevB.83.224516.

[65] Xiao-Liang Qi, Taylor L. Hughes, S. Raghu, and Shou-Cheng Zhang. Time-Reversal-Invariant Topological Superconductors and Superfluids in Two and Three Dimensions. *Phys. Rev. Lett.*, 102(18):187001, May 2009. doi: 10.1103/PhysRevLett.102.187001. URL http://link.aps.org/doi/10.1103/PhysRevLett.102.187001.

[66] C.W.J. Beenakker. Search for Majorana Fermions in Superconductors. *Annual Review of Condensed Matter Physics*, 4(1):113–136, April 2013. doi: 10.1146/annurev-conmatphys-030212-184337. URL http://www.annualreviews.org/doi/abs/10.1146/annurev-conmatphys-030212-184337.

[67] A. Yu. Kitaev. Fault-tolerant quantum computation by anyons. *Annals of Physics*, 303(1):2–30, January 2003. ISSN 0003-4916. doi: 10.1016/S0003-4916(02)00018-0. URL http://www.sciencedirect.com/science/article/pii/S0003491602000180.

[68] Chetan Nayak, Steven H. Simon, Ady Stern, Michael Freedman, and Sankar Das Sarma. Non-Abelian anyons and topological quantum computation. *Rev. Mod. Phys.*, 80(3):1083–1159, September 2008. doi: 10.1103/RevModPhys.80.1083. URL http://link.aps.org/doi/10.1103/RevModPhys.80.1083.

[69] P. Shor. Polynomial-Time Algorithms for Prime Factorization and Discrete Logarithms on a Quantum Computer. *SIAM J. Comput.*, 26(5):1484–1509, October 1997. ISSN 0097-5397. doi: 10.1137/S0097539795293172. URL http://epubs.siam.org/doi/abs/10.1137/S0097539795293172.

[70] Liang Fu and C. L. Kane. Topological insulators with inversion symmetry. *Phys. Rev. B*, 76(4):045302, July 2007. doi: 10.1103/PhysRevB.76.045302. URL http://link.aps.org/doi/10.1103/PhysRevB.76.045302.

[71] Akinori Nishide, Alexey A. Taskin, Yasuo Takeichi, Taichi Okuda, Akito Kakizaki, Toru Hirahara, Kan Nakatsuji, Fumio Komori, Yoichi Ando, and Iwao Matsuda. Direct mapping of the spin-filtered surface bands of a three-dimensional quantum spin Hall insulator. *Phys. Rev. B*, 81(4):041309, January 2010. doi: 10.1103/PhysRevB.81.041309. URL http://link.aps.org/doi/10.1103/PhysRevB.81.041309.

[72] D. Hsieh, D. Qian, L. Wray, Y. Xia, Y. S. Hor, R. J. Cava, and M. Z. Hasan. A topological Dirac insulator in a quantum spin Hall phase. *Nature*, 452(7190):970–974, April 2008. ISSN 0028-0836. doi: 10.1038/nature06843. URL http://www.nature.com/nature/journal/v452/n7190/full/nature06843.html.

[73] Y. Xia, D. Qian, D. Hsieh, L. Wray, A. Pal, H. Lin, A. Bansil, D. Grauer, Y. S. Hor, R. J. Cava, and M. Z. Hasan. Observation of a large-gap topological-insulator class with a single Dirac cone on the surface. *Nat. Phys.*, 5(6):398–402, May 2009. ISSN 1745-2473. doi:

10.1038/nphys1274. URL http://www.nature.com/nphys/journal/v5/n6/full/nphys1274.html.

[74] R. J. Cava, Huiwen Ji, M. K. Fuccillo, Q. D. Gibson, and Y. S. Hor. Crystal structure and chemistry of topological insulators. *J. Mater. Chem. C*, 1(19):3176–3189, April 2013. ISSN 2050-7534. doi: 10.1039/C3TC30186A. URL http://pubs.rsc.org/en/content/articlelanding/2013/tc/c3tc30186a.

[75] S. K. Kushwaha, I. Pletikosić, T. Liang, A. Gyenis, S. H. Lapidus, Yao Tian, He Zhao, K. S. Burch, Jingjing Lin, Wudi Wang, Huiwen Ji, A. V. Fedorov, Ali Yazdani, N. P. Ong, T. Valla, and R. J. Cava. Sn-doped $Bi_{1.1}Sb_{0.9}Te_2S$ bulk crystal topological insulator with excellent properties. *Nat Commun*, 7:11456, April 2016. doi: 10.1038/ncomms11456. URL http://www.nature.com/ncomms/2016/160427/ncomms11456/full/ncomms11456.html.

[76] Andreas P. Schnyder, Shinsei Ryu, Akira Furusaki, and Andreas W. W. Ludwig. Classification of topological insulators and superconductors in three spatial dimensions. *Phys. Rev. B*, 78(19):195125, November 2008. doi: 10.1103/PhysRevB.78.195125. URL http://link.aps.org/doi/10.1103/PhysRevB.78.195125.

[77] Yoichi Ando and Liang Fu. Topological Crystalline Insulators and Topological Superconductors: From Concepts to Materials. *Annual Review of Condensed Matter Physics*, 6(1):361–381, January 2015. doi: 10.1146/annurev-conmatphys-031214-014501. URL http://dx.doi.org/10.1146/annurev-conmatphys-031214-014501.

[78] Masatoshi Sato. Topological odd-parity superconductors. *Phys. Rev. B*, 81(22):220504, June 2010. doi: 10.1103/PhysRevB.81.220504. URL http://link.aps.org/doi/10.1103/PhysRevB.81.220504.

[79] T. Kirzhner, E. Lahoud, K. B. Chaska, Z. Salman, and A. Kanigel. Point-contact spectroscopy of $Cu_{0.2}Bi_2Se_3$ single crystals. *Phys. Rev. B*, 86(6):064517, August 2012. doi: 10.1103/PhysRevB.86.064517. URL http://link.aps.org/doi/10.1103/PhysRevB.86.064517.

[80] X. Chen, C. Huan, Y. S. Hor, C. A. R. Sá de Melo, and Z. Jiang. Point-contact Andreev reflection spectroscopy of candidate topological

superconductor $Cu_{0.25}Bi_2Se_3$. *arXiv:1210.6054*, October 2012. URL http://arxiv.org/abs/1210.6054.

[81] Niv Levy, Tong Zhang, Jeonghoon Ha, Fred Sharifi, A. Alec Talin, Young Kuk, and Joseph A. Stroscio. Experimental Evidence for s-Wave Pairing Symmetry in Superconducting $Cu_xBi_2Se_3$ Single Crystals Using a Scanning Tunneling Microscope. *Phys. Rev. Lett.*, 110(11):117001, March 2013. doi: 10.1103/PhysRevLett.110.117001. URL http://link.aps.org/doi/10.1103/PhysRevLett.110.117001.

[82] Haibing Peng, Debtanu De, Bing Lv, Fengyan Wei, and Ching-Wu Chu. Absence of zero-energy surface bound states in $Cu_xBi_2Se_3$ studied via Andreev reflection spectroscopy. *Phys. Rev. B*, 88(2):024515, July 2013. doi: 10.1103/PhysRevB.88.024515. URL http://link.aps.org/doi/10.1103/PhysRevB.88.024515.

[83] Satoshi Sasaki, Kouji Segawa, and Yoichi Ando. Superconductor derived from a topological insulator heterostructure. *Phys. Rev. B*, 90 (22):220504, December 2014. doi: 10.1103/PhysRevB.90.220504. URL http://link.aps.org/doi/10.1103/PhysRevB.90.220504.

[84] J. A. Schneeloch, R. D. Zhong, Z. J. Xu, G. D. Gu, and J. M. Tranquada. Dependence of superconductivity in $Cu_xBi_2Se_3$ on quenching conditions. *Phys. Rev. B*, 91(14):144506, April 2015. doi: 10.1103/PhysRevB.91.144506. URL http://link.aps.org/doi/10.1103/PhysRevB.91.144506.

[85] Alexei Kitaev. Periodic table for topological insulators and superconductors. *AIP Conf. Proc.*, 1134(1):22–30, May 2009. ISSN 0094243X. doi: doi:10.1063/1.3149495. URL http://proceedings.aip.org/resource/2/apcpcs/1134/1/22_1.

[86] Takeshi Mizushima, Ai Yamakage, Masatoshi Sato, and Yukio Tanaka. Dirac-fermion-induced parity mixing in superconducting topological insulators. *Phys. Rev. B*, 90(18):184516, November 2014. doi: 10.1103/PhysRevB.90.184516. URL http://link.aps.org/doi/10.1103/PhysRevB.90.184516.

[87] L. Andrew Wray, Su-Yang Xu, Yuqi Xia, Yew San Hor, Dong Qian, Alexei V. Fedorov, Hsin Lin, Arun Bansil, Robert J. Cava, and M. Zahid Hasan. Observation of topological order in a superconducting doped

topological insulator. *Nat Phys*, 6(11):855–859, November 2010. ISSN 1745-2473. doi: 10.1038/nphys1762. URL http://dx.doi.org/10.1038/nphys1762.

[88] Yi-Lin Wang, Yong Xu, Ye-Ping Jiang, Jun-Wei Liu, Cui-Zu Chang, Mu Chen, Zhi Li, Can-Li Song, Li-Li Wang, Ke He, Xi Chen, Wen-Hui Duan, Qi-Kun Xue, and Xu-Cun Ma. Structural defects and electronic properties of the Cu-doped topological insulator Bi_2Se_3. *Phys. Rev. B*, 84(7):075335, August 2011. doi: 10.1103/PhysRevB.84.075335. URL http://link.aps.org/doi/10.1103/PhysRevB.84.075335.

[89] Y. Tanaka, K. Nakayama, S. Souma, T. Sato, N. Xu, P. Zhang, P. Richard, H. Ding, Y. Suzuki, P. Das, K. Kadowaki, and T. Takahashi. Evolution of electronic structure upon Cu doping in the topological insulator Bi_2Se_3. *Phys. Rev. B*, 85(12):125111, March 2012. doi: 10.1103/PhysRevB.85.125111. URL http://link.aps.org/doi/10.1103/PhysRevB.85.125111.

[90] Takeshi Kondo, Y. Nakashima, Y. Ota, Y. Ishida, W. Malaeb, K. Okazaki, S. Shin, M. Kriener, Satoshi Sasaki, Kouji Segawa, and Yoichi Ando. Anomalous Dressing of Dirac Fermions in the Topological Surface State of Bi_2Se_3, Bi_2Te_3, and Cu-doped Bi_2Se_3. *Phys. Rev. Lett.*, 110(21):217601, May 2013. doi: 10.1103/PhysRevLett.110.217601. URL http://link.aps.org/doi/10.1103/PhysRevLett.110.217601.

[91] E. Lahoud, E. Maniv, M. Shaviv Petrushevsky, M. Naamneh, A. Ribak, S. Wiedmann, L. Petaccia, Z. Salman, K. B. Chashka, Y. Dagan, and A. Kanigel. Evolution of the Fermi surface of a doped topological insulator with carrier concentration. *Phys. Rev. B*, 88(19):195107, November 2013. doi: 10.1103/PhysRevB.88.195107. URL http://link.aps.org/doi/10.1103/PhysRevB.88.195107.

[92] M. Kriener, Kouji Segawa, Zhi Ren, Satoshi Sasaki, and Yoichi Ando. Bulk Superconducting Phase with a Full Energy Gap in the Doped Topological Insulator $Cu_xBi_2Se_3$. *Phys. Rev. Lett.*, 106(12):127004, March 2011. doi: 10.1103/PhysRevLett.106.127004. URL http://link.aps.org/doi/10.1103/PhysRevLett.106.127004.

[93] Liang Fu. Odd-parity topological superconductor with nematic order: Application to $Cu_xBi_2Se_3$. *Phys. Rev. B*, 90(10):100509, September 2014. doi: 10.1103/PhysRevB.90.100509. URL http://link.aps.org/doi/10.1103/PhysRevB.90.100509.

[94] Luke J. Sandilands, Anjan A. Reijnders, Markus Kriener, Kouji Segawa, Satoshi Sasaki, Yoichi Ando, and Kenneth S. Burch. Doping-dependent charge dynamics in $Cu_xBi_2Se_3$. *Phys. Rev. B*, 90(9):094503, September 2014. doi: 10.1103/PhysRevB.90.094503. URL http://link.aps.org/doi/10.1103/PhysRevB.90.094503.

[95] Pradip Das, Yusuke Suzuki, Masashi Tachiki, and Kazuo Kadowaki. Spin-triplet vortex state in the topological superconductor $Cu_xBi_2Se_3$. *Phys. Rev. B*, 83(22):220513, June 2011. doi: 10.1103/PhysRevB.83.220513. URL http://link.aps.org/doi/10.1103/PhysRevB.83.220513.

[96] T. V. Bay, T. Naka, Y. K. Huang, H. Luigjes, M. S. Golden, and A. de Visser. Superconductivity in the Doped Topological Insulator $Cu_xBi_2Se_3$ under High Pressure. *Phys. Rev. Lett.*, 108(5):057001, January 2012. doi: 10.1103/PhysRevLett.108.057001. URL http://link.aps.org/doi/10.1103/PhysRevLett.108.057001.

[97] Ben J. Lawson, Y. S. Hor, and Lu Li. Quantum Oscillations in the Topological Superconductor Candidate $Cu_{0.25}Bi_2Se_3$. *Phys. Rev. Lett.*, 109(22):226406, November 2012. doi: 10.1103/PhysRevLett.109.226406. URL http://link.aps.org/doi/10.1103/PhysRevLett.109.226406.

[98] Ryusuke Kondo, Taiki Yoshinaka, Yoshinori Imai, and Atsutaka Maeda. Reproducible Synthetic Method for the Topological Superconductor $Cu_xBi_2Se_3$. *J. Phys. Soc. Jpn.*, 82(6):063702, May 2013. doi: 10.1143/JPSJ.82.063702. URL http://jpsj.ipap.jp/link?JPSJ/82/063702/.

[99] M. Kriener, Kouji Segawa, Zhi Ren, Satoshi Sasaki, Shohei Wada, Susumu Kuwabata, and Yoichi Ando. Electrochemical synthesis and superconducting phase diagram of $Cu_xBi_2Se_3$. *Phys. Rev. B*, 84(5):054513, August 2011. doi: 10.1103/PhysRevB.84.054513. URL http://link.aps.org/doi/10.1103/PhysRevB.84.054513.

[100] Y. S. Hor, A. Richardella, P. Roushan, Y. Xia, J. G. Checkelsky, A. Yazdani, M. Z. Hasan, N. P. Ong, and R. J. Cava. p-type Bi_2Se_3 for topological insulator and low-temperature thermoelectric applications. *Phys. Rev. B*, 79(19):195208, May 2009. doi: 10.1103/PhysRevB.79.195208. URL http://link.aps.org/doi/10.1103/PhysRevB.79.195208.

[101] Tanmay Das, Somnath Bhattacharyya, Bhanu Prakash Joshi, Arumugum Thamizhavel, and Srinivasan Ramakrishnan. Direct evidence of intercalation in a topological insulator turned superconductor. *Materials Letters*, 93:370–373, February 2013. ISSN 0167-577X. doi: 10.1016/j.matlet.2012.11.115. URL http://www.sciencedirect.com/science/article/pii/S0167577X12016941.

[102] N. B. Babanly, Yu A. Yusibov, Z. S. Aliev, and M. B. Babanly. Phase equilibria in the Cu-Bi-Se system and thermodynamic properties of copper selenobismuthates. *Russ. J. Inorg. Chem.*, 55(9):1471–1481, September 2010. ISSN 0036-0236, 1531-8613. doi: 10.1134/S0036023610090238. URL http://link.springer.com.libproxy.cc.stonybrook.edu/article/10.1134/S0036023610090238.

[103] Tetsuroh Shirasawa, Masato Sugiki, Toru Hirahara, Masaki Aitani, Terufusa Shirai, Shuji Hasegawa, and Toshio Takahashi. Structure and transport properties of Cu-doped Bi_2Se_3 films. *Phys. Rev. B*, 89(19):195311, May 2014. doi: 10.1103/PhysRevB.89.195311. URL http://link.aps.org/doi/10.1103/PhysRevB.89.195311.

[104] Jiangang Guo, Shifeng Jin, Gang Wang, Shunchong Wang, Kaixing Zhu, Tingting Zhou, Meng He, and Xiaolong Chen. Superconductivity in the iron selenide $K_xFe_2Se_2$ ($0 \leq x \leq 1.0$). *Phys. Rev. B*, 82(18):180520, November 2010. doi: 10.1103/PhysRevB.82.180520. URL http://link.aps.org/doi/10.1103/PhysRevB.82.180520.

[105] F. Ye, S. Chi, Wei Bao, X. F. Wang, J. J. Ying, X. H. Chen, H. D. Wang, C. H. Dong, and Minghu Fang. Common Crystalline and Magnetic Structure of Superconducting $A_2Fe_4Se_5$ (A=K,Rb,Cs,Tl) Single Crystals Measured Using Neutron Diffraction. *Phys. Rev. Lett.*, 107(13):137003, September 2011. doi: 10.1103/PhysRevLett.107.137003. URL http://link.aps.org/doi/10.1103/PhysRevLett.107.137003.

[106] Peng Cai, Cun Ye, Wei Ruan, Xiaodong Zhou, Aifeng Wang, Meng Zhang, Xianhui Chen, and Yayu Wang. Imaging the coexistence of a superconducting phase and a charge-density modulation in the $K_{0.73}Fe_{1.67}Se_2$ superconductor using a scanning tunneling microscope. *Phys. Rev. B*, 85(9):094512, March 2012. doi: 10.1103/PhysRevB.85.094512. URL http://link.aps.org/doi/10.1103/PhysRevB.85.094512.

[107] R. H. Yuan, T. Dong, Y. J. Song, P. Zheng, G. F. Chen, J. P. Hu, J. Q. Li, and N. L. Wang. Nanoscale phase separation of antiferromagnetic order and superconductivity in $K_{0.75}Fe_{1.75}Se_2$. *Scientific Reports*, 2, January 2012. ISSN 2045-2322. doi: 10.1038/srep00221. URL http://www.nature.com/srep/2012/120112/srep00221/full/srep00221.html.

[108] Alessandro Ricci, Nicola Poccia, Boby Joseph, Gianmichele Arrighetti, Luisa Barba, Jasper Plaisier, Gaetano Campi, Yoshikazu Mizuguchi, Hiroyuki Takeya, Yoshihiko Takano, Naurang Lal Saini, and Antonio Bianconi. Intrinsic phase separation in superconducting $K_{0.8}Fe_{1.6}Se_2$ (T_c = 31.8 K) single crystals. *Superconductor Science and Technology*, 24(8):082002, August 2011. ISSN 0953-2048, 1361-6668. doi: 10.1088/0953-2048/24/8/082002. URL http://iopscience.iop.org/0953-2048/24/8/082002.

[109] Wei Li, Hao Ding, Peng Deng, Kai Chang, Canli Song, Ke He, Lili Wang, Xucun Ma, Jiang-Ping Hu, Xi Chen, and Qi-Kun Xue. Phase separation and magnetic order in K-doped iron selenide superconductor. *Nature Physics*, 8(2):126–130, November 2012. ISSN 1745-2473. doi: 10.1038/nphys2155. URL http://www.nature.com/nphys/journal/v8/n2/abs/nphys2155.html.

[110] Fei Han, Huan Yang, Bing Shen, Zhen-Yu Wang, Chun-Hong Li, and Hai-Hu Wen. Metastable superconducting state in quenched $K_xFe_{2-y}Se_2$. *Philosophical Magazine*, 92(19-21):2553–2562, April 2012. ISSN 1478-6435. doi: 10.1080/14786435.2012.681711. URL http://www.tandfonline.com/doi/abs/10.1080/14786435.2012.681711.

[111] Y. J. Yan, M. Zhang, A. F. Wang, J. J. Ying, Z. Y. Li, W. Qin, X. G. Luo, J. Q. Li, Jiangping Hu, and X. H. Chen. Electronic and magnetic phase diagram in $K_xFe_{2-y}Se_2$ superconductors.

Scientific Reports, 2, January 2012. ISSN 2045-2322. doi: 10.1038/srep00212. URL http://www.nature.com/srep/2012/120106/srep00212/full/srep00212.html.

[112] Naoyuki Katayama, Sungdae Ji, Despina Louca, Seunghun Lee, Masaki Fujita, Taku J. Sato, Jinsheng Wen, Zhijun Xu, Genda Gu, Guangyong Xu, Ziwei Lin, Masanori Enoki, Sung Chang, Kazuyoshi Yamada, and John M. Tranquada. Investigation of the Spin-Glass Regime between the Antiferromagnetic and Superconducting Phases in $Fe_{1+y}Se_xTe_{1-x}$. *Journal of the Physical Society of Japan*, 79(11): 113702, October 2010. doi: 10.1143/JPSJ.79.113702. URL http://jpsj.ipap.jp/link?JPSJ/79/113702/.

[113] T. Mousavi, C. R. M. Grovenor, and S. C. Speller. Structural parameters affecting superconductivity in iron chalcogenides: a review. *Mater. Sci. Technol.*, 30(15):1929–1943, April 2014. ISSN 0267-0836. doi: 10.1179/1743284714Y.0000000551. URL http://www.maneyonline.com/doi/abs/10.1179/1743284714Y.0000000551.

[114] R. Shipra, H. Takeya, K. Hirata, and A. Sundaresan. Effects of Ni and Co doping on the physical properties of tetragonal $FeSe_{0.5}Te_{0.5}$ superconductor. *Physica C: Superconductivity*, 470(13–14): 528–532, July 2010. ISSN 0921-4534. doi: 10.1016/j.physc.2010.04.009. URL http://www.sciencedirect.com/science/article/pii/S0921453410002510.

[115] Wei Bao, Y. Qiu, Q. Huang, M. A. Green, P. Zajdel, M. R. Fitzsimmons, M. Zhernenkov, S. Chang, Minghu Fang, B. Qian, E. K. Vehstedt, Jinhu Yang, H. M. Pham, L. Spinu, and Z. Q. Mao. Tunable ($\delta\pi$, $\delta\pi$)-Type Antiferromagnetic Order in α-Fe(Te,Se) Superconductors. *Phys. Rev. Lett.*, 102(24):247001, June 2009. doi: 10.1103/PhysRevLett.102.247001. URL http://link.aps.org/doi/10.1103/PhysRevLett.102.247001.

[116] T. M. McQueen, A. J. Williams, P. W. Stephens, J. Tao, Y. Zhu, V. Ksenofontov, F. Casper, C. Felser, and R. J. Cava. Tetragonal-to-Orthorhombic Structural Phase Transition at 90 K in the Superconductor $Fe_{1.01}Se$. *Phys. Rev. Lett.*, 103(5):057002, July 2009. doi: 10.1103/PhysRevLett.103.057002. URL http://link.aps.org/doi/10.1103/PhysRevLett.103.057002.

[117] Koichi Momma and Fujio Izumi. VESTA 3 for three-dimensional visualization of crystal, volumetric and morphology data. *Journal of Applied Crystallography*, 44(6):1272–1276, December 2011. ISSN 0021-8898. doi: 10.1107/S0021889811038970. URL http://scripts.iucr.org/cgi-bin/paper?S0021889811038970.

[118] D. Parshall, L. Pintschovius, J. L. Niedziela, J.-P. Castellan, D. Lamago, R. Mittal, Th. Wolf, and D. Reznik. Close correlation between magnetic properties and the soft phonon mode of the structural transition in $BaFe_2As_2$ and $SrFe_2As_2$. *Phys. Rev. B*, 91(13): 134426, April 2015. doi: 10.1103/PhysRevB.91.134426. URL http://link.aps.org/doi/10.1103/PhysRevB.91.134426.

[119] Jennifer L. Niedziela, D. Parshall, K. A. Lokshin, A. S. Sefat, A. Alatas, and T. Egami. Phonon softening near the structural transition in $BaFe_2As_2$ observed by inelastic x-ray scattering. *Phys. Rev. B*, 84 (22):224305, December 2011. doi: 10.1103/PhysRevB.84.224305. URL http://link.aps.org/doi/10.1103/PhysRevB.84.224305.

[120] R. M. Fernandes, L. H. VanBebber, S. Bhattacharya, P. Chandra, V. Keppens, D. Mandrus, M. A. McGuire, B. C. Sales, A. S. Sefat, and J. Schmalian. Effects of Nematic Fluctuations on the Elastic Properties of Iron Arsenide Superconductors. *Phys. Rev. Lett.*, 105(15): 157003, October 2010. doi: 10.1103/PhysRevLett.105.157003. URL http://link.aps.org/doi/10.1103/PhysRevLett.105.157003.

[121] Terutaka Goto, Ryosuke Kurihara, Koji Araki, Keisuke Mitsumoto, Mitsuhiro Akatsu, Yuichi Nemoto, Shunichi Tatematsu, and Masatoshi Sato. Quadrupole Effects of Layered Iron Pnictide Superconductor $Ba(Fe_{0.9}Co_{0.1})_2As_2$. *J. Phys. Soc. Jpn.*, 80(7):073702, June 2011. ISSN 0031-9015. doi: 10.1143/JPSJ.80.073702. URL http://journals.jps.jp/doi/abs/10.1143/JPSJ.80.073702.

[122] Masahito Yoshizawa, Daichi Kimura, Taiji Chiba, Shalamujiang Simayi, Yoshiki Nakanishi, Kunihiro Kihou, Chul-Ho Lee, Akira Iyo, Hiroshi Eisaki, Masamichi Nakajima, and Shin-ichi Uchida. Structural Quantum Criticality and Superconductivity in Iron-Based Superconductor $Ba(Fe_{1-x}Co_x)_2As_2$. *J. Phys. Soc. Jpn.*, 81(2):024604, January 2012. ISSN 0031-9015. doi: 10.1143/JPSJ.81.024604. URL http://journals.jps.jp/doi/abs/10.1143/JPSJ.81.024604.

[123] A.E. Böhmer, P. Burger, F. Hardy, T. Wolf, P. Schweiss, R. Fromknecht, M. Reinecker, W. Schranz, and C. Meingast. Nematic Susceptibility of Hole-Doped and Electron-Doped $BaFe_2As_2$ Iron-Based Superconductors from Shear Modulus Measurements. *Phys. Rev. Lett.*, 112(4):047001, January 2014. doi: 10.1103/PhysRevLett.112.047001. URL http://link.aps.org/doi/10.1103/PhysRevLett.112.047001.

[124] A.E. Böhmer, T. Arai, F. Hardy, T. Hattori, T. Iye, T. Wolf, H.v. Löhneysen, K. Ishida, and C. Meingast. Origin of the Tetragonal-to-Orthorhombic Phase Transition in FeSe: A Combined Thermodynamic and NMR Study of Nematicity. *Phys. Rev. Lett.*, 114(2):027001, January 2015. doi: 10.1103/PhysRevLett.114.027001. URL http://link.aps.org/doi/10.1103/PhysRevLett.114.027001.

[125] B. C. Sales, A. S. Sefat, M. A. McGuire, R. Y. Jin, D. Mandrus, and Y. Mozharivskyj. Bulk superconductivity at 14 K in single crystals of $Fe_{1+y}Te_xSe_{1-x}$. *Phys. Rev. B*, 79(9):094521, March 2009. doi: 10.1103/PhysRevB.79.094521. URL http://link.aps.org/doi/10.1103/PhysRevB.79.094521.

[126] Barry Winn, Uwe Filges, V. Ovidiu Garlea, Melissa Graves-Brook, Mark Hagen, Chenyang Jiang, Michel Kenzelmann, Larry Passell, Stephen M. Shapiro, Xin Tong, and Igor Zaliznyak. Recent progress on HYSPEC, and its polarization analysis capabilities. *EPJ Web of Conferences*, 83:03017, 2015. ISSN 2100-014X. doi: 10.1051/epjconf/20158303017. URL http://www.epj-conferences.org/10.1051/epjconf/20158303017.

[127] J. W. Lynn, Y. Chen, S. Chang, Y. Zhao, S. Chi, W. Ratcliff, B. G. Ueland, and R. W. Fonda. Double Focusing Thermal Triple Axis Spectrometer at the NCNR. *Journal of Research of NIST*, 117:61–79, February 2012. URL http://dx.doi.org/10.6028/jres.117.002.

[128] J. A. Rodriguez, D. M. Adler, P. C. Brand, C. Broholm, J. C. Cook, C. Brocker, R. Hammond, Z. Huang, P. Hundertmark, J. W. Lynn, N. C. Maliszewskyj, J. Moyer, J. Orndorff, D. Pierce, T. D. Pike, G. Scharfstein, S. A. Smee, and R. Vilaseca. MACS—a new high intensity cold neutron spectrometer at NIST. *Meas. Sci. Technol.*, 19

(3):034023, March 2008. ISSN 0957-0233. doi: 10.1088/0957-0233/19/3/034023. URL http://iopscience.iop.org/0957-0233/19/3/034023.

[129] Mildred S. Dresselhaus, G. Dresselhaus, and A. Jorio. *Group Theory: Applications to the Physics of Condensed Matter*. 2008.

[130] David Fobes, Igor A. Zaliznyak, Zhijun Xu, Ruidan Zhong, Genda Gu, John M. Tranquada, Leland Harriger, Deepak Singh, V. Ovidiu Garlea, Mark Lumsden, and Barry Winn. Ferro-Orbital Ordering Transition in Iron Telluride $Fe_{1+y}Te$. *Phys. Rev. Lett.*, 112(18):187202, May 2014. doi: 10.1103/PhysRevLett.112.187202. URL http://link.aps.org/doi/10.1103/PhysRevLett.112.187202.

[131] Despina Louca, K. Horigane, A. Llobet, R. Arita, S. Ji, N. Katayama, S. Konbu, K. Nakamura, T.-Y. Koo, P. Tong, and K. Yamada. Local atomic structure of superconducting $FeSe_{1-x}Te_x$. *Phys. Rev. B*, 81(13): 134524, April 2010. doi: 10.1103/PhysRevB.81.134524. URL http://link.aps.org/doi/10.1103/PhysRevB.81.134524.

[132] B. Keimer, S. A. Kivelson, M. R. Norman, S. Uchida, and J. Zaanen. From quantum matter to high-temperature superconductivity in copper oxides. *Nature*, 518(7538):179–186, February 2015. ISSN 0028-0836. doi: 10.1038/nature14165. URL http://www.nature.com/nature/journal/v518/n7538/full/nature14165.html.

[133] Andrea Damascelli, Zahid Hussain, and Zhi-Xun Shen. Angle-resolved photoemission studies of the cuprate superconductors. *Rev. Mod. Phys.*, 75(2):473–541, April 2003. doi: 10.1103/RevModPhys.75.473. URL http://link.aps.org/doi/10.1103/RevModPhys.75.473.

[134] B. O. Wells, R. J. Birgeneau, F. C. Chou, Y. Endoh, D. C. Johnston, M. A. Kastner, Y. S. Lee, G. Shirane, J. M. Tranquada, and K. Yamada. Intercalation and staging behavior in super-oxygenated La_2CuO_4. *Zeitschrift fr Physik B Condensed Matter*, 100(4):535–545, July 1996. ISSN 0722-3277, 1431-584X. doi: 10.1007/s002570050158. URL http://www.springerlink.com/content/nlhknglw2qegjkaa/.

[135] John M. Tranquada. Neutron Scattering Studies of Antiferromagnetic Correlations in Cuprates. In J. Robert Schrieffer and James S.

Brooks, editors, *Handbook of High-Temperature Superconductivity*, pages 257–298. Springer New York, 2007. ISBN 978-0-387-35071-4 978-0-387-68734-6. URL http://link.springer.com/chapter/10.1007/978-0-387-68734-6_6. DOI: 10.1007/978-0-387-68734-6_6.

[136] R. Coldea, S. M. Hayden, G. Aeppli, T. G. Perring, C. D. Frost, T. E. Mason, S.-W. Cheong, and Z. Fisk. Spin Waves and Electronic Interactions in La_2CuO_4. *Phys. Rev. Lett.*, 86(23):5377–5380, June 2001. doi: 10.1103/PhysRevLett.86.5377. URL http://link.aps.org/doi/10.1103/PhysRevLett.86.5377.

[137] K. Yamada, K. Kurahashi, T. Uefuji, M. Fujita, S. Park, S.-H. Lee, and Y. Endoh. Commensurate Spin Dynamics in the Superconducting State of an Electron-Doped Cuprate Superconductor. *Phys. Rev. Lett.*, 90(13):137004, April 2003. doi: 10.1103/PhysRevLett.90.137004. URL http://link.aps.org/doi/10.1103/PhysRevLett.90.137004.

[138] M. Fujita, S. Kuroshima, M. Matsuda, and K. Yamada. Neutron-scattering study of spin correlations in electron-doped $Pr_{0.89}LaCe_{0.11}CuO_4$ single crystals. *Physica C: Superconductivity*, 392–396, Part 1:130–134, October 2003. ISSN 0921-4534. doi: 10.1016/S0921-4534(03)00750-0. URL http://www.sciencedirect.com/science/article/pii/S0921453403007500.

[139] Stephen D. Wilson, Pengcheng Dai, Shiliang Li, Songxue Chi, H. J. Kang, and J. W. Lynn. Resonance in the electron-doped high-transition-temperature superconductor $Pr_{0.88}LaCe_{0.12}CuO_{4-\delta}$. *Nature*, 442(7098):59–62, July 2006. ISSN 0028-0836. doi: 10.1038/nature04857. URL http://www.nature.com/nature/journal/v442/n7098/abs/nature04857.html.

[140] Y. Sidis, S. Pailhès, B. Keimer, P. Bourges, C. Ulrich, and L. P. Regnault. Magnetic resonant excitations in High-T_c superconductors. *phys. stat. sol. (b)*, 241(6):1204–1210, May 2004. ISSN 1521-3951. doi: 10.1002/pssb.200304498. URL http://onlinelibrary.wiley.com/doi/10.1002/pssb.200304498/abstract.

[141] G. Yu, Y. Li, E. M. Motoyama, and M. Greven. A universal relationship between magnetic resonance and superconducting gap in

unconventional superconductors. *Nat Phys*, 5(12):873–875, December 2009. ISSN 1745-2473. doi: 10.1038/nphys1426. URL http://www.nature.com/nphys/journal/v5/n12/full/nphys1426.html.

[142] N. B. Christensen, D. F. McMorrow, H. M. Rønnow, B. Lake, S. M. Hayden, G. Aeppli, T. G. Perring, M. Mangkorntong, M. Nohara, and H. Takagi. Dispersive Excitations in the High-Temperature Superconductor $La_{2-x}Sr_xCuO_4$. *Phys. Rev. Lett.*, 93(14):147002, September 2004. doi: 10.1103/PhysRevLett.93.147002. URL http://link.aps.org/doi/10.1103/PhysRevLett.93.147002.

[143] Yvan Sidis, Stéphane Pailhès, Vladimir Hinkov, Benoît Fauqué, Clemens Ulrich, Lucia Capogna, Alexandre Ivanov, Louis-Pierre Regnault, Bernhard Keimer, and Philippe Bourges. Inelastic neutron scattering study of spin excitations in the superconducting state of high temperature superconductors. *Comptes Rendus Physique*, 8(7):745–762, September 2007. ISSN 1631-0705. doi: 10.1016/j.crhy.2007.07.003. URL http://www.sciencedirect.com/science/article/pii/S163107050700165X.

[144] Y. Sidis, P. Bourges, H. F. Fong, B. Keimer, L. P. Regnault, J. Bossy, A. Ivanov, B. Hennion, P. Gautier-Picard, G. Collin, D. L. Millius, and I. A. Aksay. Quantum Impurities and the Neutron Resonance Peak in $YBa_2Cu_3O_7$: Ni versus Zn. *Phys. Rev. Lett.*, 84(25):5900–5903, June 2000. doi: 10.1103/PhysRevLett.84.5900. URL http://link.aps.org/doi/10.1103/PhysRevLett.84.5900.

[145] B. Keimer, N. Belk, R. J. Birgeneau, A. Cassanho, C. Y. Chen, M. Greven, M. A. Kastner, A. Aharony, Y. Endoh, R. W. Erwin, and G. Shirane. Magnetic excitations in pure, lightly doped, and weakly metallic La_2CuO_4. *Phys. Rev. B*, 46(21):14034–14053, December 1992. doi: 10.1103/PhysRevB.46.14034. URL http://link.aps.org/doi/10.1103/PhysRevB.46.14034.

[146] J. J. Wagman, D. Parshall, M. B. Stone, A. T. Savici, Y. Zhao, H. A. Dabkowska, and B. D. Gaulin. Quasi-two-dimensional spin and phonon excitations in $La_{1.965}Ba_{0.035}CuO_4$. *Phys. Rev. B*, 91(22):224404, June 2015. doi: 10.1103/PhysRevB.91.224404. URL http://link.aps.org/doi/10.1103/PhysRevB.91.224404.

[147] Zahra Yamani, W. J. L. Buyers, F. Wang, Y.-J. Kim, J.-H. Chung, S. Chang, P. M. Gehring, G. Gasparovic, C. Stock, C. L. Broholm, J. C. Baglo, Ruixing Liang, D. A. Bonn, and W. N. Hardy. Separation of magnetic and superconducting behavior in $YBa_2Cu_3O_{6.33}$ ($t_c = 8.4$ k). *Phys. Rev. B*, 91(13):134427, April 2015. doi: 10.1103/PhysRevB.91.134427. URL http://link.aps.org/doi/10.1103/PhysRevB.91.134427.

[148] Kyoichi Kinoshita, Hiroyuki Shibata, and Tomoaki Yamada. High-pressure synthesis of superconducting $La_{2-x}Ca_{1+x}Cu_2O_{6-x/2+\delta}$. *Physica C: Superconductivity*, 171(5–6):523–527, November 1990. ISSN 0921-4534. doi: 10.1016/0921-4534(90)90267-I. URL http://www.sciencedirect.com/science/article/pii/092145349090267I.

[149] M. Hücker, Young-June Kim, G. D. Gu, J. M. Tranquada, B. D. Gaulin, and J. W. Lynn. Neutron scattering study on $La_{1.9}Ca_{1.1}Cu_2O_{6+\delta}$ and $La_{1.85}Sr_{0.15}CaCu_2O_{6+\delta}$. *Phys. Rev. B*, 71(9):094510, March 2005. doi: 10.1103/PhysRevB.71.094510. URL http://link.aps.org/doi/10.1103/PhysRevB.71.094510.

[150] C. Ulrich, S. Kondo, M. Reehuis, H. He, C. Bernhard, C. Niedermayer, F. Bourée, P. Bourges, M. Ohl, H. M. Rønnow, H. Takagi, and B. Keimer. Structural and magnetic instabilities of $La_{2-x}Sr_xCaCu_2O_6$. *Phys. Rev. B*, 65(22):220507, May 2002. doi: 10.1103/PhysRevB.65.220507. URL http://link.aps.org/doi/10.1103/PhysRevB.65.220507.

[151] G.D. Gu, M. Hücker, Y.-J. Kim, J.M. Tranquada, H. Dabkowska, G.M. Luke, T. Timusk, B.D. Gaulin, Q. Li, and A.R. Moodenbaugh. Crystal growth and superconductivity of $(La_{1-x}Ca_x)_2CaCu_2O_{6+\delta}$. *Journal of Physics and Chemistry of Solids*, 67(1–3):431–434, March 2006. ISSN 0022-3697. doi: 10.1016/j.jpcs.2005.10.153. URL http://www.sciencedirect.com/science/article/pii/S0022369705004622.

[152] M. B. Stone, J. L. Niedziela, D. L. Abernathy, L. DeBeer-Schmitt, G. Ehlers, O. Garlea, G. E. Granroth, M. Graves-Brook, A. I. Kolesnikov, A. Podlesnyak, and B. Winn. A comparison of four direct geometry time-of-flight spectrometers at the Spallation Neutron Source. *Rev. Sci. Instrum.*, 85(4):045113, April 2014. ISSN 0034-6748,

1089-7623. doi: 10.1063/1.4870050. URL http://scitation.aip.org/content/aip/journal/rsi/85/4/10.1063/1.4870050.

[153] Hefei Hu, Yimei Zhu, Xiaoya Shi, Qiang Li, Ruidan Zhong, John A. Schneeloch, Genda Gu, John M. Tranquada, and Simon J. L. Billinge. Nanoscale coherent intergrowthlike defects in a crystal of $La_{1.9}Ca_{1.1}Cu_2O_{6+\delta}$ made superconducting by high-pressure oxygen annealing. *Phys. Rev. B*, 90(13):134518, October 2014. doi: 10.1103/PhysRevB.90.134518. URL http://link.aps.org/doi/10.1103/PhysRevB.90.134518.

[154] J. J. Wagman, G. Van Gastel, K. A. Ross, Z. Yamani, Y. Zhao, Y. Qiu, J. R. D. Copley, A. B. Kallin, E. Mazurek, J. P. Carlo, H. A. Dabkowska, and B. D. Gaulin. Two-dimensional incommensurate and three-dimensional commensurate magnetic order and fluctuations in $La_{2-x}Ba_xCuO_4$. *Phys. Rev. B*, 88(1):014412, July 2013. doi: 10.1103/PhysRevB.88.014412. URL http://link.aps.org/doi/10.1103/PhysRevB.88.014412.

[155] M. K. Chan, C. J. Dorow, L. Mangin-Thro, Y. Tang, Y. Ge, M. J. Veit, G. Yu, X. Zhao, A. D. Christianson, J. T. Park, Y. Sidis, P. Steffens, D. L. Abernathy, P. Bourges, and M. Greven. Commensurate antiferromagnetic excitations as a signature of the pseudogap in the tetragonal high-T_c cuprate $HgBa_2CuO_{4+\delta}$. *Nat Commun*, 7:10819, March 2016. doi: 10.1038/ncomms10819. URL http://www.nature.com/ncomms/2016/160304/ncomms10819/full/ncomms10819.html.

[156] S. Shamoto, M. Sato, J. M. Tranquada, B. J. Sternlieb, and G. Shirane. Neutron-scattering study of antiferromagnetism in $YBa_2Cu_3O_{6.15}$. *Phys. Rev. B*, 48(18):13817–13825, November 1993. doi: 10.1103/PhysRevB.48.13817. URL http://link.aps.org/doi/10.1103/PhysRevB.48.13817.

[157] Hashini E. Mohottala, Barrett O. Wells, Joseph I. Budnick, William A. Hines, Christof Niedermayer, Linda Udby, Christian Bernhard, Arnold R. Moodenbaugh, and Fang-Cheng Chou. Phase separation in superoxygenated $La_{2-x}Sr_xCuO_{4+y}$. *Nat Mater*, 5(5):377–382, May 2006. ISSN 1476-1122. doi: 10.1038/nmat1633. URL http://www.nature.com/nmat/journal/v5/n5/full/nmat1633.html.

[158] Y. Takeda, K. Yoshikawa, O. Yamamoto, and M. Takano. Superconductivity of $La_{2-x}Nd_xCuO_{4+z}$ prepared under high oxygen pressure: Suppression of the phase separation seen in La_2CuO_{4+z}. *Journal of Solid State Chemistry*, 92(1):241–246, May 1991. ISSN 0022-4596. doi: 10.1016/0022-4596(91)90264-I. URL http://www.sciencedirect.com/science/article/pii/002245969190264I.

[159] Y. Takeda, A. Sato, K. Yoshikawa, N. Imanishi, O. Yamamoto, M. Takano, Z. Hiroi, and Y. Bando. Superconductivity of $La_{2-x}A_xCuO_{4+\delta}$ (A=Nd and Bi) prepared under high oxygen pressure. *Physica C: Superconductivity*, 185:603–604, December 1991. ISSN 0921-4534. doi: 10.1016/0921-4534(91)92104-J. URL http://www.sciencedirect.com/science/article/pii/092145349192104J.

[160] Zenji Hiroi, Mikio Takano, Yoshichika Bando, Atsushi Sato, and Yasuo Takeda. Superconducting properties of $La_{2-x}Bi_xCuO_{4+\delta}$. *Phys. Rev. B*, 46(22):14857–14860, December 1992. doi: 10.1103/PhysRevB.46.14857. URL http://link.aps.org/doi/10.1103/PhysRevB.46.14857.

[161] John A. Schneeloch, Zhijun Xu, B. Winn, C. Stock, P. M. Gehring, R. J. Birgeneau, and Guangyong Xu. Phonon coupling to dynamic short-range polar order in a relaxor ferroelectric near the morphotropic phase boundary. *Phys. Rev. B*, 92(21):214302, December 2015. doi: 10.1103/PhysRevB.92.214302. URL http://link.aps.org/doi/10.1103/PhysRevB.92.214302.

[162] Kenji Uchino. *Piezoelectric Actuators and Ultrasonic Motors*. Springer Science & Business Media, November 1996. ISBN 978-0-7923-9811-0.

[163] Robert F. Service. Shape-Changing Crystals Get Shiftier. *Science*, 275(5308):1878–1878, March 1997. ISSN 0036-8075, 1095-9203. doi: 10.1126/science.275.5308.1878. URL http://www.sciencemag.org/content/275/5308/1878.

[164] Charles Kittel. *Introduction to Solid State Physics*. John Wiley And Sons, United States of America, 8th edition, 2005.

[165] Neil W. Ashcroft and N. David Mermin. *Solid State Physics*. Thomson Learning, United States of America, 1976.

[166] George A Samara. The relaxational properties of compositionally disordered ABO_3 perovskites. *Journal of Physics: Condensed Matter*, 15 (9):R367–R411, March 2003. ISSN 0953-8984. doi: 10.1088/0953-8984/15/9/202. URL http://iopscience.iop.org/0953-8984/15/9/202.

[167] K. Binder and A. P. Young. Spin glasses: Experimental facts, theoretical concepts, and open questions. *Rev. Mod. Phys.*, 58(4):801–976, October 1986. doi: 10.1103/RevModPhys.58.801. URL http://link.aps.org/doi/10.1103/RevModPhys.58.801.

[168] B. Noheda, D. E. Cox, G. Shirane, J. Gao, and Z.-G. Ye. Phase diagram of the ferroelectric relaxor $(1-x)PbMg_{1/3}Nb_{2/3}O_3$-$xPbTiO_3$. *Phys. Rev. B*, 66(5):054104, August 2002. doi: 10.1103/PhysRevB.66.054104. URL http://link.aps.org/doi/10.1103/PhysRevB.66.054104.

[169] O. Noblanc, P. Gaucher, and G. Calvarin. Structural and dielectric studies of $Pb(Mg_{1/3}Nb_{2/3})O_3$–$PbTiO_3$ ferroelectric solid solutions around the morphotropic boundary. *Journal of Applied Physics*, 79 (8):4291–4297, April 1996. ISSN 0021-8979, 1089-7550. doi: 10.1063/1.361865. URL http://scitation.aip.org/content/aip/journal/jap/79/8/10.1063/1.361865.

[170] P. K Davies and M. A Akbas. Chemical order in PMN-related relaxors: structure, stability, modification, and impact on properties. *Journal of Physics and Chemistry of Solids*, 61(2):159–166, February 2000. ISSN 0022-3697. doi: 10.1016/S0022-3697(99)00275-9. URL http://www.sciencedirect.com/science/article/pii/S0022369799002759.

[171] Mehmet A. Akbas and Peter K. Davies. Domain Growth in $Pb(Mg_{1/3}Ta_{2/3})O_3$ Perovskite Relaxor Ferroelectric Oxides. *Journal of the American Ceramic Society*, 80(11):2933–2936, November 1997. ISSN 1551-2916. doi: 10.1111/j.1151-2916.1997.tb03214.x. URL http://onlinelibrary.wiley.com/doi/10.1111/j.1151-2916.1997.tb03214.x/abstract.

[172] N. Setter and L. E. Cross. The role of B-site cation disorder in diffuse phase transition behavior of perovskite ferroelectrics. *Journal of Applied Physics*, 51(8):4356–4360, August 1980. ISSN 0021-8979, 1089-7550. doi: 10.1063/1.328296. URL http://scitation.aip.org/

content/aip/journal/jap/51/8/10.1063/1.328296;jsessionid=yQ16rAP5qTgMtRU89QZy74Ea.x-aip-live-03.

[173] D. M. Fanning, I. K. Robinson, S. T. Jung, E. V. Colla, D. D. Viehland, and D. A. Payne. Superstructure ordering in lanthanum-doped lead magnesium niobate. *Journal of Applied Physics*, 87(2): 840–848, January 2000. ISSN 0021-8979, 1089-7550. doi: 10.1063/1.371951. URL http://scitation.aip.org/content/aip/journal/jap/87/2/10.1063/1.371951.

[174] David Michael Fanning. *Structure property relations in ferroelectric materials*. PhD thesis, University of Illinois at Urbana-Champaign, 2000. URL http://adsabs.harvard.edu/abs/2000PhDT.....58F.

[175] Abdel-Baset M. A. Ibrahim, Rajan Murgan, Mohd Kamil Abd Rahman, and Junaidah Osm. Morphotropic Phase Boundary in Ferroelectric Materials. In Mickal Lallart, editor, *Ferroelectrics - Physical Effects*. InTech, August 2011. ISBN 978-953-307-453-5. URL http://www.intechopen.com/books/ferroelectrics-physical-effects/morphotropic-phase-boundary-in-ferroelectric-materials.

[176] R. A. Cowley, S. N. Gvasaliya, S. G. Lushnikov, B. Roessli, and G. M. Rotaru. Relaxing with relaxors: a review of relaxor ferroelectrics. *Adv. Phys.*, 60(2):229–327, 2011. ISSN 0001-8732. doi: 10.1080/00018732.2011.555385. URL http://dx.doi.org/10.1080/00018732.2011.555385.

[177] B. Jaffe, R. S. Roth, and S. Marzullo. Piezoelectric Properties of Lead ZirconateLead Titanate SolidSolution Ceramics. *Journal of Applied Physics*, 25(6):809–810, June 1954. ISSN 0021-8979, 1089-7550. doi: 10.1063/1.1721741. URL http://scitation.aip.org/content/aip/journal/jap/25/6/10.1063/1.1721741.

[178] D. E. Cox, B. Noheda, G. Shirane, Y. Uesu, K. Fujishiro, and Y. Yamada. Universal phase diagram for high-piezoelectric perovskite systems. *Appl. Phys. Lett.*, 79(3):400–402, July 2001. ISSN 0003-6951, 1077-3118. doi: 10.1063/1.1384475. URL http://scitation.aip.org/content/aip/journal/apl/79/3/10.1063/1.1384475.

[179] L. E. Cross. Relaxor Ferroelectrics. In *Piezoelectricity*, number 114 in Springer Series in Materials Science, pages 131–155. Springer Berlin Heidelberg, January 2008. ISBN 978-3-540-68680-4 978-3-540-68683-5. URL http://link.springer.com/chapter/10.1007/978-3-540-68683-5_5.

[180] Guangyong Xu, D. Viehland, J. F. Li, P. M. Gehring, and G. Shirane. Evidence of decoupled lattice distortion and ferroelectric polarization in the relaxor system PMN-xPT. *Phys. Rev. B*, 68(21):212410, December 2003. doi: 10.1103/PhysRevB.68.212410. URL http://link.aps.org/doi/10.1103/PhysRevB.68.212410.

[181] R. Sommer, N. K. Yushin, and J. J. van der Klink. Polar metastability and an electric-field-induced phase transition in the disordered perovskite $Pb(Mg_{1/3}Nb_{2/3})O_3$. *Phys. Rev. B*, 48(18):13230–13237, November 1993. doi: 10.1103/PhysRevB.48.13230. URL http://link.aps.org/doi/10.1103/PhysRevB.48.13230.

[182] Hidehiro Ohwa, Makoto Iwata, Hiroshi Orihara, Naohiko Yasuda, and Yoshihiro Ishibashi. Raman Scattering in (1-x)$Pb(Mg_{1/3}Nb_{2/3})O_3$–$x PbTiO_3$. *J. Phys. Soc. Jpn.*, 70(10):3149–3154, October 2001. ISSN 0031-9015. doi: 10.1143/JPSJ.70.3149. URL http://journals.jps.jp/doi/abs/10.1143/JPSJ.70.3149.

[183] M. Matsuura, K. Hirota, P. M. Gehring, Z.-G. Ye, W. Chen, and G. Shirane. Composition dependence of the diffuse scattering in the relaxor ferroelectric compound $(1x)Pb(Mg_{1/3}Nb_{2/3}O_3$-$xPbTiO_3$ (0x0.40). *Phys. Rev. B*, 74(14):144107, October 2006. doi: 10.1103/PhysRevB.74.144107. URL http://link.aps.org/doi/10.1103/PhysRevB.74.144107.

[184] Gerald Burns and F. H. Dacol. Glassy polarization behavior in ferroelectric compounds $Pb(Mg_{1/3}Nb_{2/3})O_3$ and $Pb(Zn_{1/3}Nb_{2/3})O_3$. *Solid State Communications*, 48(10):853–856, December 1983. ISSN 0038-1098. doi: 10.1016/0038-1098(83)90132-1. URL http://www.sciencedirect.com/science/article/pii/0038109883901321.

[185] P. M. Gehring, H. Hiraka, C. Stock, S.-H. Lee, W. Chen, Z.-G. Ye, S. B. Vakhrushev, and Z. Chowdhuri. Reassessment of the Burns temperature and its relationship to the diffuse scattering, lattice dynamics,

and thermal expansion in relaxor $Pb(Mg_{1/3}Nb_{2/3})O_3$. *Phys. Rev. B*, 79(22):224109, June 2009. doi: 10.1103/PhysRevB.79.224109. URL http://link.aps.org/doi/10.1103/PhysRevB.79.224109.

[186] J. D. Axe, J. Harada, and G. Shirane. Anomalous Acoustic Dispersion in Centrosymmetric Crystals with Soft Optic Phonons. *Phys. Rev. B*, 1(3):1227–1234, February 1970. doi: 10.1103/PhysRevB.1.1227. URL http://link.aps.org/doi/10.1103/PhysRevB.1.1227.

[187] K. Hirota, Z.-G. Ye, S. Wakimoto, P. Gehring, and G. Shirane. Neutron diffuse scattering from polar nanoregions in the relaxor $Pb(Mg_{1/3}Nb_{2/3})O_3$. *Phys. Rev. B*, 65(10):104105, February 2002. doi: 10.1103/PhysRevB.65.104105. URL http://link.aps.org/doi/10.1103/PhysRevB.65.104105.

[188] Wenwei Ge, Christopher P. Devreugd, D. Phelan, Qinhui Zhang, Muhtar Ahart, Jiefang Li, Haosu Luo, Lynn A. Boatner, Dwight Viehland, and Peter M. Gehring. Lead-free and lead-based ABO_3 perovskite relaxors with mixed-valence A-site and B-site disorder: Comparative neutron scattering structural study of $(Na_{1/2}Bi_{1/2})TiO_3$ and $Pb(Mg_{1/3}Nb_{2/3})O_3$. *Phys. Rev. B*, 88(17):174115, November 2013. doi: 10.1103/PhysRevB.88.174115. URL http://link.aps.org/doi/10.1103/PhysRevB.88.174115.

[189] Daniel Phelan, Christopher Stock, Jose A. Rodriguez-Rivera, Songxue Chi, Juscelino Leão, Xifa Long, Yujuan Xie, Alexei A. Bokov, Zuo-Guang Ye, Panchapakesan Ganesh, and Peter M. Gehring. Role of random electric fields in relaxors. *PNAS*, 111(5):1754–1759, February 2014. ISSN 0027-8424, 1091-6490. doi: 10.1073/pnas.1314780111. URL http://www.pnas.org/content/111/5/1754.

[190] C. Stock, H. Luo, D. Viehland, J. F. Li, I. P. Swainson, R. J. Birgeneau, and G. Shirane. Strong Influence of the Diffuse Component on the Lattice Dynamics in $Pb(Mg_{1/3}Nb_{2/3})O_3$. *J. Phys. Soc. Jpn.*, 74(11):3002–3010, August 2005. doi: 10.1143/JPSJ.74.3002. URL http://jpsj.ipap.jp/link?JPSJ/74/3002/.

[191] K. H. Michel and J. Naudts. Dynamics of translations and rotations in molecular crystals. *The Journal of Chemical Physics*, 68 (1):216–228, 1978. ISSN 0021-9606, 1089-7690. doi: 10.1063/1.

435485. URL http://scitation.aip.org/content/aip/journal/jcp/68/1/10.1063/1.435485.

[192] Jean-Michel Kiat, Yoshiaki Uesu, Brahim Dkhil, Masaaki Matsuda, Charlotte Malibert, and Gilbert Calvarin. Monoclinic structure of unpoled morphotropic high piezoelectric PMN-PT and PZN-PT compounds. *Phys. Rev. B*, 65(6):064106, January 2002. doi: 10.1103/PhysRevB.65.064106. URL http://link.aps.org/doi/10.1103/PhysRevB.65.064106.

[193] Jun Kuwata, Kenji Uchino, and Shoichiro Nomura. Phase transitions in the $Pb(Zn_{1/3}Nb_{2/3})O_3$-$PbTiO_3$ system. *Ferroelectrics*, 37(1):579–582, October 1981. ISSN 0015-0193. doi: 10.1080/00150198108223490. URL http://dx.doi.org/10.1080/00150198108223490.

[194] Jun Kuwata, Kenji Uchino, and Shoichiro Nomura. Dielectric and Piezoelectric Properties of $0.91Pb(Zn_{1/3}Nb_{2/3})O_3$-$0.09PbTiO_3$ Single Crystals. *Jpn. J. Appl. Phys.*, 21(9R):1298, September 1982. ISSN 1347-4065. doi: 10.1143/JJAP.21.1298. URL http://iopscience.iop.org/1347-4065/21/9R/1298.

[195] H. Hiraka, S.-H. Lee, P. M. Gehring, Guangyong Xu, and G. Shirane. Cold neutron study on the diffuse scattering and phonon excitations in the relaxor $Pb(Mg_{1/3}Nb_{2/3})O_3$. *Phys. Rev. B*, 70(18):184105, November 2004. doi: 10.1103/PhysRevB.70.184105. URL http://link.aps.org/doi/10.1103/PhysRevB.70.184105.

[196] H. You and Q. M. Zhang. Diffuse X-Ray Scattering Study of Lead Magnesium Niobate Single Crystals. *Phys. Rev. Lett.*, 79(20):3950–3953, November 1997. doi: 10.1103/PhysRevLett.79.3950. URL http://link.aps.org/doi/10.1103/PhysRevLett.79.3950.

[197] Naohisa Takesue, Yasuhiko Fujii, and Hoydoo You. X-ray diffuse scattering study on ionic-pair displacement correlations in relaxor lead magnesium niobate. *Phys. Rev. B*, 64(18):184112, October 2001. doi: 10.1103/PhysRevB.64.184112. URL http://link.aps.org/doi/10.1103/PhysRevB.64.184112.

[198] Guangyong Xu, Z. Zhong, H. Hiraka, and G. Shirane. Three-dimensional mapping of diffuse scattering in $Pb(Zn_{1/3}Nb_{2/3})O_3$-$x PbTiO_3$. *Phys. Rev. B*, 70(17):174109, November 2004. doi:

10.1103/PhysRevB.70.174109. URL http://link.aps.org/doi/10.1103/PhysRevB.70.174109.

[199] D. La-Orauttapong, J. Toulouse, J. L. Robertson, and Z.-G. Ye. Diffuse neutron scattering study of a disordered complex perovskite $Pb(Zn_{1/3}Nb_{2/3})O_3$ crystal. *Phys. Rev. B*, 64(21):212101, November 2001. doi: 10.1103/PhysRevB.64.212101. URL http://link.aps.org/doi/10.1103/PhysRevB.64.212101.

[200] D. La-Orauttapong, J. Toulouse, Z.-G. Ye, W. Chen, R. Erwin, and J. L. Robertson. Neutron scattering study of the relaxor ferroelectric $(1-x)Pb(Zn_{1/3}Nb_{2/3})O_3$-$xPbTiO_3$. *Phys. Rev. B*, 67(13):134110, April 2003. doi: 10.1103/PhysRevB.67.134110. URL http://link.aps.org/doi/10.1103/PhysRevB.67.134110.

[201] B. Dkhil, J. M. Kiat, G. Calvarin, G. Baldinozzi, S. B. Vakhrushev, and E. Suard. Local and long range polar order in the relaxor-ferroelectric compounds $PbMg_{1/3}Nb_{2/3}O_3$ and $PbMg_{0.3}Nb_{0.6}Ti_{0.1}O_3$. *Phys. Rev. B*, 65(2):024104, December 2001. doi: 10.1103/PhysRevB.65.024104. URL http://link.aps.org/doi/10.1103/PhysRevB.65.024104.

[202] S. B. Vakhrushev, A. A. Naberezhnov, N. M. Okuneva, and B. N. Savenko. *Phys. Solid State*, 37:1993, 1995.

[203] J. Hlinka, S. Kamba, J. Petzelt, J. Kulda, C. A. Randall, and S. J. Zhang. Diffuse scattering in $Pb(Zn_{1/3}Nb_{2/3})O_3$ with 8% $PbTiO_3$ by quasi-elastic neutron scattering. *J. Phys.: Condens. Matter*, 15(24): 4249, June 2003. ISSN 0953-8984. doi: 10.1088/0953-8984/15/24/318. URL http://iopscience.iop.org/0953-8984/15/24/318.

[204] Sergey Vakhrushev, Alexandre Ivanov, and Jiri Kulda. Diffuse neutron scattering in relaxor ferroelectric $PbMg_{1/3}Nb_{2/3}o_3$. *Phys. Chem. Chem. Phys.*, 7(11):2340–2345, May 2005. ISSN 1463-9084. doi: 10.1039/B416454G. URL http://pubs.rsc.org/en/content/articlelanding/2005/cp/b416454g.

[205] Guangyong Xu, G. Shirane, J. R. D. Copley, and P. M. Gehring. Neutron elastic diffuse scattering study of $Pb(Mg_{1/3}Nb_{2/3})O_3$. *Phys. Rev. B*, 69(6):064112, February 2004. doi: 10.1103/PhysRevB.69.064112. URL http://link.aps.org/doi/10.1103/PhysRevB.69.064112.

[206] Zhijun Xu, Jinsheng Wen, Guangyong Xu, C. Stock, J. S. Gardner, and P. M. Gehring. Two-component model of the neutron diffuse scattering in the relaxor ferroelectric PZN-4.5%PT. *Phys. Rev. B*, 82(13):134124, October 2010. doi: 10.1103/PhysRevB.82.134124. URL `http://link.aps.org/doi/10.1103/PhysRevB.82.134124`.

[207] Guangyong Xu, P. M. Gehring, and G. Shirane. Persistence and memory of polar nanoregions in a ferroelectric relaxor under an electric field. *Phys. Rev. B*, 72(21):214106, December 2005. doi: 10.1103/PhysRevB.72.214106. URL `http://link.aps.org/doi/10.1103/PhysRevB.72.214106`.

[208] Guangyong Xu, P. M. Gehring, and G. Shirane. Coexistence and competition of local- and long-range polar orders in a ferroelectric relaxor. *Phys. Rev. B*, 74(10):104110, September 2006. doi: 10.1103/PhysRevB.74.104110. URL `http://link.aps.org/doi/10.1103/PhysRevB.74.104110`.

[209] Guangyong Xu, Z. Zhong, Y. Bing, Z.-G. Ye, and G. Shirane. Electric-field-induced redistribution of polar nano-regions in a relaxor ferroelectric. *Nat. Mater.*, 5(2):134–140, February 2006. ISSN 1476-1122. doi: 10.1038/nmat1560. URL `http://www.nature.com/nmat/journal/v5/n2/abs/nmat1560.html`.

[210] C. Stock, Guangyong Xu, P. M. Gehring, H. Luo, X. Zhao, H. Cao, J. F. Li, D. Viehland, and G. Shirane. Neutron and x-ray diffraction study of cubic [111] field-cooled $Pb(Mg_{1/3}Nb_{2/3})O_3$. *Phys. Rev. B*, 76(6):064122, August 2007. doi: 10.1103/PhysRevB.76.064122. URL `http://link.aps.org/doi/10.1103/PhysRevB.76.064122`.

[211] Jinsheng Wen, Guangyong Xu, C. Stock, and P. M. Gehring. Response of polar nanoregions in $68\%Pb(Mg_{1/3}Nb_{2/3})O_3$-$32\%PbTiO_3$ to a [001] electric field. *Appl. Phys. Lett.*, 93(8):082901, August 2008. ISSN 0003-6951, 1077-3118. doi: 10.1063/1.2959077. URL `http://scitation.aip.org/content/aip/journal/apl/93/8/10.1063/1.2959077`.

[212] P. M. Gehring, K. Ohwada, and G. Shirane. Electric-field effects on the diffuse scattering in $PbZn_{1/3}Nb_{2/3}O_3$ doped with 8% $PbTiO_3$. *Phys. Rev. B*, 70(1):014110, July 2004. doi: 10.1103/PhysRevB.70.014110. URL `http://link.aps.org/doi/10.1103/PhysRevB.70.014110`.

[213] O. Arnold, J. C. Bilheux, J. M. Borreguero, A. Buts, S. I. Campbell, L. Chapon, M. Doucet, N. Draper, R. Ferraz Leal, M. A. Gigg, V. E. Lynch, A. Markvardsen, D. J. Mikkelson, R. L. Mikkelson, R. Miller, K. Palmen, P. Parker, G. Passos, T. G. Perring, P. F. Peterson, S. Ren, M. A. Reuter, A. T. Savici, J. W. Taylor, R. J. Taylor, R. Tolchenov, W. Zhou, and J. Zikovsky. Mantid—Data analysis and visualization package for neutron scattering and SR experiments. *Nucl. Instr. Meth. Phys. Res. Sect. A*, 764:156–166, November 2014. ISSN 0168-9002. doi: 10.1016/j.nima.2014.07.029. URL `http://www.sciencedirect.com/science/article/pii/S0168900214008729`.

[214] P. M. Gehring, S.-E. Park, and G. Shirane. Soft Phonon Anomalies in the Relaxor Ferroelectric $Pb(Zn_{1/3}Nb_{2/3})_{0.92}Ti_{0.08}O_3$. *Phys. Rev. Lett.*, 84(22):5216–5219, May 2000. doi: 10.1103/PhysRevLett.84.5216. URL `http://link.aps.org/doi/10.1103/PhysRevLett.84.5216`.

[215] P. M. Gehring, S. B. Vakhrushev, and G. Shirane. Soft mode anomalies in the perovskite relaxor $Pb(Mg_{1/3}Nb_{2/3})O_3$. In *AIP Conference Proceedings*, volume 535, pages 314–322. AIP Publishing, September 2000. doi: 10.1063/1.1324469. URL `http://scitation.aip.org/content/aip/proceeding/aipcp/10.1063/1.1324469`.

[216] P. M. Gehring, S.-E. Park, and G. Shirane. Dynamical effects of the nanometer-sized polarized domains in $Pb(Zn_{1/3}Nb_{2/3})O_3$. *Phys. Rev. B*, 63(22):224109, May 2001. doi: 10.1103/PhysRevB.63.224109. URL `http://link.aps.org/doi/10.1103/PhysRevB.63.224109`.

[217] P. M. Gehring, S. Wakimoto, Z.-G. Ye, and G. Shirane. Soft Mode Dynamics above and below the Burns Temperature in the Relaxor $Pb(Mg_{1/3}Nb_{2/3})O_3$. *Phys. Rev. Lett.*, 87(27):277601, December 2001. doi: 10.1103/PhysRevLett.87.277601. URL `http://link.aps.org/doi/10.1103/PhysRevLett.87.277601`.

[218] D. La-Orauttapong, B. Noheda, Z.-G. Ye, P. M. Gehring, J. Toulouse, D. E. Cox, and G. Shirane. Phase diagram of the relaxor ferroelectric $(1-x)Pb(Zn_{1/3}Nb_{2/3})O_3$-$xPbTiO_3$. *Phys. Rev. B*, 65(14):144101, March 2002. doi: 10.1103/PhysRevB.65.144101. URL `http://link.aps.org/doi/10.1103/PhysRevB.65.144101`.

[219] T. Y. Koo, P. M. Gehring, G. Shirane, V. Kiryukhin, S.-G. Lee, and S-W. Cheong. Anomalous transverse acoustic phonon broadening in the relaxor ferroelectric $Pb(Mg_{1/3}Nb_{2/3})_{0.8}Ti_{0.2}O_3$. *Phys. Rev. B*, 65(14): 144113, April 2002. doi: 10.1103/PhysRevB.65.144113. URL `http://link.aps.org/doi/10.1103/PhysRevB.65.144113`.

[220] J. Hlinka, S. Kamba, J. Petzelt, J. Kulda, C. A. Randall, and S. J. Zhang. Origin of the "Waterfall" Effect in Phonon Dispersion of Relaxor Perovskites. *Phys. Rev. Lett.*, 91(10):107602, September 2003. doi: 10.1103/PhysRevLett.91.107602. URL `http://link.aps.org/doi/10.1103/PhysRevLett.91.107602`.

[221] C. Stock, D. Ellis, I. P. Swainson, Guangyong Xu, H. Hiraka, Z. Zhong, H. Luo, X. Zhao, D. Viehland, R. J. Birgeneau, and G. Shirane. Damped soft phonons and diffuse scattering in $40\%Pb(Mg_{1/3}Nb_{2/3})O_3$-$60\%PbTiO_3$. *Phys. Rev. B*, 73(6):064107, February 2006. doi: 10.1103/PhysRevB.73.064107. URL `http://link.aps.org/doi/10.1103/PhysRevB.73.064107`.

[222] J. M. Worlock and P. A. Fleury. Electric Field Dependence of Optical-Phonon Frequencies. *Phys. Rev. Lett.*, 19(20):1176–1179, November 1967. doi: 10.1103/PhysRevLett.19.1176. URL `http://link.aps.org/doi/10.1103/PhysRevLett.19.1176`.

[223] Manabu Watanabe, Yagi Toshirou, and Yamaguchi Masashi. Brillouin Scattering Study of Quantum Paraelectric $SrTiO_3$ under Electric Field. *J. Korean Phys. Soc.*, 32:S556–S558, February 1998.

[224] N. Boccara. Electric field influence on soft phonon modes frequencies in ferroelectrics. *Solid State Commun.*, 6(4):211–213, April 1968. ISSN 0038-1098. doi: 10.1016/0038-1098(68)90037-9. URL `http://www.sciencedirect.com/science/article/pii/0038109868900379`.

[225] C. Stock, P. M. Gehring, H. Hiraka, I. Swainson, Guangyong Xu, Z.-G. Ye, H. Luo, J.-F. Li, and D. Viehland. Evidence for anisotropic polar nanoregions in relaxor $Pb(Mg_{1/3}Nb_{2/3})O_3$: A neutron study of the elastic constants and anomalous TA phonon damping in PMN. *Phys. Rev. B*, 86(10):104108, September 2012. doi: 10.1103/PhysRevB.86.104108. URL `http://link.aps.org/doi/10.1103/PhysRevB.86.104108`.

[226] B. E. Vugmeister and M. D. Glinchuk. Dipole glass and ferroelectricity in random-site electric dipole systems. *Rev. Mod. Phys.*, 62(4):993–1026, October 1990. doi: 10.1103/RevModPhys.62.993. URL http://link.aps.org/doi/10.1103/RevModPhys.62.993.

[227] V. Westphal, W. Kleemann, and M. D. Glinchuk. Diffuse phase transitions and random-field-induced domain states of the "relaxor" ferroelectric $PbMg_{1/3}Nb_{2/3}O_3$. *Phys. Rev. Lett.*, 68(6):847–850, February 1992. doi: 10.1103/PhysRevLett.68.847. URL http://link.aps.org/doi/10.1103/PhysRevLett.68.847.

[228] C. Stock, R. J. Birgeneau, S. Wakimoto, J. S. Gardner, W. Chen, Z.-G. Ye, and G. Shirane. Universal static and dynamic properties of the structural transition in $Pb(Zn_{1/3}Nb_{2/3})O_3$. *Phys. Rev. B*, 69(9):094104, March 2004. doi: 10.1103/PhysRevB.69.094104. URL http://link.aps.org/doi/10.1103/PhysRevB.69.094104.

[229] Silvia Tinte, B. P. Burton, Eric Cockayne, and U. V. Waghmare. Origin of the Relaxor State in $Pb(B_xB'_{1-x})O_3$ Perovskites. *Phys. Rev. Lett.*, 97(13):137601, September 2006. doi: 10.1103/PhysRevLett.97.137601. URL http://link.aps.org/doi/10.1103/PhysRevLett.97.137601.

[230] R. Pirc and R. Blinc. Spherical random-bond–random-field model of relaxor ferroelectrics. *Phys. Rev. B*, 60(19):13470–13478, November 1999. doi: 10.1103/PhysRevB.60.13470. URL http://link.aps.org/doi/10.1103/PhysRevB.60.13470.

[231] Zhijun Xu, Jinsheng Wen, E. Mamontov, C. Stock, P. M. Gehring, and Guangyong Xu. Freezing of the local dynamics in the relaxor ferroelectric $[Pb(Zn_{1/3}Nb_{2/3})O_3]_{0.955}[PbTiO_3]_{0.045}$. *Phys. Rev. B*, 86(14):144106, October 2012. doi: 10.1103/PhysRevB.86.144106. URL http://link.aps.org/doi/10.1103/PhysRevB.86.144106.

[232] C. Stock, L. Van Eijck, P. Fouquet, M. Maccarini, P. M. Gehring, Guangyong Xu, H. Luo, X. Zhao, J.-F. Li, and D. Viehland. Interplay between static and dynamic polar correlations in relaxor $Pb(Mg_{1/3}Nb_{2/3})O_3$. *Phys. Rev. B*, 81(14):144127, April 2010. doi: 10.1103/PhysRevB.81.144127. URL http://link.aps.org/doi/10.1103/PhysRevB.81.144127.

[233] B. E. Vugmeister. Polarization dynamics and formation of polar nanoregions in relaxor ferroelectrics. *Phys. Rev. B*, 73(17):174117, May 2006. doi: 10.1103/PhysRevB.73.174117. URL http://link.aps.org/doi/10.1103/PhysRevB.73.174117.

[234] R. Pirc, R. Blinc, and V. Bobnar. Dynamics of relaxor ferroelectrics. *Phys. Rev. B*, 63(5):054203, January 2001. doi: 10.1103/PhysRevB.63.054203. URL http://link.aps.org/doi/10.1103/PhysRevB.63.054203.

[235] Yoshihiro Kuroiwa, Shinobu Aoyagi, Akikatsu Sawada, Jimpei Harada, Eiji Nishibori, Masaki Takata, and Makoto Sakata. Evidence for Pb-O Covalency in Tetragonal $PbTiO_3$. *Phys. Rev. Lett.*, 87(21):217601, November 2001. doi: 10.1103/PhysRevLett.87.217601. URL http://link.aps.org/doi/10.1103/PhysRevLett.87.217601.

[236] Jun-ichi Okamoto, Carlos J. Arguello, Ethan P. Rosenthal, Abhay N. Pasupathy, and Andrew J. Millis. Experimental Evidence for a Bragg Glass Density Wave Phase in a Transition-Metal Dichalcogenide. *Phys. Rev. Lett.*, 114(2):026802, January 2015. doi: 10.1103/PhysRevLett.114.026802. URL http://link.aps.org/doi/10.1103/PhysRevLett.114.026802.

[237] T. C. Proctor and E. M. Chudnovsky. Effect of a dilute random field on a continuous-symmetry order parameter. *Phys. Rev. B*, 91(14):140201, April 2015. doi: 10.1103/PhysRevB.91.140201. URL http://link.aps.org/doi/10.1103/PhysRevB.91.140201.

[238] T. R. Welberry, M. J. Gutmann, Hyungje Woo, D. J. Goossens, Guangyong Xu, C. Stock, W. Chen, and Z.-G. Ye. Single-crystal neutron diffuse scattering and Monte Carlo study of the relaxor ferroelectric $PbZn_{1/3}Nb_{2/3}O_3$ (PZN). *J. Appl. Crystallogr.*, 38(4):639–647, August 2005. ISSN 0021-8898. doi: 10.1107/S0021889805015918. URL http://scripts.iucr.org/cgi-bin/paper?S0021889805015918.

[239] T. R. Welberry, D. J. Goossens, and M. J. Gutmann. Chemical origin of nanoscale polar domains in $PbZn_{1/3}Nb_{2/3}O_3$. *Phys. Rev. B*, 74(22):224108, December 2006. doi: 10.1103/PhysRevB.74.224108. URL http://link.aps.org/doi/10.1103/PhysRevB.74.224108.

[240] Marek Paściak, Marek Wołcyrz, and Adam Pietraszko. Interpretation of the diffuse scattering in Pb-based relaxor ferroelectrics in terms of three-dimensional nanodomains of the ⟨110⟩-directed relative interdomain atomic shifts. *Phys. Rev. B*, 76(1):014117, July 2007. doi: 10.1103/PhysRevB.76.014117. URL http://link.aps.org/doi/10.1103/PhysRevB.76.014117.

[241] P. Ganesh, E. Cockayne, M. Ahart, R. E. Cohen, B. Burton, Russell J. Hemley, Yang Ren, Wenge Yang, and Z.-G. Ye. Origin of diffuse scattering in relaxor ferroelectrics. *Phys. Rev. B*, 81(14):144102, April 2010. doi: 10.1103/PhysRevB.81.144102. URL http://link.aps.org/doi/10.1103/PhysRevB.81.144102.

[242] R. Burkovsky, S. B. Vakhrushev, S. M. Shapiro, A. Ivanov, K. Hirota, and M. Matsuura. Inelastic and Quasielastic Neutron Scattering in $PbMg_{1/3}Nb_{2/3}O_3$ Above the Burns Temperature. *Ferroelectrics*, 400(1):372–386, September 2010. ISSN 0015-0193. doi: 10.1080/00150193.2010.505858. URL http://dx.doi.org/10.1080/00150193.2010.505858.

[243] A. Bosak, D. Chernyshov, Sergey Vakhrushev, and M. Krisch. Diffuse scattering in relaxor ferroelectrics: true three-dimensional mapping, experimental artefacts and modelling. *Acta Crystallogr. Sect. A*, 68(1):117–123, January 2012. ISSN 0108-7673, 1600-5724. doi: 10.1107/S0108767311040281. URL http://scripts.iucr.org/cgi-bin/paper?S0108767311040281.

[244] Antonio Cervellino, S. N. Gvasaliya, O. Zaharko, B. Roessli, G. M. Rotaru, R. A. Cowley, S. G. Lushnikov, T. A. Shaplygina, and M. T. Fernandez-Diaz. Diffuse scattering from the lead-based relaxor ferroelectric $PbMg_{1/3}Ta_{2/3}O_3$. *J. Appl. Crystallogr.*, 44(3):603–609, May 2011. ISSN 0021-8898. doi: 10.1107/S0021889811012635. URL http://scripts.iucr.org/cgi-bin/quickfind.

[245] Izumi Tomeno, Yoshinobu Ishii, Yorihiko Tsunoda, and Kunihiko Oka. Lattice dynamics of tetragonal $PbTiO_3$. *Phys. Rev. B*, 73(6):064116, February 2006. doi: 10.1103/PhysRevB.73.064116. URL http://link.aps.org/doi/10.1103/PhysRevB.73.064116.

[246] Masatoshi Sato and Yoichi Ando. Topological Superconductors. *arXiv:1608.03395 [cond-mat]*, August 2016. URL http://arxiv.org/abs/1608.03395. arXiv: 1608.03395.

[247] H. Eisaki, N. Kaneko, D. L. Feng, A. Damascelli, P. K. Mang, K. M. Shen, Z.-X. Shen, and M. Greven. Effect of chemical inhomogeneity in bismuth-based copper oxide superconductors. *Phys. Rev. B*, 69(6): 064512, February 2004. doi: 10.1103/PhysRevB.69.064512. URL http://link.aps.org/doi/10.1103/PhysRevB.69.064512.